Generation and control of reactive species in low temperature atmospheric pressure plasma sources

Mr. Seán Kelly

A Dissertation submitted in fulfilment of the
requirements for the award of
Doctor of Philosophy (Ph.D.)

presented to the

School of Physical Science

Faculty of Science and Health

Dublin City University

Supervisor: Prof. Miles M. Turner

August 19, 2014

Declaration

I hereby certify that this material, which I now submit for assessment on the programme of study leading to the award of PhD is entirely my own work, that I have exercised reasonable care to ensure that the work is original, and does not to the best of my knowledge breach any law of copyright, and has not been taken from the work of others save and to the extent that such work has been cited and acknowledged within the text of my work.

Signed .....

Seán Kelly

Student ID: 59119845
Date: August 19, 2014

Contents

Abstract

This work presents results of novel numerical studies investigating the interaction of plasma, gas and heat dynamics for a variety of popular source geometries. Plasma produced chemistry and heat flux reaching a treatment surface is investigated offering fundamental insight into induced plasma effects. Control opportunities for reactive species delivery and heat limitation is investigated in this context.

The mixing of helium and air species in a *corona plasma jet*('plasma needle') is shown to define the shape and composition of the plasma region. Numerical analysis reveals an electro-positive plasma core surrounded by an electro-negative edge reflecting the gas mixture profile. This non-uniform plasma results in non-uniform reactive species production. Circular and annular killing patterns recently found on bacteria treated by the source is shown here to correlate with atomic oxygen distributions at the surface. Interaction of the source with an aqueous surface reveals hydrogen peroxide as the dominant species dissolving at this interface. Atomic oxygen produced by O_2 admixing to helium in a *capacitively coupled jet*('micro-Atmospheric Pressure Plasma Jet') is shown to quickly convert to ozone for increasing device to surface separation. Gas heating is dominated by elastic electron collisions and positive ion heating.

Power modulation of a capacitively coupled jet('micro-Atmospheric Pressure Plasma Jet') is demonstrated as a mechanism for control of reactive species and heat flux delivery to a surface. Power is found to be coupled extensively to the electrons with large initial electron losses leading to weak interference between successive modulation phases. *Frequency variation* in a dielectric barrier discharge plasma source driven in the $\sim$ kHz frequency range is shown here to vary power deposition to the plasma by changing the interval between current pulses. $O_2(a^1\Delta)$ and O_3 production is found to be coupled strongly to the O_2 admixture.

Acknowledgements

I would like to acknowledge my supervisor Prof. Miles Turner who without his guidance, support and collaboration this thesis would not be possible. I want to thank the staff of the National Centre for Plasma Science and Technology and the Physics department at Dublin City University for their support and facilitation of my research which has been invaluable. I would also like to acknowledge my post-graduate piers who provided insight, encouragement and support over the last years. To Stefanie for her patience and support I am very grateful. I would like to thank my parents for their unconditional support throughout my education.

This material is based upon work supported by Science Foundation Ireland under Grant No. 08/SRC/1411. The author wishes to acknowledge the SFI/HEA Irish Centre for High-End Computing (ICHEC) for the provision of computational facilities and support.

Publications & presentations

Publications

- *Generation of reactive species by an atmospheric pressure plasma jet*, Seán Kelly and Miles M. Turner, Plasma Sources Science and Technology, 23, 6, 065013, 2014, http://dx.doi.org/10.1088/0963-0252/23/6/065013
- *Power modulation in an atmospheric pressure plasma jet*, Seán Kelly and Miles M. Turner, Plasma Sources Science and Technology, 23, 6, 065012, 2014, http://dx.doi.org/10.1088/0963-0252/23/6/065012
- *Atomic oxygen patterning from a biomedical needle-plasma source*, Seán Kelly and Miles M. Turner, Journal of Applied Physics, 114, 123301, 2013, http://dx.doi.org/10.1063/1.4821241
- *Simulation benchmarks for low-pressure plasmas: Capactivie discharges*, M. M. Turner, A. Derzsi, Z. Donko, D. Eremin, *S. J. Kelly*, T. Lafleur and T. Mussenbrock, Physics of Plasmas, 20, 013507, 2013, http://dx.doi.org/10.1063/1.4775084

Presentations & conferences

- *Institute of Physics in Ireland (IOPI)*, Rosse Medal poster competition 2014, finalist, 8^{th} March 2014
- *National Centre for Plasma Science and Technology (NCPST)*, postgraduate poster competition, first place, Dublin City University 2013, 17^{th} December 2013
- *British Oxygen Company* Physics poster competition, Dublin City University 2013, second place, 31^{st} May 2013
- 31^{st} International Conference on Phenomena in Ionized Gases (ICPIG) 2013: contributed paper and poster presentation
- *Cost Action MP1101* Topical Workshop: Biomedical applications of Atmospheric Pressure Plasma Technology, Dublin, October 2012
- Bio-Interface Symposium, University College Dublin, October 2012
- *Impedans* Pulsed Plasma Diagnostics workshop, 6-7^{th} September 2012, Dublin: poster presentation

- 39^{th} IEEE International Conference On Plasma Science (ICOPS) 2012: poster presentation & attendance of minicourse on Plasma Medicine and Health Care
- *COMSOL user conference*, Stuttgart 2011: contributed paper and poster presentation
- *Workshop on Radio Frequency Discharges*, National centre for Plasma Science and Technology, Dublin City University, 2011
- 30^{th} International Conference on Phenomena in Ionized Gases (ICPIG) 2011: contributed paper and poster presentation
- *European Summer School*: "Low Temperature Plasma Physics: Basics and Applications", Bad Honnef, Germany, October 2010

List of Figures

List of Tables

Chapter 1

Introduction

1.1 Introduction

Low temperature atmospheric pressure plasmas have generated much research interest due to their reactive properties. Fractional ionisation of a gas (plasma formation) such as helium promotes electron heating without substantially heating the carrier gas. This non-equilibrium characteristic allows generation of a reactive chemistry near room temperature attractive for treatment of heat sensitive materials. Recent research has focused on development of novel medical and biological technologies. Promising applications include the enhancement of wound healing, blood coagulation, disinfection of dental carries and alteration of mammalian cell functions with potential for novel cancer therapies [15, 16, 17, 18, 19, 20, 21]. Decontamination of biologically active surfaces in food processing and hospital environments has demonstrated atmospheric pressure plasmas strong bactericidal characteristics [22]. Established and emerging surface engineering applications of low temperature atmospheric plasmas allow for alteration of the surface properties of polymers [23] and textiles [24] used widely in many industries. Surface engineering of materials such as plastics and textiles with atmospheric plasmas can etch and activate the surface changing properties such as the surface energy [25, 26].

The role of atmospheric gases is central to the efficacy of plasma applications [15, 16, 17, 19, 27]. Many successful sources of current research interest [5] produce dissociated, excited and ionised species of oxygen, nitrogen and water by mixing of these atmospheric gases to a noble carrier gas such as helium. These reactive species often collectively known as *reactive oxygen nitrogen species* (RONS) are present in the reduction-oxidation (redox) biochemistry which plays a central role in many plant and animal cellular functions [27]. Plasma based therapies in biomedicine attempt to manipulate this redox cycle by externally administering RONS to precipitate a desired cellular change. Treatment of living organism brings the requirement of precise dosage which often controls the balance between therapeutic and toxic effects. *Control* of reactive species *generation and delivery* is therefore a key challenge as application of plasmas in medicine emerges [28]. In order to further understanding of RONS interaction with living systems quantita-

tive assessment of their delivery to the treatment surface is necessary. Manipulation of inanimate material surfaces treated by plasma produced RONS similarly depends on the "dosage" received. Reactive oxygen species are critical to increasing surface energy in plasma treated materials such as polypropylene [29] and silicon [30]. In thin film deposition using atmospheric pressure plasma systems reactive oxygen species precipitate cross-linking and oxidation of monomers in formation of nanometre thick polymer coatings [31]. Characterising the chemical influence of plasma treated materials is essential for progress in the understanding of plasma induced surface effects.

This chapter provides an introduction discussing gas breakdown mechanisms and characteristics of the plasma state (section 1.2). Non-equilibrium atmospheric pressure plasma source designs are discussed in section 1.3. The scope of this thesis is given in section 1.4 with an overview of the proceeding chapters.

1.2 Plasma - an introduction

Plasma is the most common state of ordinary matter in the observable universe and is mostly found in stars or in a highly rarefied form in intergalactic space. Naturally occurring terrestrial plasmas include lightning or the spectacular aurora light display caused by the interaction of charged energetic particles from the solar wind in the earth's thermosphere. Plasmas provide a chemically active media which is applied in a wide variety of industries including microelectronic manufacturing [4], lighting [32], plasma display technology [33], surface treatment of materials [34], chemical treatment of gases and liquids [35], nuclear energy research [36] and recently in medicine [20]. The nomenclature "plasma" refers to a collection of charged particles that respond collectively to electromagnetic stimulus. Plasma forms when a significant amount of atoms and molecules are ionised to allow collective conductive behaviour to emerge. The energy required to ionise atoms can come from electrical, thermal or optical sources. The plasmas described in this report are generated via transfer of electrical energy to gases. Externally applied electric fields are used to directly and indirectly heat electrons, ions and neutral charge species in the gaseous state precipitating ionisation, excitation and other chemical reactions. The formation of ions and the availability of unbound charges makes a previously inert gas electromagnetically responsive. This gives plasmas unique characteristics over the gaseous state. Electrons and ions typically present in equal number make up the *plasma density*. The plasma density for the plasmas considered in this report constitutes a small fraction of typically $\ll 0.1\%$ of the background gas.

1.2.1 Gas breakdown

The transformation process of a gas from an insulating to a conducting state is called *gas breakdown*. An illustration of plasma generation with a static or direct current (DC) voltage is shown in figure 1.1 (a) consisting of two parallel metallic plates surrounding a gas. A background density of free electrons in the order of $\sim 10^6$ m^{-3} is present naturally in the ambient environment due to

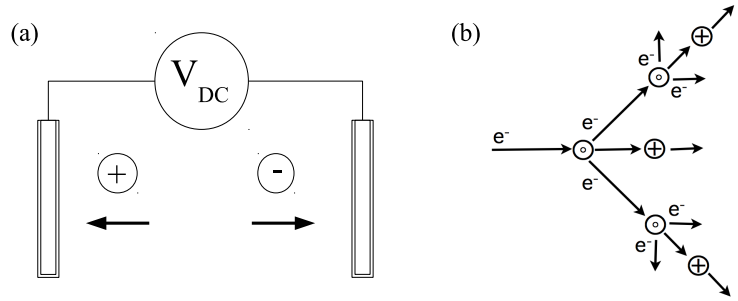

Figure 1.1: (a) Static DC voltage across a gas gap separating two metallic electrodes leading to plasma formation (b) Electron avalanche mechanism

ionisation from background radiation. These background electrons provide a precursor for breakdown. When a particular potential difference is reached free electrons will gain enough thermal energy to significantly ionise the background gas. This voltage threshold know as the breakdown voltage (V_b) is shown as a function of the pressure distance product pd (Paschen curve [2, 37, 38]) in figure 1.2 for various gases.

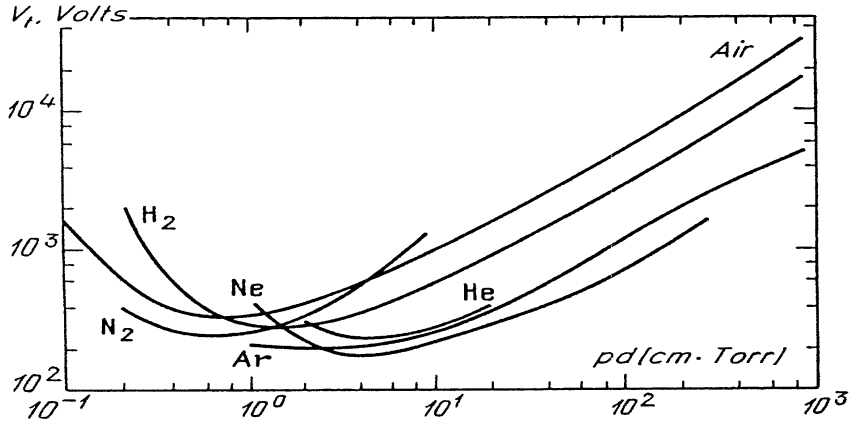

Figure 1.2: Paschen curve: breakdown voltage as a function of pressure and electrode gap distance product (pd) [1]

Gas breakdown occurs from the exponential growth of electrons caused by an avalanche mechanism (see figure 1.5 (b)). The multiplication factor M = $e^{\alpha d}$ [1] describes the intensity of this breakdown where α is the number of ionization events per unit length by electron impact, d is the gap distance between planar electrodes. *Secondary electrons* are produced primarily by ions impacting at the cathode. These secondary electrons can cause further ionisation and electron emission contributing to an exponential growth in electron density. This breakdown process which attributes current growth exclusively to ionization processes is called the *Townsend mechanism* [2].

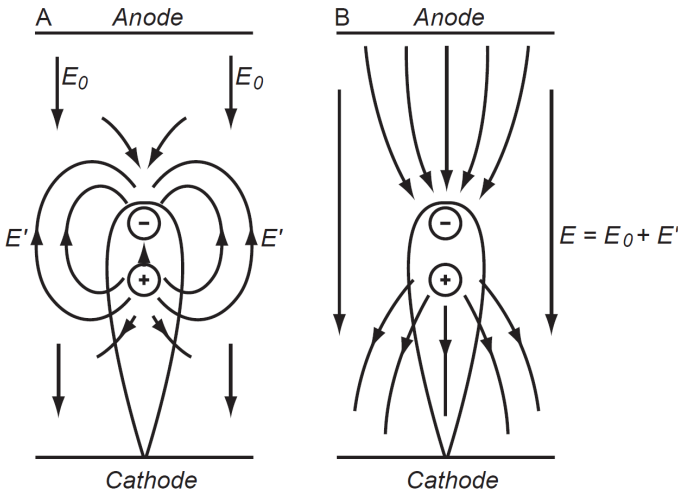

Figure 1.3: Streamer Mechanism [2]: On the left external (E_0) and space charge (E') electric fields are shown separately and on the right the combined external electric fields.

When the external applied voltage is increased significantly beyond the breakdown voltage a streamer driven breakdown occurs. Streamers are thin ionized pathways which form between the electrodes. Transition from an avalanche to a streamer mechanism occurs when the internal electric field of an electron avalanche becomes comparable with the external applied electric field. For multiplication factors M > 10^8 (Meek criterion [1]) localised space charge is formed in the volume between the electrodes initiating streamer development. An initial *primary avalanche* propagates from the cathode as illustrated in figure 1.3. Energetic photons and electrons produced from the primary avalanche induce secondary avalanches near the pathway of the primary avalanche propagating an ionisation front. Electrons due to these secondary avalanches are attracted to the positively charged ionic trail of the primary avalanche. This creates a *quasi-neutral plasma* channel in the primary avalanche pathway. Increased over-voltage leads to intensive streamer development with heat (thermionic) induced electron emission on the electrodes. This results in arcing conditions characterised by high current and gas temperatures.

1.2.2 Plasma collisions

Increased electron thermal energy and charge movement precipitates electron collisions with the background gas producing new species via ionisation and excitation. Collisions are of two main types: *Elastic*: kinetic energy is transferred from electrons to heavy species with the total kinetic energy of collision partners being preserved. *Inelastic*: total kinetic energy of colliding particles is not conserved and collisions result in production of ions and excited species.

The characteristic length between collisions for an electron with a heavy atom or molecule is the *mean free path*. Electron mean free path can be given by $\lambda = 1/(n_g\sigma)$ considering a

simplified model of point mass electrons scattering elastically through a density (n_g) of gas atoms assumed as stationary hard spheres [39, 40]. A cross section (σ) represents an effective surface area of interaction between colliding partners. In this simplified scenario of mono-energetic elastic collisions Argon has a cross section area of 3×10^{-20} m^2 ($\sigma = \pi r^2$) [39]. An atmospheric pressure ideal gas at room temperature has a number density of the order 10^{25} m^{-3}. This gives a mean free path estimation for argon at atmospheric pressure of the order of $\sim \mu m$. The *frequency of electron-neutral collisions* is given here by considering the average electron thermal velocity given by $\hat{v} = 6.7 \times 10^5 \sqrt{T_e}$ [4] where T is the electron temperature in electron volts. The electron-neutral collision frequency can be estimated here by considering the product $\nu_n = \hat{v}/\lambda$. For a typical electron energy of 1 eV ($k_B T(K)$) an electron-neutral collision frequency at atmospheric pressure of 0.67 THz ($\times 10^{12}$ s^{-1}) is estimated.

In reality cross sections for interaction of electrons and atomic species are strongly electron energy dependent. Inelastic collisions such as ionisation or excitation also require the impacting electron to have a threshold energy. Collision cross sections for elastic and inelastic collisions in Helium are shown in figure 1.4. For Helium (figure 1.4) the ionisation threshold value is 24.56 eV and the excitation energy threshold value is 19.8 eV. The *ionisation degree* of a plasma is defined as the ratio of the electron (or ion) number density to the number density of the background gas. It represents the fraction of unbound charge carriers in a plasma active in precipitating and sustaining the reactive chemistry. Non-equilibrium low temperature atmospheric plasmas of interest here typically have an ionisation degree $\ll 0.1\,\%$.

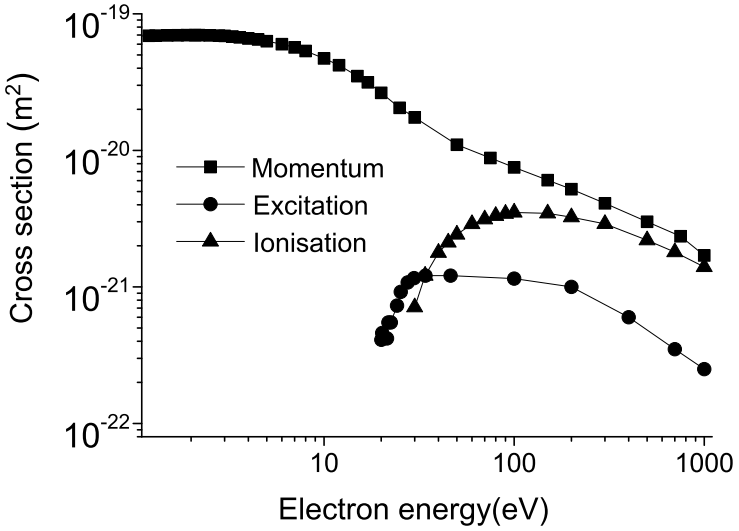

Figure 1.4: Elastic (momentum) and inelastic (ionisation & excitation) electron impact collisions in Helium [3]

1.2.3 Plasma temperature

Heating of charged species by an external electric field in a weakly ionised plasma is dominated by electron heating due to their small mass. Arising from the large mass difference between electrons and the heavy species, the electrons come to thermodynamic equilibrium amongst themselves much faster than they come into equilibrium with the ions or neutrals. If the electrons and heavy species share the same temperature this is known as an *equilibrium* or *thermal plasma*. If the electrons and heavy species are at different temperatures this is known as a *non-equilibrium* or *non-thermal (low temperature)* plasma with the electrons typically having a much higher temperature. This non-equilibrium characteristic allows generation of a reactive chemistry near room temperature attractive for treatment of heat sensitive materials.

Applications of high temperature plasmas include *arc discharges* for melting in welding and for torches in waste treatment and incineration [25]. *Non-thermal discharges* are used in a variety of applications such as semi-conductor manufacturing [4], surface treatment of materials [23] and medicine [15, 41]. Low temperature plasmas can provide a rich chemistry source at or near room temperature due to highly energetic electrons. This characteristic is advantageous for heat sensitive application such as plasma application to skin in medicine or in heat sensitive material surface treatments.

1.2.4 Plasma scale

Electrons and ions in a gas disturbed by an external electric field will oscillate about an equilibrium driven by an electrostatic (Columbic) restoring force. Electrons being far more mobile compared to ions will typically have a much higher frequency response to any electrostatic disturbance with ions approximately stationary on this time scale. The *electron plasma frequency* response therefore dictates a fundamental time scale for the plasma state known as the *plasma period*. This oscillatory response of electrons allows collective conductive properties to emerge while the plasma remains electrically neutral on time-scales above the plasma period. This property is known as *quasi-neutrality*.

The electron plasma frequency also highlights the fundamental spatial scale of plasma behaviour. Consider an electron with thermal motion $\hat{v}$ and oscillation period τ. This fundamental scale is then given by the product $\hat{v}\tau$. This distance is called the *Debye length*. The Debye length is the radius of force influence a charged particle has over its neighbouring charged particles. In this regime the Coulomb electric potential is limited to the distance of the Debye length due to the increased thermal motion of the electrons. The Debye length (λ_D) in a plasma can be calculated using $\lambda_D = 740\sqrt{T_e/n_e}$ [4] where T_e is electron temperature (K) and n_e electron density (m^{-3}). For a range of typical electron density n_e = 10^{15} - 10^{21} m^{-3} and an electron temperature of 1 eV (kT_e) we find Debye lengths in the range of 23.4 μm - 23.4 nm. The corresponding electron plasma frequency is given by $\nu_p = \hat{v}/\lambda_D$ with values in the range of 0.29 - 29 THz ($\times$ 10^{12} s^{-1}). A steady state plasma not in contact with a boundary is electrically neutral at length scales above

the Debye radius and on time scales above the electron plasma period. This sets the temporal and spatial bounds of the plasma state.

In order for the plasma state to exist at least one other charge carrier must be within the Debye sphere of influence so that *collective behaviour* can emerge. Collective plasma behaviour arises from local concentrations of charge confined to a Debye sphere influencing other charges throughout the plasma. A plasma responds collectively to a charge perturbation from an external electric field on length scales larger than a Debye length. The average number of particles in the Debye sphere (*Debye number* N_D) is given by the formula $N_D = (4/3)\pi n_e \lambda_d^3$ [4]. For electron number density typical of the sources in this report in the range of 10^{15} - 10^{21} m^{-3} the Debye number (N_D) ranges from 68 - 0.068.

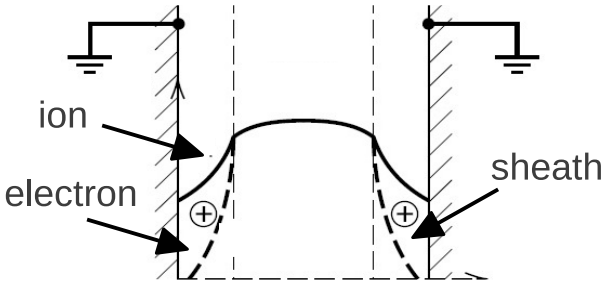

Figure 1.5: Sketch of plasma sheath formed at a solid grounded boundary [4]

1.2.5 Plasma boundary interaction

When a plasma is in contact with a wall or solid boundary unbound charges are lost to the surface and a charged region near the boundary occurs. In the plasma characteristics discussed above we have assumed the plasma is independent of any boundary interaction. The laboratory and industrial plasma's of interest here are however in contact with walls of their containment and treatment surface. The electron thermal velocity is much larger than that of ions due to their difference in mass. This results in a large collisional loss of electrons to the wall and the formation of an area of space charge at the boundary known as a *sheath*. An electric field is formed in which positive potential falls sharply with respect to the bulk which accelerates ions towards the wall and electrons away leading to the formation of a positively charged sheath region. In figure 1.5 (a) we see the formation of sheaths of positive charge when a plasma is in contact with a grounded wall.

1.3 Plasma sources

A range of low temperature (non-equilibrium) plasma sources have recently been developed and investigated for application to heat sensitive materials such as living tissue [5, 42]. In this section various characteristics of low temperature atmospheric pressure plasma source design are discussed. Power (section 1.3.1), electrode design (section 1.3.2), source gas (section 1.3.3) and surface interaction properties (section 1.3.4) are elaborated here.

1.3.1 Power

The frequency of power generation used in application of low temperature atmospheric pressure plasmas ranges from direct current (DC) to alternating current (AC) and includes pulsed voltage supplies across a range of frequencies. AC driven atmospheric pressure plasma applications have been reported in a frequency range from $\sim$ kHz to $\sim$ GHz [5, 42]. Implementation of efficient power supply to plasma devices requires alignment of the impedance of the plasma device with the load requirements of the voltage source. This ensures maximum power transfer between source and load (plasma) by minimising the reflected power. For applications involving AC supplies the typical industry standard generator is designed to deliver power to a load of 50 Ω. *Impedance matching circuits* function to transform the plasma impedance (resistance and reactance) to 50 Ω in this scenario. This is achieved through a circuit design process involving addition of inductive and capacitive elements which alter the load impedance of the plasma device [40].

1.3.2 Electrode design

A planar geometry of parallel metallic electrodes separated by a gas gap represents a *canonical electrode arrangement* (see figure 1.1). When an AC voltage in the radio frequency (RF) frequency range ($\sim$ MHz) is applied this source is known as a *Capacitively Coupled Plasma (CCP)* due to its design resemblance of a capacitive circuit element. The deviation of electrode design from this canonical geometry can be characterised by two main considerations: *current restriction* and *electrode curvature*. This practically manifests in the use of *dielectric barriers* [8, 43, 44] for current limitation and the use of pointed electrodes geometries known as *Corona discharges* [25, 45] over planar geometries. A 2-D sketch of these electrode structures is shown in figure 1.6 (see I and II in figure 1.6). *Dielectric barrier* sources (I in figure 1.6) involve the placement of a material with relatively high dielectric constant such as a ceramic on either or both electrodes in the source. The dielectric barriers limit current by inducing an opposing voltage to that which is applied caused by accumulation of surface charge on dielectric surface. Dielectric barriers are primarily used to limit current at applied voltage frequencies in the kHz range as at higher RF frequencies surface charge has little time to accumulate limiting the effectiveness of the dielectric barrier. Current limitation in this way primarily prevents the onset of arcing conditions often undesirable due to large associated currents and gas temperatures unsuitable for many surface engineering applications. It

can also promote homogeneous plasma formation limiting over-voltage conditions and resultant streamer formation. This homogeneous operation mode often called a *glow or diffuse mode* is desirably in many applications due to its spatial uniformity and reproducibility. *Corona discharges* [25, 45] (II in figure 1.6) are characterised by a highly curved or sharp electrode where large potential gradients and high electric fields result from the applied voltage at the driven electrode. An often luminous glow is localised around the electrode pin where higher plasma densities typically occur. Corona sources for both DC and AC sources have been developed [5] but properties of RF driven devices have gained popularity in many biomedical applications due to their low current and limited gas heating properties. *Surface barrier discharges* (III in figure 1.6) also represent another design which incorporates electrode and dielectric components. The source consists of a single solid piece with an embedded electrode on or inside a dielectric component with resultant plasma formation on the outside surface of the source.

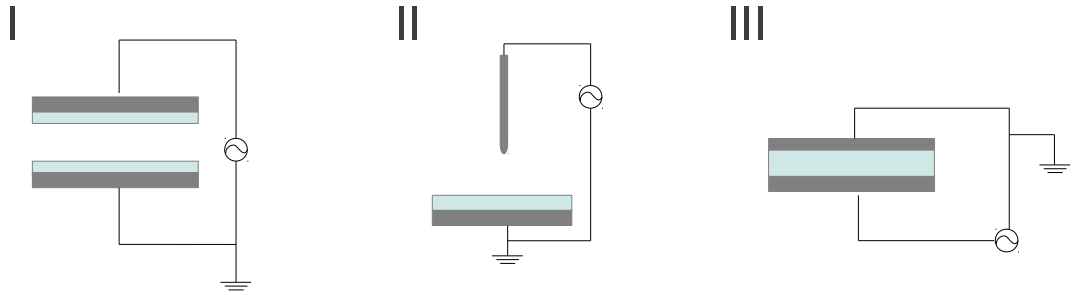

Figure 1.6: Sketch of electrode geometries of low temperature atmospheric kHz/Mhz AC driven plasma sources [5]: I - Dielectric barrier discharge, II - Corona discharge & III - Surface barrier discharge

1.3.3 Carrier gas & jets

The high collision frequency of atmospheric pressure plasmas leads to gap sizes of the order $\sim$ mm being used in application sources [42]. Monatomic gases such as helium and argon are often favoured over molecular gases such as N_2 and O_2 due to their ability to generate low temperature discharges. Noble gases such as helium typically have high ionsiation thresholds (24.8 eV) compared to other gases but are suspectible to ionisation via penning processes involving metastable (19.8eV) interaction with small molecular impurities ($\sim$ ppm) of N_2 and O_2. This dynamic allows gas breakdown at lower energies than with pure mon-atomic gases. The energy threshold for vibrational and rotational excitations in molecular gases is also typically much lower than excitation and ionization reaction thresholds. Vibrational and rotational excitations in molecular gases are therefore a significant sink of electron energy leading to increased gas heating as excited molecular species are quenched by inelastic collisions with the background gas.

Atmospheric plasma jets consist of a carrier gas convecting through a plasma source into the ambient and onto a treatment surface. The carrier gas mixes with atmospheric gases such as N_2,

O_2 and H_2O to generate an abundance of reactive species. Atmospheric gases (N_2, O_2 and H_2O) are also frequently ad-mixed in small percentages to the noble carrier gases to generate reactive species of oxygen, nitrogen and hydrogen. These species are critical to many sources alteration of surfaces and biological systems and an area of extensive research at present [16, 19].

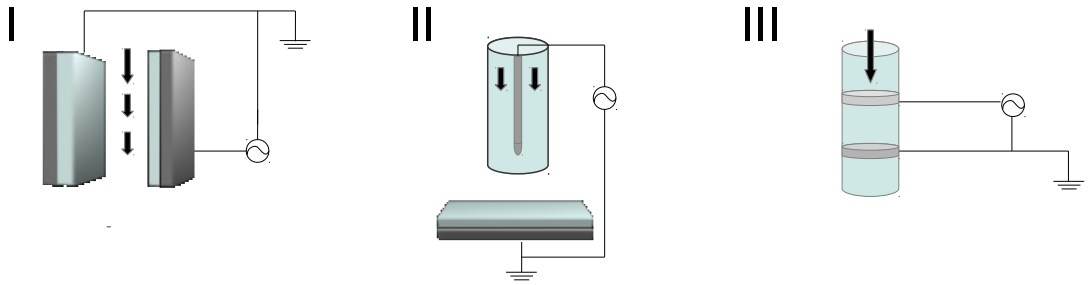

Figure 1.7: Sketch of electrode geometries of low temperature atmospheric kHz/Mhz AC driven plasma jet sources [5]

A sketch of three common electrode structures implemented for containing and convecting a gas flow through a discharge region is shown in figure 1.7. These electrode configuration correspond to the equivalent (non-jet) configurations shown in figure 1.6. Dielectric barrier jets can be constructed with a rectangular (I in figure 1.7) enclosure separated by a dielectric or insulating component to facilitate gas flow. Corona jets typically consist of a container such as a quartz or borosilicate dielectric tube which move gas flows around the pin electrode (II in figure 1.7). A grounded electrode is typically incorporated below the pin on the surface to be treated or as part of the gas tubing [42] for treatment of ungrounded targets. The latter arrangement in which the ground forms part of the gas tubing results in an electric field which forms an electric field across the gas flow (*cross field plasma jet*). Surface barrier jets (III in figure 1.7) in which the driven and grounded electrodes share a common dielectric can be arranged in a linear or cross field arrangement.

1.3.4 Surface interaction

A plasma treated surface is exposed to an abundance of charged and radical species which leads to alteration of surface layer structures via chemical reaction, surface deposition and etching. *Reactive* properties of low temperature atmospheric plasmas include the effects of charged and neutral reactive species, UV radiation (A,B,C bands), electric fields and currents [16, 17, 19, 23, 24, 29, 46]. The design of plasma sources for application can *directly* or *indirectly* treat the target surface inside or outside the electrode gap where the plasma is generated. Indirect sources treat with uncharged properties of neutral (uncharged) reactive species and radiation. Sources which directly treat the target surface will have the additional effects of charged species, electric fields and currents. However, in atmospheric noble gas plasma jets with a sufficiently large over-voltage

propagation of the plasma plume outside the electrode into the surrounding environment can occur. Such plasma plumes were found to be made up of discrete plasma structure called *plasma bullets* [42, 47, 48]. Bullet velocities have been measured with values up to $10^5\ m/s$ [48]. These fast moving plasma structures represent the ionization front of a self-propagating streamer [49]. This continues to be an expanding area of current research [48, 50, 51] with promising applications for delivery of a charged "plasma packet" to remote treatment surfaces.

1.4 Scope of this report

Generation and *control* of reactive species in low temperature atmospheric pressure plasma sources is discussed in this report. Selection and delivery of chemical agents is a key challenge for emerging application of atmospheric plasmas in medicine and surface engineering. Numerical studies of plasma, gas and heat dynamics are undertaken using the geometries found in application sources of current research interest. The *corona*, *capacitively coupled* and *dielectric barrier* plasma devices considered here are shown in figure 1.8. Generation of reactive species by gas mixing with atmospheric gases or via admixture directly to the plasma jet is studied. Models are developed and executed to study plasma sources differentiated by gas dynamics, power characteristics and electrode structure. Electrical behaviour, reactive species generation, gas heating and surface interaction is discussed. Mechanisms for reactive species dosage control and heat limitation to a treatment surface is discovered. Power modulation and frequency variation as potential mechanisms is discussed. Evidence from experimental measurements is corroborated with numerical results in this context.

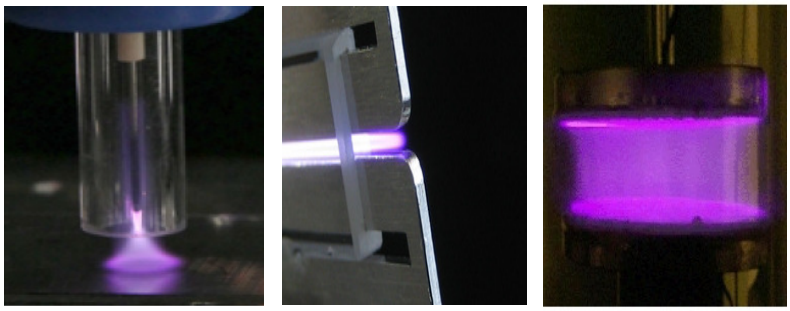

Figure 1.8: Low temperature atmospheric helium plasma sources: plasma needle [6] (left), micro-Atmospheric Pressure Plasma Jet [7] (middle) and dielectric barrier discharge [8, 9]

Chapter 2 describes the equations, formulations and numerical strategies utilised in this work. An overview of common numerical methodologies used in modelling plasma dynamics is initially discussed with further focus given on the fluid approach employed in this work. Details of the gas mixture and heat dynamics models are discussed. An overview of the finite element numerical scheme and the stabilisation methods used are finally presented.

Validation of the plasma model used in this report by comparison with experimental measurement is discussed in *chapter 3*. Comparison of model results with current density measurements is presented for a *dielectric barrier discharge* source (figure 1.8 (right)).

The *plasma needle* [5, 6, 52, 53] is a RF driven ($f = 13.56$ MHz) *corona* plasma device (see figure 1.8 (left)) consisting of a thin tungsten wire driven by a radio frequency voltage surrounded by quartz tubing guiding helium around the wire. A critical factor in its efficacy in treating surfaces such as bacterial samples [12] is attributed to the mixing of the helium carrier gas with air [54]. In *chapter 4* we investigate numerically the role of uncharged *reactive oxygen nitrogen species* (RONS) species produced by the plasma needle device with a focus on the atomic oxygen and ozone patterning at a treated surface. Surface losses are discussed in this context where results of the interaction of plasma produced reactants with reactive solid and liquid interfaces are presented.

Numerical models of reactive species generation in the *capacitively coupled* radio frequency driven *micro-Atmospheric Pressure Plasma Jet* (μAPPJ) [7] is considered in *chapter 5*. The device shown in figure 1.8 (middle) has emerged as a benchmark source for numerical [55, 56, 57, 58, 59, 60, 61] and experimental investigation [60, 62, 63, 64] of capacitively coupled plasma jets for development of applications in biomedicine and heat sensitive surface engineering. The μAPPJ device consists of two parallel steel electrodes surrounded on two sides by transparent quartz allowing optical diagnosis of the plasma core. Small admixtures of atmospheric gases such as O_2 are added to a helium carrier gas to generate bio-active RONS. Production efficiency of reactive species and the subsequent spatial behaviour in the carrier jet before intersecting solid and aqueous surfaces is investigated here. Gas mixing and heating dynamics are also discovered.

Power modulation as a mechanism to control reactive oxygen species generation and heat flux to a treatment surface is discussed in *chapter 6*. Power modulation effects on the capacitively coupled μAPPJ source (chapter 5) are investigated. Gas heating and reactive species generation is investigated for a range of duty cycles at a fixed modulation period of 100 kHz for an electronegative helium oxygen gas mixture.

Frequency variation in a *dielectric barrier discharge* source as a control mechanism for reactive oxygen species generation and heat flux is considered in *chapter 7*. This device shown in figure 1.8 (right) is operated at a lower $\sim$ kHz AC frequency compared with the plasma needle and μAPPJ devices driven $\sim$ Mhz. Charging of the dielectric barriers limits current resulting in pulsed plasma behaviour. The device is operated over larger gap distances ($\sim$ 5 mm) than its RF capacitively coupled counterpart ($\sim$ 1-2 mm). This makes it more suitable for treatment of polymer or textile sheets which can be passed between the electrodes in industrial scale surface engineering applications. Spatial behaviour of reactive species and gas heating is discussed for a large scale device operating in the open air.

Chapter 2

Model description

This chapter describes the equations, formulations and numerical strategies utilised in this work. An introduction to the different modelling approaches typically employed for investigating non-equilibrium low temperature plasmas is initially given in section 2.1. The *fluid model* approach used here is described in more detail in section 2.2. This popular approach allows tractable simulation of plasma species and associated electric fields using macroscopic variables rather than solving for each species velocity and position. Gas dynamics are investigated using the *Navier-Stokes* equations extended to include buoyancy effects with transport of uncharged gas species modelled using a *convection-diffusion* equation (section 2.3). Heat dynamics are studied using a thermal energy formulation coupled to the gas dynamics (section 2.4). The *finite element* numerical technique used in this work is implemented using a commercial partial differential equations (PDE) solver *Comsol Multiphysics*® [65]. Formulation and solution details of the finite element equations is discussed in section 2.5. Issues regarding the stability of equations and artificial stabilisation techniques are considered in section 2.6. Temporal, spatial and novel aspects of the modelling strategy employed is finally discussed in section 2.7.

2.1 Non-equilibrium plasma modelling

Many numerical models of non-equilibrium (non-thermal) plasma sources begin with the *Boltzmann equation*. This formulation describes the evolution of the density of particles in terms of velocity and position over time. Its solution amounts to a fully kinetic solution of a plasmas behaviour over time.

$$\frac{\partial f}{\partial t} + v \cdot \frac{\partial f}{\partial r} + a \cdot \frac{\partial f}{\partial v} = (\frac{\partial f}{\partial t})_c \tag{2.1}$$

f(r,v,t) is a distribution in 6 dimensional phase space *(r,v)* of particle positions and velocities where

$$f(r, v, t)\ \mathrm{d^3r}\ \mathrm{d^3v} = \text{ number of particles inside } \mathrm{d^3r}\ \mathrm{d^3v} \text{ at coordinate (r,v) at time t}$$

By considering particle motion in phase space inside a fixed volume $d^3r\,d^3v$ a continuity relationship for the distribution function emerges. The flux of particles moving through the volume is conserved subject to internal drift $v \cdot \frac{\partial f}{\partial r}$ and external forces $a \cdot \frac{\partial f}{\partial v}$ (acceleration $a = \frac{F}{m}$). Collisions change particle velocities resulting in the appearance and disappearance of particles inside $d^3r\,d^3v$. This is accounted for with the collision operator given as $(\frac{\partial f}{\partial t})_c$ which is evaluated by a spatial integral consisting of the collision partner velocities and their associated distribution functions.

Fluid modelling The fluid approach involves modelling of averaged macroscopic variables such as energy, momentum and density instead of individual particle velocity and positions. The model is derived by taking velocity moments of the Boltzmann equation. This is discussed in more detail in section 2.2. Global models represent a volume averaged (zero dimensional) extension of the fluid approach in which power deposition and species behaviour is assumed to be uniform [4]. This approximation provides a significant reduction in computational requirements but can lead to large inaccuracies in prediction of plasma behaviour.

Kinetic modelling A complete solution of the Boltzmann equations (equation 2.1) represent a fundamental description of plasma behaviour. Solution of the Boltzmann equation is represented by a velocity distribution function which manifests as a solution of a 7 dimensional equation (3 space, 3 velocity and 1 time) for each species. Kinetic descriptions at atmospheric pressure are often intractable due to the high number of collisions requiring some approximation and averaging to reduce the computational overhead.

Monte Carlo methods Another approach to tracking individual particle trajectories is through a combination of Newton's laws and collisional modelling using *Monte-Carlo* methods [66] [67]. This approach does not explicitly follow the trajectory of each particle but uses a smaller set of macro particles to represent their behaviour. Collisions are realised via a weighted probability function using a random number generator. An extension of this idea is found with *Particle in Cell* [66] [67] models which combine the Monte-Carlo technique with a self-consistent treatment of the electric field. Monte Carlo methods provide a more accurate solutions of the plasma dynamics than averaged approaches such as fluid or global models but with an increased computational overhead.

Hybrid approaches Fluid modelling generally requires significantly less computational resources than kinetic models. This allows a larger plasma chemistry in multiple dimensions to be realised with the equivalent kinetic model often too large for efficient implementation on many computational infrastructures. Fluid model inaccuracies are often due to a failure to accurately solve the electron dynamics. This inaccuracy often manifests for higher pressures especially in the sheath regions. A combination of Monte Carlo and fluid models can be used in this instance to improve

accuracy. Electron dynamics are solved using a Monte Carlo approach while a fluid model is used for the heavy species (ions, neutrals) and electric field [68]. This adds some calculation time to a fluid model but usually increases the accuracy of the electron dynamics simulated while not incurring the full cost of a kinetic model.

0 D solutions of Boltzmann equation The *electron energy distribution function* for any fluid model description must be assumed or calculated. If one makes some simplifications about the electron energy relationship to velocity (thermal equilibrium) explicit solutions such as the *Maxwellian* [4] and *Druyvesteynian* [69] electron energy distribution can be found as analytical solutions to the Boltzmann equation for the electron velocity distribution function. This assumption however often fails to capture the physics accurately [70]. Spatially averaged kinetic numerical approaches are frequently used to pre-calculate the *electron collision reaction rates* and *transport coefficients* as a function of the reduced electric field by solving the electron velocity or energy distribution function. Direct methods for solving the Boltzmann equation include expansion methods where a function *f (u)* is used to represent the velocity distribution function as a series of orthogonal basis functions. Assuming spatial uniformity and imposing a uniform electric field approximation on this series allows the electron Boltzmann equation to be reduced to a set of differential equations which can be solved in a steady state manner [71]. Software such as *Bolsig+* [72] are used for solving the *zero dimensional Boltzmann equation* for the electron in non-thermal partially ionised plasmas of focus in this work.

2.2 Fluid model formulation

In this section we discuss aspects of the fluid modelling approach employed in this work to study the plasma dynamics and outline the equations used in this context. We begin by outlining the fluid model formulation for the species density and electron energy continuity equations. A log transformation of the continuity equations is used to increase equation stability here. The electric potential is calculated via the Poisson equation from the spatial distribution of charged species. The electron reaction rates and transport properties are pre-processed into lookup tables using results from a zero dimensional solution of the Boltzmann equation (see above). This solution is used to describe electron impact reactions rates (ionisation, excitation..) and electron transport rates (mobility, diffusivity) as a function of the electron energy. Boundary information and conditions are discussed for Dirichlet and Neumann boundary conditions employed in this work.

2.2.1 Formulation of fluid model equations

The fluid model equations are derived by taking velocity moments of the Boltzmann equation [4]. The n^{th} velocity moment is realised by multiplying the *Boltzmann equation* by a chosen function $g(r, v^n, t)$ and then integrating over velocity space in order to form a conservation equation for

the desired variable. The lowest moment of the Boltzmann equation is attained by multiplication by $g(r, v^{n=0}, t) = v^0 = 1$ and integration over velocity space. This produces the number density conservation equation.

$$\frac{\partial n_i}{\partial t} + \nabla \cdot \Gamma_i = Q_i \tag{2.2}$$

Number density n_i , flux Γ_i , production/absorption term Q_i .

The next velocity moment describes the flux term Γ_i. Letting $g(r, v^n, t) = mv^1$ a continuity equation for momentum conservation is obtained [4, 73, 74]. Inertial, viscous and magnetic effects are typically neglected and further approximations resulting in a flux described by its drift due to the electric field and diffusion due to density gradients only can be made. This results in the so called *drift-diffusion* approximation.

$$\Gamma_i = \mu_i n_i E - D_i \nabla n_i \tag{2.3}$$

where μ_i is the electron mobility coefficient, D_i the diffusion coefficient, E the electric field.

A third velocity moment is considered to derive a continuity equation for energy conservation. Heavy particles (ions and neutrals) can be considered in thermal equilibrium with the background gas and therefore no energy (temperature) balance equation is required to be solved for these species. The electron energy is solved in this formulation by taking $g(r, v^{n=2}, t) = \frac{mv^2}{2}$ to obtain an equation for the electron energy density similar to above (equation 2.3).

$$\frac{\partial n_\epsilon}{\partial t} + \nabla \cdot \Gamma_\epsilon + E \cdot \Gamma_e = Q_\epsilon \tag{2.4}$$

Here $n_\epsilon = n_e \epsilon$ for mean electron energy ϵ. The electron energy flux is expressed as

$$\Gamma_\epsilon = \mu_\epsilon n_\epsilon E - D_\epsilon \nabla n_\epsilon \tag{2.5}$$

2.2.2 Log formulation of fluid equations

Charged species densities can have values often spanning ten orders of magnitude especially in the sheath regions of a plasma. The time and space derivatives in the linear continuity equations can be reformulated using a log formulation. This reformulation increases equation stability by preventing non-zero values [65]. We transform the time and space of the linear continuity equation 2.2, 2.3 in terms of the natural log of the species density $N_i = ln(n_i)$.

$$n_i \frac{\partial N_i}{\partial t} + \nabla . \Gamma_i = Q_i - n_i (u \cdot \nabla) N_i \tag{2.6}$$

$$\Gamma_i = -n_i (\mu_i \cdot E) - n_i (D_i \cdot \nabla N_i) \tag{2.7}$$

Number density n_i , flux Γ_i, production/absorption term Q_i and electron transport properties (μ_e, D_e, μ_ϵ, D_ϵ). The properties of the exponential derivative exploited in 2.6 are shown by the following.

$$\frac{d\,e^Y}{d\,x} = e^Y\,\frac{d\,Y}{dx}$$
$$y = e^Y \text{or } Y = ln\,y \tag{2.8}$$

2.2.3 Electric field

The electric field is calculated using the Poisson equation for potential V. The potential is typically calculated for the plasma region but also for a dielectric region if present on the electrodes. The potential arising from the plasma region is given by the following.

$$-\nabla.\epsilon_0\epsilon_r\nabla V = q(\sum_{k=1}^{N} n_{ion_k} + n_e) \tag{2.9}$$

where ϵ_0 is the permittivity of vacuum, ϵ_r the dielectric constant of the material and q is the charge on the electron or ion (± 1). The potential arising from the spatial distribution of charges couples back to the fluid model above via the drift term in the drift-diffusion flux approximation.

For a dielectric material on an electrode, charge accumulates at the surface of the dielectric and effects the potential applied to the plasma. Accumulation of surface charge σ at the dielectric boundary is accounted by solving an ordinary differential equation of the net current density J on the surface given by the following.

$$\frac{\partial\sigma}{\partial t} = \hat{n}.J_{ion} - \hat{n}.J_e \tag{2.10}$$

The electric field inside the dielectric E_{diel} and just outside E_{gas} is related by Gauss$'$s law.

$$\epsilon_{diel}E_{diel}\cdot\hat{n} - \epsilon_0 E_{gas}\cdot\hat{n} = \sigma \tag{2.11}$$

Equation 2.11 specifies a boundary condition for the potential either side of the dielectric at the gas and material boundaries.

2.2.4 Source and transport coefficients

In the section below we discuss the source coefficient formulation for the species density (electrons, ions, neutrals) and electron energy density equations. This term represents the creation and destruction of species in the plasma. The transport coefficients describe the drift (mobility) and diffusion of plasma species.

Source coefficients The source coefficient Q_i for the electron/ion/neutral plasma particles is given by the following.

$$Q_i = \sum_{i,j} k_{ijk} n_i n_j n_k \tag{2.12}$$

Species density $n_{i,j,k}$ and reaction rate coefficients k_{ijk} for collisions between species i, j and k. For the electrons the reaction rate coefficients k_{ij} are pre-calculated here using collision cross section data [3] with a Boltzmann equation solver [72]. A lookup table is established with the electron impact reaction rate interpolated as a function of the mean electron energy. This formulation is known as the *local mean energy approximation*. The ion and neutral reaction rates are taken from literature as a function of the mean electron energy.

The source coefficients for the electron energy Q_ϵ is given by two terms representing heating by the electric field and energy loss in collisions.

$$Q_\epsilon = -e\Gamma_e \cdot E + \sum_j k_{ej} n_e n_j \Delta\epsilon_j \tag{2.13}$$

Γ_e the electron flux , e magnitude of the charge on electron , E the electric field, the electron energy density n_ϵ, reaction energy loss for electron collisions $\Delta\epsilon_j$.

Transport coefficients The electron transport properties for electron and electron energy mobility μ_e, μ_ϵ are pre-calculated using collision cross section data [3] with a Boltzmann equation solver [72]. A lookup table is established with the electron and electron energy mobilities interpolated as function of the mean electron energy. Einstein's formula is then used to relate mobility and diffusion to temperature.

$$\frac{D_i}{\mu_i} = \frac{k_B T_i}{q_i} \tag{2.14}$$

For the electron energy equation the mean electron energy is related to the temperature by assuming the electron velocity distribution is isotropic giving the relation

$$k_B T_e q_e = \frac{2}{3}\epsilon \tag{2.15}$$

Using equation 2.14 above the electron energy mobility and diffusion coefficients can be written as

$$\mu_\epsilon = \frac{5}{3}\mu_e \tag{2.16}$$

$$D_\epsilon = \frac{5}{3}D_e \tag{2.17}$$

The mobilities of *ionic species* are calculated as a function of the reduced electric field using experimental data from Viehland and Mason [75]. Diffusion coefficient for ionic species are related to mobility values using Einstein′s equation and the gas temperature. Diffusion coefficients for *neutral species* are calculated using Chapman-Ensog theory with Leonard-Jones potentials taken from literature [76].

2.2.5 Boundary conditions

Boundary information is critical to describing the interaction of a plasma when it encounters solid and gaseous boundaries in the domain under investigation. Boundary conditions are required for all variables at all boundaries in the simulation domain. In the following we describe the typical boundary conditions used for the fluid model describing the plasma dynamics.

Three types of boundary conditions are encountered for the plasma species in this report: wall, insulation and constraint boundary conditions. These are typically given by setting a value for the species flux at the boundary. *Wall boundary conditions* involve the interaction of the plasma gas and a solid boundary. Electrons are lost by a net flux to the wall (migrative flux), via thermal motion (thermal flux) close to the wall and also gained by secondary electron emission. The three terms in the following equation for the electron density represent these quantities [77].

$$\Gamma_e.\hat{n} = n_e(\mu_e \cdot E) \cdot \hat{n} + \frac{1}{2}\,\nu_{th,e} n_e - \,(1-a)\sum_i \gamma_i \Gamma_i.\hat{n} \tag{2.18}$$

where γ_i is the secondary electron coefficient for particle i emitting an electron at the boundary and $\nu_{th} = (kT_k/m_k)^{1/2}$ is the thermal velocity. The switching function a accounts for the migrative flux: $a = 1$ when the flux is directed towards the wall and zero otherwise. For the electron energy a similar flux boundary conditions is given by the following.

$$\Gamma_\epsilon.\hat{n} = n_\epsilon(\mu_\epsilon \cdot E) \cdot \hat{n} + \frac{2}{3}\,\nu_{th,e} n_\epsilon - \,(1-a)\sum_i \gamma_i \bar{\epsilon_i} \Gamma_i.\hat{n} \tag{2.19}$$

Here $\bar{\epsilon_i}$ represents the mean initial energy of the electron emitted by incidence of species i. Ions and neutral boundary conditions are given by a similar flux condition. Secondary particle emission is not considered here for the heavy species and migrative flux for the neutral species is absent.

$$\Gamma_i.\hat{n} = \frac{1}{2}\nu_{th,i} - n_i(\mu_i \cdot E) \tag{2.20}$$

An *insulation boundary condition* is used when the plasma region is bounded by a gas and typically represents the edges of the discharge region under study which are not solid. The insulation boundary condition for species density at an open boundary is given by setting the normal compo-

nent of the species flux to zero.

$$\hat{n} \cdot \Gamma_k = 0 \tag{2.21}$$

A *constraint boundary condition* is given by setting the variable of interest to a specific value at the boundary. This is typically done for the electron or electron energy density.

2.3 Mixing gas models

In this section we discuss equations and boundary conditions for the gas dynamics of a buoyant gas such as helium injected into air and couple this to a mass transport model to describe the mixing and reacting of gas species. The couplings between models used is also discussed.

Gas dynamics The *Navier Stokes* equations (compressible flow) [78] are used to model the gas flow.

$$\rho \frac{\partial u}{\partial t} + \rho(u \cdot \nabla)u = \nabla \cdot [-pI + \tau] + F \tag{2.22}$$

$$\tau = \mu(\nabla u + (\nabla u)^T) - \frac{2}{3}\mu(\nabla \cdot u)I \tag{2.23}$$

$$\frac{\partial \rho}{\partial t} + \rho(\nabla \cdot u) = 0 \tag{2.24}$$

where ρ is the density, u the velocity vector, p the pressure, τ the viscous stress tensor and F is the volume force term. Equation of state for p and ρ is given by the ideal gas equation. The volume force is made up of a buoyancy term due to gas mixing.

$$F = g(\rho_{Mixture} - \rho_{Air}) \tag{2.25}$$

At *wall boundaries* which include electrode boundaries and surfaces, a no slip boundary condition is used with fluid velocity $u = 0$. For *gaseous boundaries* such as the surrounding air the viscous stress tensor τ is set to zero ($\hat{n} \cdot \tau = 0$) and the pressure constrained to atmospheric pressure (p = p_{atm}). The *gas inlet boundary condition* is imposed on u by specifying the standard volumetric flow rate. The flow rate (Q_0 m^3/s) at the boundary ($\partial\Omega$) is set with the following constraint.

$$-\int_{\partial\Omega} d_{inlet} \frac{\rho}{\rho_0}(u \cdot \hat{n}) dS = Q_0 \tag{2.26}$$

where d_{inlet} is the boundary thickness (1 mm) and ρ_0 the standard density. Here ρ_0 = M_{mean}/V_0 where M_{mean} is the mean molecular mass of the inlet fluid and V_0 is the standard molar volume. For the case of a helium gas with an O_2 admixture $M_{mean} = (1 - admixture) * M_{He} + admixture$

* M_{O_2} with M_{He} = 0.0040026 kg/mol and M_{O_2} = 0.0319988 kg/mol [79]. The standard molar volume for a gas at 293 K and 1 atmosphere of V_0 = 0.0246172 m^3/mol is used here. To prevent tangential components of velocity at the boundary $n^T \cdot \tau = 0$, $u \times n = 0$ is also imposed [65].

Mass transport The mixing of gases is modelled by solving a continuity equation for mass transport via diffusion and convection [65, 80].

$$\frac{\partial n_i}{\partial t} + \nabla \cdot (-D_i \nabla n_i) + u \cdot \nabla n_i = R_{ijk}$$
$$\Gamma_i = -D_i \nabla n_i + u n_i \tag{2.27}$$

The concentration n_i is solved for each fluid species. The diffusion coefficient is given by D_i and velocity vector by u here. A coupling between velocity field in the Navier Stokes equation (equation 2.22) to the mass transport concentration equation (equation 2.27) via the velocity vector u is used. R_{ijk} for a reacting gas is given by equation 2.12.

The fluid density is computed from the ideal gas law using local pressure and mixture composition (see equation 2.28 below). The dynamic viscosity $\hat{\mu}$ was accounted for using a mixture average formulation.

$$\rho = \frac{p}{T\ R\ \sum_i (\frac{x_i}{M_i})}$$
$$\hat{\mu} = \sum_i \hat{\mu_i} x_i \tag{2.28}$$

where x_i is the mass fraction for species i with molecular weight M_i.

The concentration flux is set to zero $\hat{n} \cdot \Gamma_i = 0$ at *wall boundaries*. For boundaries representing *gaseous boundaries* such as the surrounding air the following boundary condition is implemented.

$$-n \cdot D_i \nabla n_i = 0 \qquad if\ \ \hat{n} \cdot u \geq 0$$
$$n_i = n_{0,j} \qquad if\ \ \hat{n} \cdot u < 0 \tag{2.29}$$

Where $n_{0,j}$ represents the fixed concentration of species i at the gaseous boundary. When the gaseous boundary is air the concentration of each species is taken as a fraction (79% N_2, 20 % O_2, 1% H_2O) of the concentration of an ideal gas at 293 K and 1 atmosphere. At a *gas inlet boundary* a similar concentration constraint is given for inlet gas mixture.

Plasma model gas coupling The velocity field is coupled to the particle density equations (see eqt. 2.2) using a convective flux $u \cdot \nabla n_i$ term to include the effect of gas flow. This gives the

particle density continuity equations as:

$$\frac{\partial n_i}{\partial t} + \nabla . \Gamma_i + u \cdot \nabla n_i = Q_i \tag{2.30}$$

2.4 Heat model

We consider a thermal energy equation for a fluid given by.

$$\rho C_p \frac{\partial T}{\partial t} + \rho C_p (u \cdot \nabla T) = \nabla \cdot (k \nabla T) + Q_p \tag{2.31}$$

Here ρ is the gas density, C_p is the heat capacity at constant pressure, T temperature, k thermal conductivity, u fluid velocity, Q_p is heat from plasma (see below). Heat transfer in a solid domain such as an electrode is given by

$$\rho C_p \frac{\partial T}{\partial t} = \nabla \cdot (k \nabla T) \tag{2.32}$$

The heat generated by the plasma acts as a heat source for the bulk gas. The heat is given by Q_p and its time averaged value Q'_p.

$$Q_p = \left(\sum_i q_i \Gamma_i . E + \sum_j \Delta\epsilon_j R_j + 3 \frac{m_i}{M_g} K_{el} k_b (T_e - T_g) \right) \tag{2.33}$$

$$Q'_p = \frac{1}{\tau_p} \int_0^{\tau_p} \left(\sum_i q_i \Gamma_i . E + \sum_j \Delta\epsilon_j R_j + 3 \frac{m_e}{M_g} K_{el} k_b (T_e - T_g) \right) \mathrm{d}t \tag{2.34}$$

The heat of formation for reaction j is given by $\Delta\epsilon_j$ in equation 2.33 above and the thermodynamic properties for each reaction is calculated from literature [65, 81]. Here k_b represents the Boltzmann constant, R_j the inelastic collision losses and K_{el} the elastic collision losses.

The *insulation boundary condition* -$\hat{n} \cdot (k \nabla T) = 0$ is imposed at external *solid boundaries.* For *gaseous boundaries* the following boundary condition is implemented.

$$\begin{aligned} -\hat{n} \cdot \nabla T &= 0 \qquad && if \;\; \hat{n} \cdot u \geq 0 \\ T &= T_0 && if \;\; \hat{n} \cdot u < 0 \end{aligned} \tag{2.35}$$

Here T_0 is set to represent the temperature of the ambient air. At an *inlet flow boundary* the temperature is fixed.

2.5 Finite element formulation

A commercial partial differential equation (PDE) solver *COMSOL Multiphysics* [65] is used for solution of the finite element discretisation of the partial differential equations solved in this re-

port. An introduction to finite elements is given in section 2.5.1. Formulation of finite element fluid equations is discussed in more detail in section 2.5.2 along with details of solution of these equations (section 2.5.3) in the context of the PDE′s considered here.

2.5.1 Introduction to finite elements

We consider a one dimensional domain discretised for $\Omega = \{x : a \leq x \leq b, a\, b \in \mathbb{Z}\}$ into N-1 sub-domains or elements $\Omega_i = \{x_i : x_{i-1} \leq x \leq x_i\}$. A one dimensional approximation for a variable $u(x,t)$ represented by a linear combination of the product of a piecewise basis function $\phi_i(x)$ and a discrete variable $U_i(t)$ with values defined at each node or mesh point in the domain is given by:

$$u(x,t) = \sum_{i=1}^{N} U_i(t)\phi_i(x) \tag{2.36}$$

Figure 2.1 graphically illustrates this concept ($\phi_i \equiv N_i$). The basis function $\phi_i(x)$ can be described within each element sub-domain by *shape functions*. These shape functions can be characterised by *local or element coordinates*. Element coordinates can be defined generally as a *d-dimensional standard simplex*. A standard simplex is the generalisation of a triangle or tetrahedron to arbitrary dimension (d=1 unit interval, d=2 triangle with 45° angles, d=3 tetrahedron). The simplex obeys the conditions $\xi_i \geq 0$ and $\xi_1 + \cdots + \xi_n \leq 1$. Each finite element Ω_i is parametrised by the local coordinates $\xi_1 \ldots \xi_n$ and mesh elements can be considered as a linear transformation of the standard simplex by letting the global coordinate x_i be a linear function of the local coordinates. In our 1D example, any basis function on any linear mesh element is one of the following so called *shape* functions.

$$\phi = \xi_1,\ \phi = 1 - \xi_1,\ \phi = 0 \tag{2.37}$$

Here the basis function is linear in the mesh interval $\phi_i = 1 - \xi_{d=1}$, equal to the local coordinate ξ_1 on the mesh node and zero outside it. This concept is illustrated in figure 2.2 where ξ_1, ξ_2 parametrize the local coordinate space in element Ω_i.

The finite elements discussed above are known generally as *Lagrange elements*. On each element, u is described by a polynomial of degree k where the local coordinates ξ_d are integer multiples of $\frac{1}{k}$. In our 1D example here we discussed shape function for linear elements corresponding to an element order of $k = 1$. Quadratic elements have order $k = 2$. Increasing element order increases the accuracy of approximation of solution in the element space but comes at the cost of increased computational time.

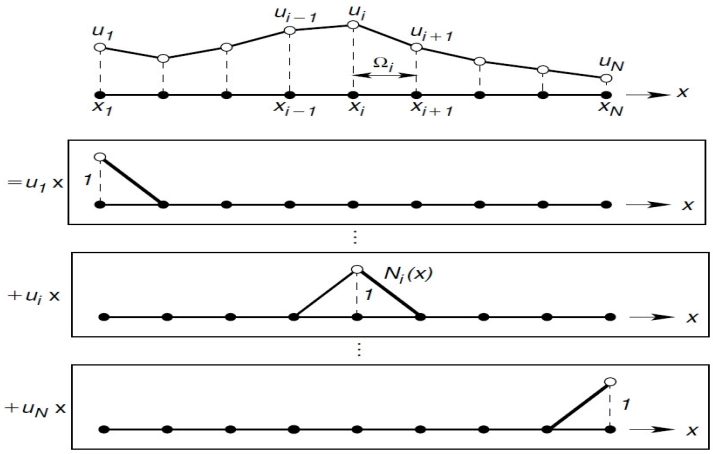

Figure 2.1: One dimensional finite element discretisation [10]

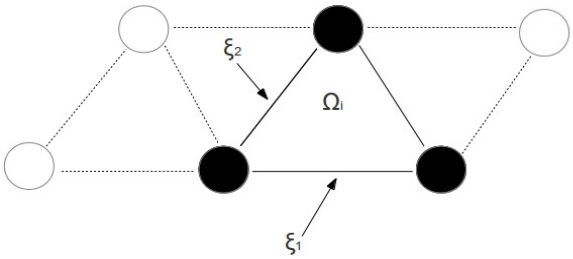

Figure 2.2: Two dimensional simplex

2.5.2 Formulation of finite element equations

The starting point for the discretion of a problem using the finite element numerical method starts with the *weak or integral form* of a *partial differential equation (PDE)*. In this section we discuss the reformulation of our model equations in the weak form and discretion of this form using finite elements. An introduction to finite elements is given in appendix 2.5.1 and more detailed discussions can be found in literature [82]. In this section we outline the transformation of a linear continuity equation from a (strong) differential form to a (weak) integral form and discuss the incorporation of boundary information. Finally discretion and linearisation of this weak form is carried out to formulate our model as a matrix system.

Weak form

We consider the weak formulation of the fluid equations for the linear continuity equation of a particle number density (equation 2.2) as a template for the discretisation of the PDE's used in this

report.

$$\frac{\partial n_i}{\partial t} + \nabla.\Gamma_i = Q_i \tag{2.38}$$

In the weak form a PDE is required only to hold for weak solutions with respect to a test function. We multiply each term by an arbitrary test function v_i and integrate over the domain Ω for each term.

$$\int_\Omega \frac{\partial n_i}{\partial t} v_i \mathrm{d}\Omega + \int_\Omega \nabla.\Gamma_i v_i \mathrm{d}\Omega = \int_\Omega Q_i v_i \mathrm{d}\Omega \tag{2.39}$$

Expanding the second term of 2.39 using integration by parts and the divergence theorem on boundaries $\partial\Omega$.

$$\int_\Omega \nabla.\Gamma_i v_i \mathrm{d}\Omega = \int_{\partial\Omega} \Gamma_i v_i \hat{n}.\mathrm{d}s - \int_\Omega \Gamma_i \nabla.v_i \mathrm{d}\Omega \tag{2.40}$$

Equation 2.40 is now substituted into equation 2.39 giving

$$\int_\Omega \frac{\partial n_i}{\partial t} v_i \mathrm{d}\Omega + \int_{\partial\Omega} \Gamma_i v_i \hat{n}.\mathrm{d}s - \int_\Omega \Gamma_i \nabla.v_i \mathrm{d}\Omega = \int_\Omega Q_i v_i \mathrm{d}\Omega \tag{2.41}$$

This form enables us to specify a *Neumann boundary* condition by direct substitution of the boundary term. To enforce a *Dirichlet boundary condition* we would have to solve an additional problem of the form of equation 2.42 on the boundary $\partial\Omega$ given by:

$$\int_{\partial\Omega} R(n_i, t) v_i \hat{n}.\mathrm{d}s = 0 \tag{2.42}$$

Alternatively we can include a Dirichlet boundary condition as a constraint by using a *Lagrange multiplier* formulation. We consider a general formulation which includes a Lagrange variable μ to facilitate the inclusion of dependent Dirichlet boundary conditions for the input coefficients $R(n_i, t)$ and $G(n_i, t)$ representing the Dirichlet boundary constraint and the Neumann flux value at the boundary.

$$\begin{aligned} 0 &= R(n_i, t) \quad on \quad \partial\Omega \\ n \cdot \Gamma &= G(n_i, t) - \frac{\partial R}{\partial n_i}\mu \end{aligned} \tag{2.43}$$

We now substitute our boundary terms (equation 2.43) into equation 2.40 above.

$$\int_\Omega \frac{\partial n_i}{\partial t} v_i \mathrm{d}\Omega + \int_{\partial\Omega} (G - \frac{\partial R}{\partial n_i}\mu) v_i \hat{n} \cdot \mathrm{d}s - \int_\Omega \Gamma_i \nabla . v_i \mathrm{d}\Omega = \int_\Omega Q_i v_i \mathrm{d}\Omega$$
$$0 = R \text{ on } \partial\Omega \tag{2.44}$$

Equation 2.44 above is known as the *weak formulation* of the PDE 2.5.2. Weak form formulations for the log continuity equations (see section 2.2.2), electric field (see section 2.2.3), Navier stokes and mixing gas model (section 2.3) can be derived in a similar way.

Discretisation of weak form

Discretisation of the weak form equations using finite elements (see appendix 2.5.1) approximates the dependent variables as a combination of the product of a piecewise basis function and values defined on each element in the domain. We consider the particle number density and its approximation:

$$\frac{\partial n_i}{\partial t} + \nabla \, . \, \Gamma_i = Q_i \tag{2.45}$$

$$n_l = \sum_{i=1} n_j(t) \phi_j^{(l)} \tag{2.46}$$

Where ϕ_j^l are the basis functions for l variables n_l with solution vector n_j containing the degrees of freedom. The *Galerkin method* is commonly used for solution with finite elements. The Galerkin method selects the test functions from the basis functions $v_l = \phi_j^{(l)}$. Substituting into the weak form of the PDE this gives a set of differential algebraic equations (DAE).

Discretisation of continuity equation The weak expression for the continuity equation 2.41 now becomes (dropping the summation i on n):

$$\sum_{j=1} \int_\Omega \frac{\partial}{\partial t} n_j \phi_j^{(l)} \mathrm{d}\Omega + \sum_{j=1} \int_{\partial\Omega} (G - \frac{\partial R}{\partial n_j}\mu) \phi_j^{(l)} \hat{n} . \mathrm{d}s - \sum_{j=1} \int_\Omega \Gamma_j \nabla . \phi_j^{(l)} \mathrm{d}\Omega$$
$$- \sum_{j=1} \int_\Omega Q_j \phi_j^{(l)} \mathrm{d}\Omega = 0$$
$$0 = R \text{ on } \partial\Omega \tag{2.47}$$

For l variables across our domain discretised by $j = 1, \ldots, M$ finite elements.

We now rewrite the above in matrix form.

$$L(n,\dot{n},t) = \sum_{j=1}\int_\Omega \frac{\partial}{\partial t} n_j \phi_j^{(l)} \mathrm{d}\Omega + \sum_{j=1}\int_{\partial\Omega} G\phi_j^{(l)}\hat{n}.\mathrm{d}s - \sum_{j=1}\int_\Omega \Gamma_j \nabla.\phi_j^{(l)}\mathrm{d}\Omega$$
$$- \sum_{j=1}\int_\Omega Q_j\phi_j^{(l)}\mathrm{d}\Omega = 0$$
$$N_F\Lambda = -\int_{\partial\Omega}(\frac{\partial R}{\partial n_j}\mu_j)\phi_j\ \hat{n}.\ \mathrm{d}s$$
$$M(n,t) = 0 \tag{2.48}$$

Where N_F is given by $\phi_j \frac{\partial R}{\partial n_j}$, Λ contains the Lagrange variables μ_j and $M(n,t) \equiv R$ contains the constraints. Our time dependent PDE can now be written in matrix form as:

$$0 = L(n(t),\dot{n}(t)) - N_F(n(t))\ \Lambda(t)$$
$$0 = M(n(t)) \tag{2.49}$$

L is called the *residual matrix*, M the *constraint residual matrix*, Λ the *Lagrange multiplier matrix* and N_F the constraint force *Jacobian matrix* $\frac{\partial M}{\partial n}$.

Linearisation Many of the terms in the continuity expression for particle density discussed above are dependent on other variables (n_i) for evaluation. In order to solve the continuity equation implicitly at each time step we must linearise our PDE. We consider an initial guess value at point ($n = n_0\ \ , \frac{dn_0}{dt} = \dot{n}_0$) as a linearisation point and take a Taylor expansion. Equation 2.49 now becomes.

$$L(n_0,\dot{n}_0) = K(n_0)(n-n_0) + D(\dot{n}_0)(\dot{n}-\dot{n}_0) + N_F(n_0)\ \Lambda$$
$$M(n_0) = N(n_0)(n-n_0) \tag{2.50}$$

Here L is called the *load vector*, its Jacobian $K = \frac{\partial L}{\partial n}$ is called the *stiffness matrix* and $D = \frac{\partial L}{\partial \dot{n}}$ is known as the *mass matrix*.

2.5.3 Solutions of finite element formulation

The commercial PDE solver *COMSOL multi-physics* [65] is used for numerical simulations in this report. In this section we outline the solution methods and strategies employed here.

Time dependent solutions The Lagrange multipliers can be eliminated by selecting an appropriate test function boundary condition. We introduce the following boundary conditions on the test function.

$$0 = \frac{\partial R}{\partial n_l} v_l \text{ on } \partial\Omega \tag{2.51}$$

This ensures that the weak formulation (equation 2.44) is solved only for n_l such that the solution holds for all test functions v_l that satisfy the above boundary conditions. The weak formulation given in equation 2.44 above can now be reformulated as:

$$\int_\Omega \frac{\partial n_l}{\partial t} v_l \mathrm{d}\Omega + \int_{\partial\Omega} G v_l \hat{n} \cdot \mathrm{d}s - \int_\Omega \Gamma_i \nabla . v_l \mathrm{d}\Omega = \int_\Omega Q_l v_l \mathrm{d}\Omega$$
$$0 = \frac{\partial R}{\partial n_l} v_l \text{ on } \partial\Omega \tag{2.52}$$

Equation 2.50 can now be rewritten as

$$L(n_0, \dot{n}_0) = K(n_0)(n - n_0) + D(\dot{n}_0)(\dot{n} - \dot{n}_0)$$
$$M(n_0) = N(n_0)(n - n_0) \tag{2.53}$$

The standard Galerkin method consists of finding n such that the above equation is satisfied. Our time dependent differential algebraic system (DAE) is implemented and solved using the commercial PDE solver *Comsol multi-physics* [65]. A *backward differentiation formulation (BDF)* is used for time stepping and a *Newton method* is used to solve the linearised system of equations at each time step. The space dependent integrals occurring in the components of matrices in equation 2.50 are calculated using a *numerical quadrature* method. This computes the integral over a mesh element by taking a weighted sum of the integrand evaluated at the nodes across the mesh element [65].

Comsol implements a time-dependent solver algorithm called *IDA* (Implicit Differential Algebraic) [83] which uses a variable order variable step-size *backward differentiation formula (BDF)* method for integration of the time integral. BDF is a linear multi-step method that approximates the derivative of the function using information from previous time steps. The BDF method is a fully implicit method and requires the solution of a set of non-linear equations at each time step.

At each time step a linearised system of differential equations (equation 2.53) must be solved. This is carried out using a *Newton solver* [84]. The linearisation of a discrete equation in general form $f(U) = 0$ about a point U_0 is given by $f'(U_0)\delta U = -f(U_0)$ where $\delta U = U - U_0$ (see equation 2.53 above). Initially the Newton solver finds the solution of a linear system. This is carried out using the *PARDISO* linear solver algorithm [85, 86]. The new iteration is computed using $U_1 = U_0 + \lambda \delta U$ where λ $(0 \leq \lambda \leq 1)$ is the *damping factor*. Next the error E is calculated by solving $f'(U_0)E = -f(U_1)$. The Newton iteration continues by reducing the damping factor

λ until an error E reaches a specified tolerance or a minimum damping factor is exceeded.

2.6 Stability and stabilisation

In this section we discuss the stability of transport equations used in this work. In section 2.6.1 dimensionless numbers commonly employed to analyse transport equation stability are discussed. In section 2.6.2 artificial diffusion and source terms employed are discussed.

2.6.1 Dimensionless numbers

Numerical schemes find difficulties in areas of high gradients of the physical quantities under study such as at a boundary. In this section we discuss some dimensionless numbers derived from a generic transport equation which allows us to study the stability of equations of this type (see equations 2.22,2.30). These numbers [82] study the ratio of advective forces due to bulk motion of the fluid against diffusive forces and/or production/absorption effects of the physical quantity of interest. We consider a generic *advection-diffusion-reaction* transport equation for discussion here.

$$\frac{\partial u}{\partial t} + \beta\nabla \cdot u + \nabla \cdot (-c\nabla u) + su = 0 \tag{2.54}$$

The *Péclet number (Pe)* [82] is defined as the ratio of the rate of advection of a variable (bulk motion) to the rate of diffusion of the same variable. In equation 2.54 this measures the ratio of convective force β to diffusive forces affecting variable u. We define the element Péclet number for element mesh size h as follows:

$$Pe = \frac{\|\beta\|h}{2c} \tag{2.55}$$

The *Dämkohler number (Da)* [82] measures the magnitude of the production/adsorption effects s against the convective forces β.

$$Da = \frac{|s|h}{\|\beta\|} \tag{2.56}$$

If the production/absorption term in equation 2.54 is zero then Galerkin discretisation (see section 2.5.2) becomes unstable when the Péclet number is $Pe > 1$. If the production/absorption term is non-zero the Galerkin discretisation becomes unstable when production/absorption effects dominate over the viscous effects. The Dämkohler Péclet product can be used to describe this combined effect with instabilities arising when $2DaPe = \frac{|s|h^2}{c}$ is $>\ 1$ [82]. Increasing the mesh resolution

can reduce Pe and $2PeDa$ to prevent oscillations. In practise this is often not possible due to the large mesh requirements. For this reason *artificial diffusion and source* terms are often added to stabilise transport equations.

2.6.2 Stabilisation techniques

In executing the models used in this report we employed various stabilistaion techniques to enhance equation stability for solutions over computationally tractable mesh sizes. Stabilistaion techniques included the use of artificial diffusion terms for high Péclet or Dämkohler number flows and artificial source terms in the plasma model solutions to prevent singularities in the log formulation of the continuity equations.

Artificial diffusion terms include both consistent and inconsistent techniques. *Consistent stabilisation* adds numerical diffusion to the equation being solved in a way which results in a solution being the same as that without numerical diffusion while *inconsistent stabilisation* adds numerical diffusion which may result in a solution being different from the solution without the addition of numerical diffusion. *Streamline diffusion* is a consistent stabilisation method that introduces artificial diffusion in the streamline direction. Extended Galerkin methods which use streamline diffusion are the *Streamline Upwind Petrov Galerkin (SUPG)* method [82, 87] and the *Galerkin Least Square (GLS)* method [88]. GLS is the streamline diffusion available within the Comsol multi-physics [65] software which is stable for $2PeDa > 1$ [65, 88]. An isotropic diffusion term $c_{iso} = \eta\|\beta\|h$, where the term η is a tuning parameter, can also be added to the diffusion term in equation 2.54 in an inconsistent manner.

$$\frac{\partial u}{\partial t} + \beta \cdot \nabla\ u - \nabla \cdot ((c + c_{iso})\nabla u) + su = 0 \tag{2.57}$$

The Péclet number is now:

$$Pe = \frac{\|\beta\|h}{2(c + c_{iso})} = \frac{\|\beta\|h}{2c + \eta\ \|\beta\|h} \tag{2.58}$$

We see here that for $\eta = 0.5$ the Péclet number is always less than 1 ($Pe < 1$). The Dämkohler number in this case is unaffected so instabilities arising from production/absorption forces dominating convective forces can still cause oscillations.

An *artificial source term* Q_{stab} is added to existing source terms in the log continuity equation (see equations 2.6) for the plasma model formulation considered in this work. This prevents numerical singularities arising when species density reach zero.

$$Q_{stab} = \phi.(exp(-\zeta ln(n_i)) \tag{2.59}$$

The tuning parameters ϕ and ζ ($\zeta, \phi > 0$) must be chosen carefully for this inconsistent artificial

stabilisation term as to not perturb the calculations significantly. By default here $\phi = N_A$ is used where N_A is Avogadros number [65]. The ratio of this stabilisation term over the original source term $\frac{Q_{stab}}{Q_i}$ is used to measure and minimise the perturbing impact of this term on the equations being solved for a given mesh.

2.7 Modelling strategy

The modelling strategy employed in this work attempts to reduce the computational overhead while maintaining an accurate description of the underlying physics of interest. Balancing these needs manifests in both temporal and spatial strategies for model design. In the following we discuss these aspects in the context of the models developed in this report. We also discuss how the model strategies employed in this report advance on previous modelling efforts for the plasma sources of interest.

Spatial

The three plasma sources studied in this report (see section 1.4) represent two distinct geometries for plasma generation. The corona plasma jet (chapter 4) consists of a pin electrode encased in a quartz tube to contain and convect gas flows. The simulation domain is reduced here by considering the devices cylindrical symmetry. A two dimensional axi-symmetric domain provides an accurate account of the plasma and gas dynamics for this source. The capacitively coupled (chapter 5) and dielectric barrier sources (chapter 7) represent a planar geometry. Assuming uniformity in the plasma behaviour reduction of the simulation domain to one dimension in these sources is used. Plasma produced species and heating terms are extrapolated to higher dimensions (2-D, 3-D) for both geometries here for use as source terms in higher order models of the uncharged reacting, mixing and heated jet (see below).

Charged species in the plasma are typically contained within the electrode region by the electric field. The gaseous and plasma domain simulated will overlap to a various degree depending on the electrode design. If the target surface doubles as the ground (chapter 4) then a larger section of the gaseous domain will overlap with the plasma domain compared to a remote treatment surface (chapter 5). The solution domain for the plasma dynamics is however typically a subset of the larger domain required for investigation of the uncharged phenomena of gas and heat dynamics.

Temporal

The physics of atmospheric plasma jets involves a large range of time-scales. The plasma produces an abundance of both charged and uncharged species. Charged species (e, O_2^+, O^-, He_2^+...) respond to changes in the externally applied electric field which can be of the order of $\sim$ ns. Uncharged species consist of both long and short lived species which change on time-scales from the plasma dynamics up to the gas residence time ($\sim$ s). Long lived species consist of plasma

produced (O, N,..) and background species (He, N_2, O_2...). Short lived species are produced by excitation reactions in the plasma (O (^1D), (N (^{2}D), He*...) and react quickly within the discharge region. Gas heating is induced by the plasma dynamics ($\sim \mu s$) and plasma produced uncharged species ($\sim s$) but changes on time-scales above the order of the gas residence time ($\geq$ 1 s). These disparate time-scales are coupled by various averaging and sequential couplings discussed below.

In *chapter 4* a 2-D model of gas dynamics in a corona plasma jet ('plasma needle') is solved initially for a steady state helium air mixture profile. The plasma dynamics are then solved using this constant mixture profile. Once steady state power conditions ($\sim$ 10 μs) are reached in the plasma averaged production rates are extrapolated as source terms for a 2-D model of uncharged species reacting and convecting to the treatment surface below the device. This decoupling allows tractable solutions of the neutral (uncharged) plasma produced species behaviour on the time scale of the gas flow ($\sim$ 1 s) which is much larger than the time scale of the plasma dynamics ($\sim$ 1 ns). Such a decoupling relies on the assumption that the charged and neutral species produced by the plasma are weakly interacting. The bulk plasma density ($\sim 10^{17}$ m^{-3}) is typically several orders of magnitude lower than the steady state densities of reactive species (O, O_2 ($a^1\Delta$), O_3, N, N_xO_x, HNO_x ...) produced ($\sim 10^{21}$ m^{-3}) in this type of discharge [56, 59, 89, 90]. Uncharged plasma produced species density are therefore not significantly effected by losses due to interaction with charged species. Charged and excited species densities in the plasma may however be changed remarkably by the influence of plasma produced reactive species. Earlier reports [13, 60] show that the the primary ionisation mechanism is via helium meta-stable penning ionisation with N_2 and O_2 over plasma produced species (O, O_2 ($a^1\Delta$), O_3, N, N_2 ($A^3\Sigma$)..). Charge transfer effects due to O_2 ($a^1\Delta$), O_3 and O interaction can however change the composition of negative charge carriers depending on the O_2 density in the discharge region [90]. Analysis of larger reaction sets from literature [90, 91] reveals similar reaction pathways and transport properties for both these negative charge carriers [90, 91]. The continuously powered radio frequency plasma considered here neglects these charge transfer interactions as they are not likely to lead to large inaccuracies in the *overall electrical behaviour* of the plasma. Production trends for uncharged reactive species which is of focus in this report are preserved in this context.

Operational conditions considered for the capacitively coupled (μAPPJ) source in *chapter 5* result in a homogeneous helium-oxygen mixture in the discharge domain. The plasma dynamics are reduced to a one-dimensional model [55, 56, 57, 58, 59, 60]. Phase averaged reactive neutral (uncharged) species production rates are extrapolated from the 1-D plasma model solutions and coupled to a 2-D model of the reacting and mixing helium carrier jet in the ambient in a similar way to the corona jet discussed above. A gas heating source term is also extrapolated from 1-D solutions of the plasma dynamics for use in a 2-D model of the gas flow and heating.

The capacitively coupled (μAPPJ) source is studied again in *chapter 6* but this time with a pulsed power source. Electron detachment reactions may influence the plasma dynamics during the power-off phase when the plasma density drops significantly (see chapter 3). Analysis of

Helium-oxygen reactions revealed an electron detachment reaction involving atomic oxygen of possible importance during the plasma decay. In order to study the influence of this reaction a fixed value for the O density based on an O_2 to O conversion rate of 0.3 % is used [91, 92]. The same approach and chemistry is used in *chapter 7* where the plasma behaviour is also pulsed due to the lower frequency ($\sim$ kHz) of the externally applied electric field.

Advancements

The numerical study of a corona plasma jet ('plasma needle') considered in *chapter 4* advances previous numerical investigations of Sakiyama et al. [13]. This work approximated the air in the gas mixture as consisting of N_2. The chemistry considered in this report extends on this study by incorporation of an air chemistry consisting of N_2, O_2 and H_2O. Inclusion of molecular O_2 species provides significant insight into the role of negative ions which are critical to the spatial behaviour of the plasma. The construction of an additional model of a reacting gas consisting of uncharged plasma produced species provides information of the steady state density of reactive oxygen and nitrogen species reaching a treatment surface for the first time. These results provide numerical evidence for previous experimental reports of Goree et al. [12, 53] and Sakiyama et al. [54] for the anti-bacterial role of atomic oxygen in S. Mutans bacteria samples treated by the plasma needle. Surface interaction of plasma produced reactive species is also investigated here. This novel analysis is conducted for both a reactive solid and liquid interface.

Numerical investigation of a capacitively coupled ('μAPPJ') source is considered in *chapter 5*. Previous numerical investigations of the plasma dynamics for helium-oxygen mixtures in this source [56, 58, 59, 60, 61, 63, 90] reveal the crucial role of helium metastable in penning ionisation processes [56, 60, 63], the effect of gap size on plasma formation [58, 63] and production mechanisms for atomic oxygen [59, 61]. Global models [90, 91] have revealed the dominant charged and uncharged species in the plasma region allowing subset chemistries for spatially resolved fluid models to be constructed. Yang et al. [59] discussed the behaviour of plasma produced species in the jet effluent in a helium-oxygen atmosphere and its interaction with a reactive surface using a 1-D model and approximations of the gas flow. Hemke et al. [61] used 2-D models of the capacitively coupled jet convecting in a helium-oxygen atmosphere providing further insight into the composition of the jet effluent. Our work extends on these efforts by incorporating interaction of the jet effluent with ambient air. The efficiency of reactive oxygen species *generation* by admixture of O_2 (section 5.3.1), the subsequent spatial profiles of reactive species produced at various distances below the device both with and without a target surface (section 5.3.3) and the interaction of plasma produced reactive species with treatment surfaces (section 5.3.5) provides novel insight into the operation of this device. The modelling strategy employed in this work allows efficient solution for two dimensional dynamics of reactive oxygen species, gas mixing and heating behaviour solving to steady state for disparate time-scales ranging from ns to $\sim$ 1000 s.

Pulse modulation of the capacitively coupled 'μAPPJ' source considered in *chapter 6* presents

a novel investigation of this potential control mechanism for heat limitation and delivery of reactive oxygen species to treatment surfaces. The study of the continuously powered source in chapter 5 reveals a complex and limited operational range for variation in reactive species production and heat flux. This behaviour due to the electro-negative character of the discharge leads to a non-linear power behaviour with voltage variation. Modulation of the applied power offers a possible alternative mechanism for control of reactive species and heat flux to treatment surfaces which warrants further investigation. Previous reports [93, 94] for ∼Mhz driven capacitively coupled devices has discussed the plasma dynamics for electro-positive helium gas mixtures. This chapter presents fundamental and novel insight into the plasma growth and decay behaviour in electronegative helium-oxygen mixtures coupled with an investigation of the plasma produced reactive species, heating and gas dynamics. The demonstration of control of reactive species and heat flux delivery to treatment surfaces in this context provides a significant advance in current understanding.

The plasma dynamics of the diffuse glow mode of the dielectric barrier discharge is discussed in *chapter 7*. The critical role of small amounts of N_2 impurity in plasma formation for helium discharges via penning ionisation has been studied numerically in several previous reports [44, 95, 96]. Numerical investigations for helium-O_2 mixtures [97, 98, 99] for the source have considered the 'quenching' effects of small oxygen admixtures ($\sim$ 10 ppm) on plasma dynamics and the ability of frequency variation to recover the glow mode of operation. Frequency variation is investigated here as a mechanism for varying the power deposition to the plasma allowing control of reactive species production and heat flux. The pulsed nature of this ∼kHz driven discharge (see chapter 3) allows frequency variation to vary power deposition significantly by interrupting the period between plasma growth and decay. This chapter focuses on the potential to control the reactive oxygen species production and gas heating by varying the frequency. Similar to earlier studies of the plasma needle and μAPPJ investigation of the plasma produced reactive species, heating and gas dynamics provides a novel insight into the reactive species and heat flux produced by an industrial scale implementation of this source.

Chapter 3

Model validation

In this chapter we discuss validation activities for the numerical models described in chapter 2. *Validation* in this context refers to a process of establishing whether the numerical model provides an accurate representation of physical reality. A one dimensional model for an atmospheric dielectric barrier discharge plasma source operating with helium is considered here for experimental comparison (section 3.1). This discharge has been the case of previous computational benchmarking [44, 95, 96]. We extend on these efforts here accounting for air impurities in the discharge.

3.1 Dielectric barrier discharge benchmark

Comparison of a one dimensional plasma model (see chapter 2) with experimental measurements [11] for a *dielectric barrier discharge* (DBD) plasma source operating in atmospheric pressure helium is discussed. Conditions for a diffuse mode of plasma operation with a helium carrier gas known as a *glow discharge* [8, 9] is considered. This homogeneous discharge behaves uniformly in space allowing much of the physics to be investigated using a one dimensional model. Results of charged species behaviour is compared with experimental measurements of Mangolini et al [11] for discharge current behaviour. The emergence of asymmetric behaviour in the current profile is discussed in this context.

3.1.1 Model description

The *dielectric barrier discharge* (DBD) consists of two dielectric layers of thickness 1 mm with separation between the dielectric layers of 5 mm. One electrode is driven with a sinusoidal applied voltage with a 10 kHz frequency and a voltage amplitude of V_a = 1.85 kV while the other electrode is grounded. A self consistent fluid model with Poissoin's equation for the electric field is solved for the electron, electron energy and heavy species densities. The model was implemented using a *finite element scheme* with the commercial partial differential solver *Comsol Multiphysics* [65]. A log formulation of the electron and heavy species density continuity equation is used along with

source stabilisation (see section 2.6). The electron transport and reaction rates are preprocessed by solving the zero dimensional Boltzmann equation using the *Bolsig+ solver* software [72] and with collision cross section data from the University of Toulouse *Lxcat* database [3]. The ion transport values are taken from literature [75] (see section 2.2.4 for more details).

The helium-air chemistry used here is shown in table 3.1. The species considered include the electron e, seven ionic species (He^+, He_2^+, N_2^+, O_2^+, O^-, O_2^- and H_2O^+) with fifteen neutral species (He, He^*, He_2^*, O_2, O_2 ($a^1\Delta$), O, O (^1D), N_2, N_2 ($A^3\Sigma$), N_2 ($B^3\Pi$), N, N (^{2}D), H_2O, OH, and H). Reactions R_{1-14} in table 3.1 follow the He-N_2 reaction scheme of Golubovski et al [44]. The oxygen reaction scheme is given by reactions R_{15-22}, nitrogen excitation and dissociative reactions by R_{23-28}, H_2O reactions by R_{29-31} and oxygen negative ion reactions by R_{32-46} in table 3.1. An important characteristic of this reaction scheme is that it lumps the excited helium states into a single species He^* and assumes the various excimer levels decay into a single level He_2^* ($a^3\Sigma_u^+$) denoted as He_2^*. A destruction frequency of 10^4 s^{-1} is taken for He_2^* here [44]. Electron detachment (R_{39-46} in table 3.1) reactions R_{42} and R_{46} are dependent on the atomic oxygen density. Steady state atomic oxygen density develops on much larger timescales ($\sim$ seconds) compared with the 100 μs timescale of the charged species behaviour. In order to approximate the atomic oxygen density a fixed value based on O_2 depletion rates of 0.3% conversion of O_2 to O is used here. This depletion rate is consistent with values reported in literature [91, 92]. Air impurities in the helium carrier gas are assumed to be made up of 79% N_2, 20 % O_2 and 1% H_2O.

The boundary conditions used for plasma species at the dielectric are wall boundary conditions described in section 2.2.5. Surface charge accumulation at the dielectric barrier is described by an additional ordinary differential equation consisting of the net current density on the surface (see section 2.2.3). The secondary electron emission coefficient is set to 0.01 for each charged and excited species impacting the walls. Mesh accuracy was checked by repeating the solution run by consistently doubling the mesh size until solution accuracy was not substantially affected by mesh resolution. For the conditions under study a "quasi" steady state is eventually reached between subsequent applied voltage cycles. Typically 6 - 10 cycles are required before the current density variation over the voltage cycle converges to a steady state.

3.1.2 Results and discussion

Experimental comparison The current in the plasma volume is made up of the electron current, ion (conduction) and displacement current due to the changing electric field. The current density is a volume averaged quantity and for the one dimensional case is given by the following equation [106].

$$J = q_e \int_0^d (\Gamma_{ion} - \Gamma_e)\ dx + J_D \tag{3.1}$$

Ref	Reaction	Rate
R_1 [72]	e + He→He + e	*BOLSIG+*
R_2 [72]	e + He→He* + e	*BOLSIG+*
R_3 [72]	e + He→2e + He$^+$	*BOLSIG+*
R_4 [100]	e + He* →e + He	2.9×10^{-15}
R_5 [44]	e + He_2^+ →He* + He	$8.9 \times 10^{-15}(T_g/T_e)^{1.5}$
R_6 [44]	He$^+$ + 2He→He + He_2^+	1.1×10^{-43}
R_7 [44]	He* + 2He→He + He_2^*	2×10^{-46}
R_8 [44]	He* + He* →e + He_2^+	1.5×10^{-15}
R_9 [44]	He_2^* → 2He	10^4
R_{10} [44]	He_2^* + He_2^* →e + He_2^+ + 2He	1.5×10^{-15}
R_{11} [44]	e + N_2^+ →2N	$4.8 \times 10^{-13}(T_g/T_e)^{0.5}$
R_{12} [44]	He* + N_2 →He + N_2^+ + e	5×10^{-17}
R_{13} [44]	He_2^* + N_2 →2He + N_2^+ + e	3×10^{-17}
R_{14} [44]	He_2^+ + N_2 →He* + N_2^+	1.4×10^{-15}
R_{15} [72]	e + O_2 →2e + O_2^+	*BOLSIG+*
R_{16} [72]	e + O_2 →e + 2O	*BOLSIG+*
R_{17} [72]	e + O_2 →e + O + O (^{1}D)	*BOLSIG+*
R_{18} [101]	e + O_2^+ →2O	$6 \times 10^{-11}T_e^{-1}$
R_{19} [72]	e + O_2 →e + O_2 ($a^1\Delta$)	*BOLSIG+*
R_{20} [101]	N_2^+ + O_2 →N_2 + O_2^+	$1.04 \times 10^{-15}T_g^{-0.5}$
R_{21} [102]	He* + O_2 →He + O_2^+ + e	$2.54 \times 10^{-16}(T_g/300)^{0.5}$
R_{22} [103]	He_2^* + O_2 →2He + O_2^+ + e	$1 \times 10^{-16}(T_g/300)^{0.5}$
R_{23} [72]	e + N_2 →e + N_2 ($A^3\Sigma$)	*BOLSIG+*
R_{24} [72]	e + N_2 → e + N_2 ($B^3\Pi$)	*BOLSIG+*
R_{25} [72]	N_2 ($B^3\Pi$)→N_2 ($A^3\Sigma$)	1.2×10^5
R_{26} [72]	e + N_2 →e + N (^2D) + N	*BOLSIG+*
R_{27} [72]	e + N→e + N (^2D)	*BOLSIG+*
R_{28} [101]	e + N_2^+ →N (^2D) + N	$1.5 \times 10^{-12}/T_e^{0.7}$
R_{29} [72]	e + H_2O→2e + H_2O^+	*BOLSIG+*
R_{30} [104]	e + H_2O^+ →OH + H	$2.73 \times 10^{-12}T_g^{-0.5}$
R_{31} [72]	e + H_2O→e + OH + H	*BOLSIG+*
R_{32} [72]	e + O_2 → O + O^-	*BOLSIG+*
R_{33} [101]	e + O_2 + M → O_2^- + M	$6 \times 10^{-39}T_e^{-1}$
R_{34} [101]	O^- + O_2^+ → O + O_2	$3.464 \times 10^{-12}T_g^{-0.5}$
R_{35} [101]	O_2^- + O_2^+ → 2O_2	$3.464 \times 10^{-12}T_g^{-0.5}$
R_{36} [101]	O^- + O_2^+ + M → O + 2O_2 + M	$3.12 \times 10^{-31}T_g^{-2.5}$
R_{37} [101]	O_2^- + O_2^+ + M → 2O_2 + M	$3.12 \times 10^{-31}T_g^{-2.5}$
R_{38} [91]	O^- + O_2 → O_2^- + O	1.5×10^{-18}
R_{39} [90]	O^- + He → He + O + e	$2.5 \times 10^{-24}(T_g/300)^{0.6}$
R_{40} [105]	O^- + He* → He + O + e	3×10^{-16}
R_{41} [105]	O^- + He_2^* → 2He + O + e	3×10^{-16}
R_{42} [102]	O^- + O → O_2 + e	$5 \times 10^{-16}T_g^{0.5}$
R_{43} [90]	O_2^- + He → He + O_2 + e	$3.9 \times 10^{-16}exp(-7400/T_g)$
R_{44} [105]	O_2^- + He* → He + O_2 + e	3×10^{-16}
R_{45} [105]	O_2^- + He_2^* → 2He + O_2 + e	3×10^{-16}
R_{46} [102]	O_2^- + O → O_3 + e	$1.5 \times 10^{-16}T_g^{0.5}$

Table 3.1: He - Air Plasma chemistry

Notes: (1) R_i (n) - n indicates reference for ith reaction (2) Rates in units $[m^3/s]$, $[m^6/s]$ (3 body reactions), T_g (K) gas temperature, T_e (K) electron temperature except where stated otherwise (3) M represents background gases He, N_2, O_2.

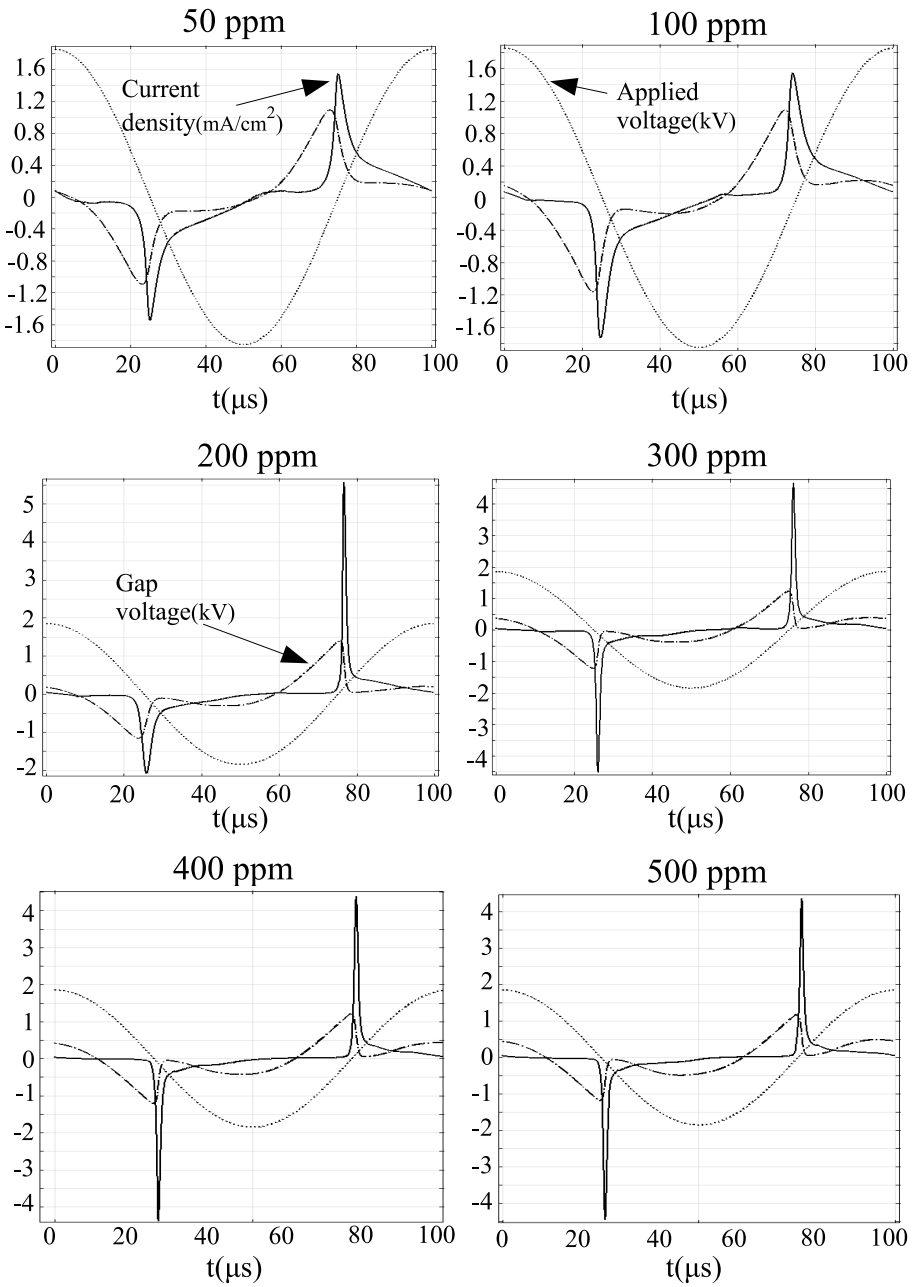

Figure 3.1: Steady state current density (mA/cm^2), gap voltage (kV) and applied voltage (kV) over the applied voltage phase for a helium dielectric barrier discharge across a range of air impurity values (50 - 500 ppm).

where d is the gap distance, q_e electron charge, $\Gamma_{ion,e}$ ion/electron fluxes and J_D the displacement current given by $J_D = \epsilon_0 \frac{\partial V_{RF}}{\partial t}$.

Experimental measurements by Mangolini et al. [11] of interest here estimated an approximate air impurity of the order of $\sim$100 ppm based on an estimation of the pressure chamber leak rate.

A one dimensional simulation to match the experimental conditions described above is run for a range of air impurity values (50 - 500 ppm). Numerical results of current densities are shown in figure 3.1. The periodic nature of the glow mode is shown by a current pulse occurring on every half voltage cycle [8, 9, 11, 107] as the plasma is continually destroyed and formed. The voltage across the plasma (gap voltage V_g) depends on the sum of the applied voltage (V_a) and the voltage induced by surface charge accumulating on the dielectric barriers (memory voltage V_m) given by $V_g = V_a \pm V_m$. The memory voltage V_m opposes the externally applied voltage for most of the applied voltage cycle as surface charge of opposite sign accumulates on the biased dielectric terminals. The memory voltage in this case limits the gap voltage V_g to values below the gas breakdown voltage. When $V_a \to 0$ however $V_g \approx \pm V_m$ which corresponds to a peak in the gap voltage and a subsequent current pulse.

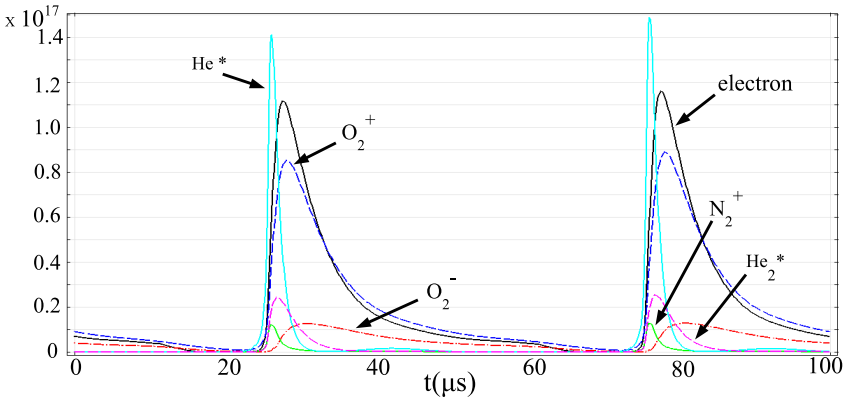

Figure 3.2: Volume averaged charged and excited species density m^{-3} over an applied voltage cycle (steady state) for a helium dielectric barrier discharge with an air impurity of 300 ppm

The volume averaged species number density are shown in figure 3.2 for an impurity value of 300 ppm. Peak He* density of $\sim 1.4 \times 10^{17}$ m^{-3} are found with maximum values occurring once per half cycle. The dominant positive charge carrier is found to be O_2^+ here with peak density of $\sim 8 \times 10^{16}$ m^{-3}. For the dominant negative charge carriers peak electron values of $\sim 1.2 \times 10^{17}$ m^{-3} and peak O_2^- values of $\sim 2 \times 10^{16}$ m^{-3} are shown in figure 3.2 at 300 ppm. The discharge current shown in figure 3.1 is found to depend remarkably on the impurity value. The predominant ionisation source during each current peak is Penning ionisation reactions ($R_{12,13,21,22}$ in table 3.1) of helium excited species (He*, He_2) with molecular air species (N_2, O_2, H_2O). At 300 ppm N_2 Penning ionisation reactions account for 49.9 % of the average (volume and phase) total ionisation while O_2 Penning ionisation reactions account for 48.6 % with a total contribution of 98.5 %. Figure 3.1 shows a transition from a symmetric current profile at 100 ppm air impurity to an asymmetric profile at 200 ppm. For a 300 ppm impurity the symmetric current profile is found to return again with a larger amplitude current density due to the increased ionisation.

The electric field values across the discharge gap is shown in figure 3.3 for an air impurity

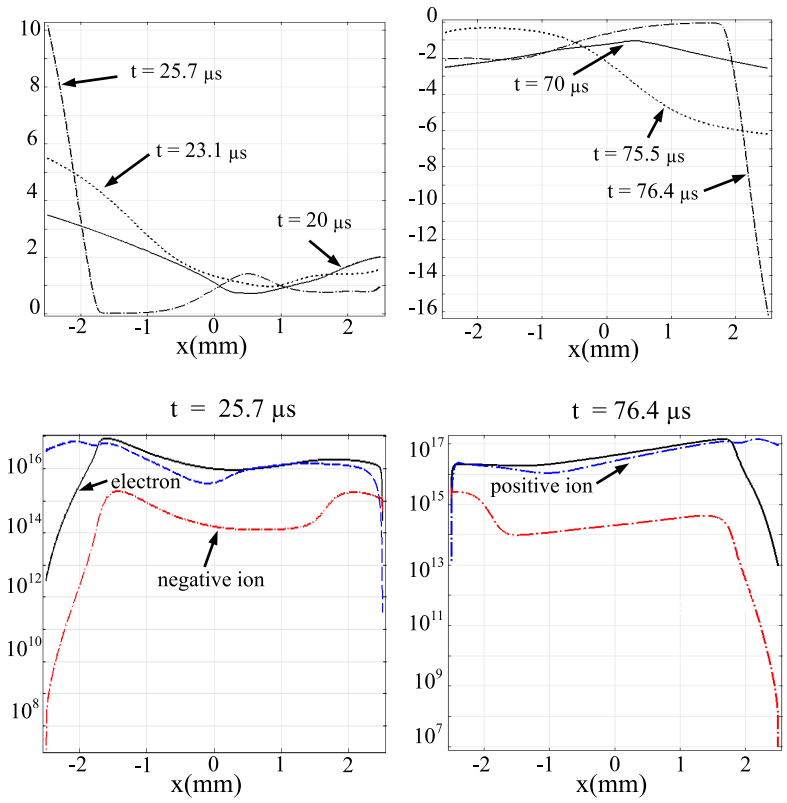

Figure 3.3: Helium dielectric barrier discharge with an air impurity of 200 ppm: Top: electric field kV/m across discharge gap at times near the current density peak. Bottom: charged species density m^{-3} across the discharge gap at current density peak times of t = 25.7 μs and t = 76.4 μs.

of 200 ppm at the gap voltage peak (23.1 μs, 75.5 μs) and current density peak (25.7 μs, 76.4 μs) with the equivalent charged species density at the current density peak shown below. The spatial behaviour of charged species was found to resemble a low pressure direct current glow discharge [1] at the current peak (see figure 3.3) with a sheath of positive space charge (cathode fall) occurring at the momentary cathode as the gap voltage peaks. The spatial structure in subsequent phases of the voltage half cycle follows that of a *sub normal glow* [95]. Quasi neutrality across the gap spatially varies as the sheath grows and shrinks with charge species loss in the gap. Charged and excited species behaviour found here is in good agreement with previous numerical investigations of the helium dielectric barrier discharge with admixed impurities [35, 44, 96, 107]. Figure 3.3 shows that the electric field peak occurs close to the temporary anode on each half cycle. The assymetry in the current density for 200 ppm (see figure 3.6) is shown in figure 3.3 by the different peak electric field values and corresponding charged species densities in each half voltage cycle.

The average electron, O_2^+ and O_2^- ion species number density over the applied voltage phase are shown in figure 3.5 for 200 and 300 ppm air impurity. In the decaying plasma between current pulses negative charge transfer processes are found to dominate over electron recombination

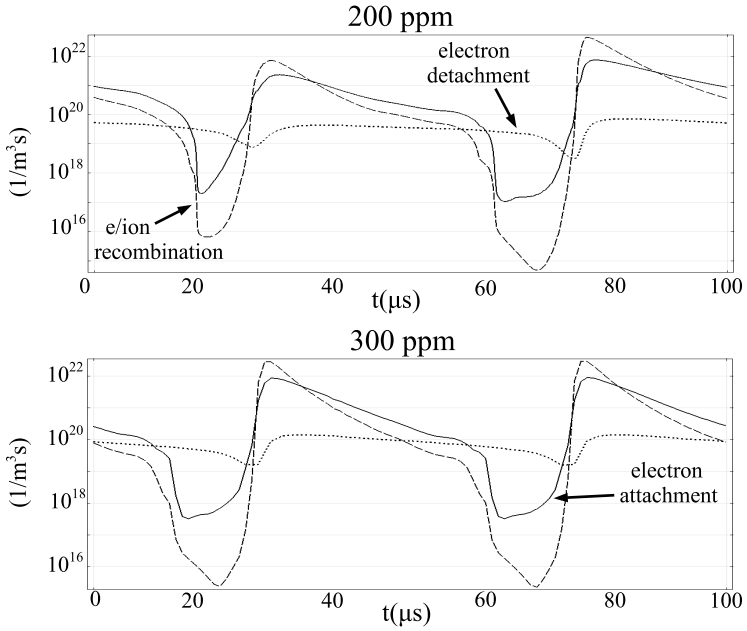

Figure 3.4: Volume averaged electron/ion recombination (reactions $R_{11,15,18,30,28}$ in table 3.1) and electron attachment ($R_{32,33}$ in table 3.1) reaction rates ($m^{-3}s^{-1}$) over an applied voltage cycle for a helium dielectric barrier discharge with an air impurity of 200, 300 ppm

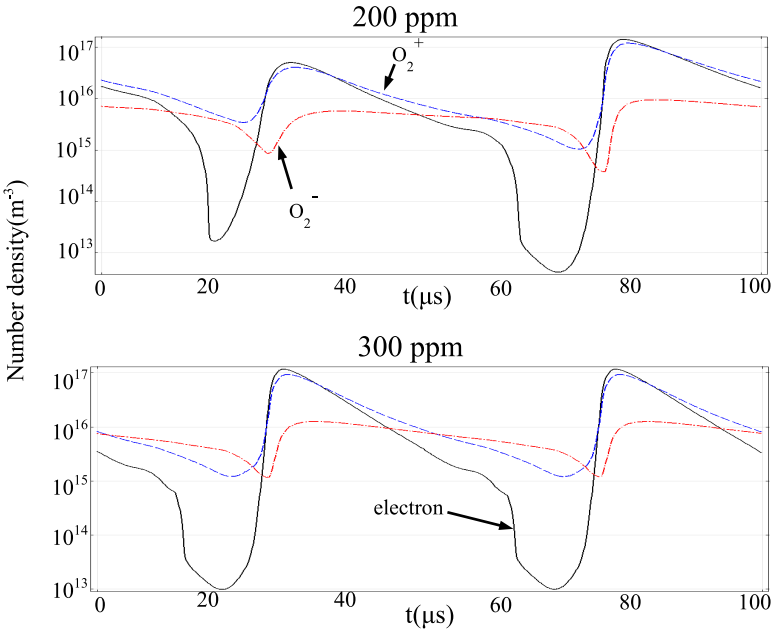

Figure 3.5: Volume averaged charged species density over an applied voltage cycle (steady state) for a helium dielectric barrier discharge with an air impurity of 200, 300 ppm

resulting in an increasingly electronegative plasma. Figure 3.4 shows the volume averaged electron production/loss rate due to recombination, attachment and detachment reactions. When the electron density drop below $\sim 10^{14}$ m^{-3} in the decaying plasma electron detachment reactions are found to become a significant source of electrons here. As the air impurity value is increased to 300 ppm Penning ionization increases the electron density resulting in a reduction of the amplitude of the larger peak and an increase in the amplitude of the smaller peak culminating in a return to a symmetric current profile.

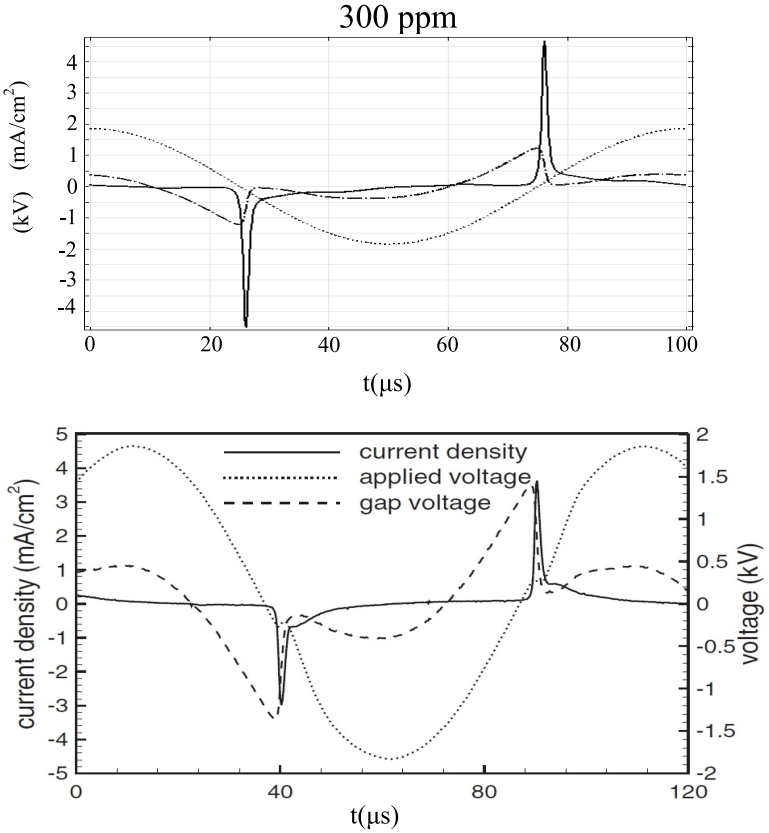

Figure 3.6: Top: steady state current density (mA/cm^2), gap voltage (kV) and applied voltage (kV) for a helium dielectric barrier discharge with an impurity value of 300 ppm. Bottom: equivalent experimentally measured [11] electrical parameters

The equivalent *experimental measurements* [11] of current density are shown in figure 3.6 with the closest matched numerical value of 300 ppm. The current peak width, pulse duration and asymmetry show good agreement here. Asymetries in the experiemnetal results indicate that the true impurity value is possibly between 200 and 300 ppm (see figure 3.6).

Asymmetric current density In the asymmetric current profile results for air impurity of 200 ppm (see figure 3.6) the highest electron density values occurred before the smallest current peak

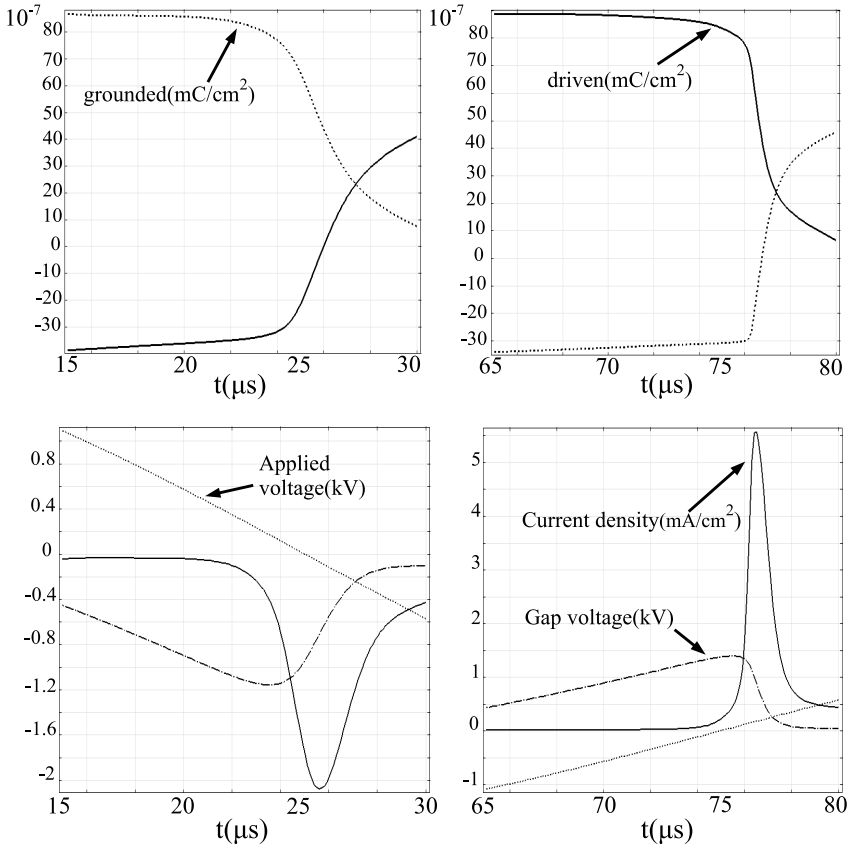

Figure 3.7: Helium dielectric barrier discharge with an air impurity of 200 ppm: Top: Surface charge accumulation (mC/cm^2) on the driven and grounded dielectric. Bottom: equivalent electrical parameters (bottom).

(see figure 3.5). The role of the additional "residual" electron density here is clearly not to provide a level of pre-ionisation for the next breakdown increasing the current density amplitude. The asymmetry in the current profile is attributed primarily to timing of the gas breakdown. Interaction of gap voltage and the residual electron density is found to result in an earlier breakdown before the smaller current peak than for the larger peak. Figure 3.7 shows the surface charge for an air impurity of 200 ppm on the temporary electrodes for two successive current pulses with the corresponding electrical parameters below. The magnitude of surface charge accumulation is similar for both current pulses while the rate of change is significantly different reflecting the asymmetric current behaviour (see figure 3.6). The first *peak in the gap voltage* of -1.149 kV occurs at 23.1 μs here. The externally applied voltage at 23.1 μs is V_a = 0.22 kV which corresponds to a memory voltage of V_a = 1.37 kV. The second peak in the gap voltage of 1.39 kV occurs at a later time of 75.5 μs when the externally applied voltage of V_a = 0.05 kV is much smaller and additive. The memory voltage in this second phase of the applied voltage is a similar value of V_a = 1.34 kV to the first half cycle. The asymmetry in the current density amplitude here is therefore attributed

to an earlier initiation of the gas breakdown. This earlier breakdown is due to a higher residual electron density in the first half cycle. The external voltage is shown here to limit the gap voltage peak at this earlier breakdown resulting in a lower current amplitude. The *current density peak* occurs after the gap voltage maximum in each half of the applied voltage cycle. The first current density peak occurs 2.6 μs after the gap voltage peak at 25.7 μs with a value of 2.146 (mA/cm^2). This compares to 76.4 μs in the second half cycle with a peak value of 5.77 (mA/cm^2). The increase in current amplitude in the second half cycle corresponds to a peak occurring 0.7 μs later than the previous half cycle correlating to a doubling in the time after V_a = 0 (at 25 and 75 μs). This manifests in the broad and narrow current profiles observed in figure 3.6 and higher rates of surface charge accumulation change shown in figure 3.7.

3.2 Conclusion

Physical validation for the plasma model and chemistry used in this work is established by comparison of numerical results with experimental measurements [11]. Comparison of current density behaviour for an atmospheric pressure helium dielectric barrier discharge with variation of air impurity values in the 50 - 500 ppm range is presented. Current profiles between 200 - 300 ppm show good agreement. Investigation of the dielectric barrier discharge in a diffuse mode of operation is characterised by pulsed plasma behaviour. The interplay between the applied voltage and the voltage induced by surface charge accumulated on the dielectric surface results in a peak in gap voltage and current density during each half cycle of the applied voltage. The influence of air impurities is shown to be remarkable here accounting for 98.5 % of the ionisation via reaction between the helium metastable species and N_2, O_2. Electron density typically varies between $\sim 10^{13}$ m^{-3} - 10^{17} m^{-3} within each half cycle of the applied voltage. Negative charge transfer processes are found to dominate over electron recombination as the plasma decays between each current pulse. Electron detachment is shown to overtake electron attachment reactions as the electron density falls below 10^{14} m^{-3} in the latter stage of the plasma decay phase. Asymmetries in the current density profile between air impurity values of 200 ppm - 300 ppm are shown to result from differences in the initiation time of gas breakdown.

Chapter 4

Corona plasma jet

Abstract

A "plasma needle" is a cold plasma source operating at atmospheric pressure. Such sources interact strongly with living cells, but experimental studies on bacterial samples show that this interaction has a surprising pattern resulting in circular or annular killing structures. This chapter presents numerical simulations showing that this pattern occurs because biologically active reactive oxygen and nitrogen species are produced dominantly where effluent from the plasma needle interacts with ambient air. A novel solution strategy is utilised coupling plasma produced neutral (uncharged) reactive species to the gas dynamics solving for steady state profiles at the treated biological surface. Numerical results are compared with experimental reports corroborating evidence for atomic oxygen as a key bactericidal species. Surface losses are considered for interaction of plasma produced reactants with reactive solid and liquid interfaces. Atomic oxygen surface reactions on a reactive solid surface with adsorption probabilities above 0.1 are shown to be limited by the flux of atomic oxygen from the plasma. Interaction of the source with an aqueous surface showed hydrogen peroxide as the dominant species at this interface.

4.1 Introduction

In this chapter a two dimensional numerical study of a corona plasma jet mixing with ambient gases is considered. Such devices have recently proven successful in killing bacteria and altering mammalian cell function highlighting interest for applications in medicine [5, 52, 53]. Reactive species generated due to mixing of atmospheric gases with noble carrier gases such as helium are believed to play a key role in these sources bio-active properties. *S. Mutans* bacterial samples

*Atomic oxygen patterning from a biomedical needle-plasma source, Seán Kelly and Miles M. Turner, Journal of Applied Physics, 114, 123301, 2013, http://dx.doi.org/10.1063/1.4821241

treated by the "plasma needle" source show circular and annular killing structures at different gas flow rates [12]. Optical diagnosis under similar conditions revealed that atomic oxygen produces a similar patterning to this killing structure [54]. The influence of gas mixing on plasma dynamics is investigated here offering fundamental understanding of how bio-active species such as atomic oxygen reach treatment surfaces below these plasma jets. A novel solution strategy is utilised by coupling plasma produced neutral (uncharged) reactive species to the gas dynamics and solving for steady state profiles at the treated surface. Reaction of the plasma produced chemistry at a treatment surface depends on the surface properties. Species profiles over inactive, active and aqueous surfaces are investigated here.

The plasma needle [6] is a cold atmospheric plasma device under study for biomedical applications [5, 52, 53]. The device consists of a thin tungsten wire driven by a radio frequency voltage surrounded by quartz tubing guiding helium flows of up to 2 slpm around the wire. A critical factor in its efficacy is attributed to the mixing of the helium carrier gas with air [12, 54]. Mixing results in generation of *reactive oxygen nitrogen species* (RONS) culminating in oxidative and nitrosative stress to exposed cells. In this chapter we investigate numerically the role of neutral RONS species produced by the plasma needle device with a focus on the atomic oxygen and ozone patterning at the treated surface. Surface losses are discussed in this context where results of the interaction of plasma produced reactants with reactive solid and liquid interfaces are presented.

4.2 Model description

A two dimensional axi-symmetric domain about the pin axis is considered, utilising the devices cylindrical symmetry (see figure 4.1). The dimensions are matched to experimental reports of Goree *et al* [12, 53] and Sakiyama *et al.* [54] on the devices killing pattern of S. Mutans bacteria samples. A 5 mm dielectric barrier ($5\epsilon_0$) sits on a grounded plate at a distance of 3 mm below the RF driven pin. The pin diameter was taken as 0.4 mm with a taper of length 6 mm and tip diameter 0.15 mm.

In the present work, the commercial finite element partial differential equation solver COMSOL Multi-physics (version 4.3a) [65] is used to find a mutually consistent solution for the reacting gas flow (which is assumed to be laminar) and the plasma discharge [65, 108]. Initially, mass and momentum continuity equations (compressible Navier-Stokes) are coupled to a mass transport equation and solved in a steady state manner for a profile of the helium-air mixture. A gas temperature of 330 K is assumed with variable density and dynamic viscosity based on the mixture fraction of gaseous species. Diffusion coefficients for the neutral gas species are calculated from kinetic gas theory using the Leonard-Jones potential parameters [76]. For further information on equation formulation and boundary conditions (figure 4.1) see reports [13, 76].

The stationary helium-air mixture profile is coupled to a self consistent fluid model of the plasma. Continuity equations for the electron density, electron energy and heavy species densities

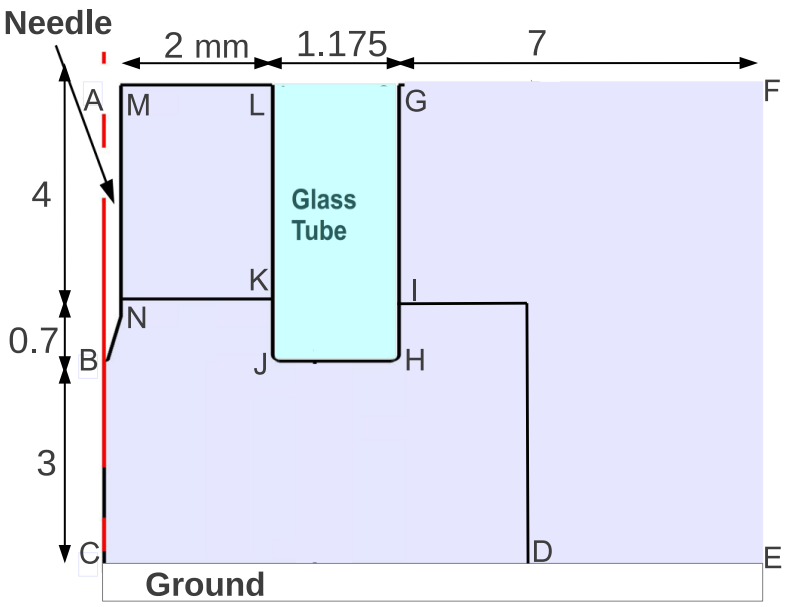

Figure 4.1: Plasma needle geometry [12, 13]

are solved with Poisson's equation for the electric field in the area NBCDIHJK shown in figure 4.1 for CD of length 5 mm. A log substitution ($N_i = ln\, n_i$) for species density n_i from the standard (linear) [109] species continuity equation is used [65]. This model is similar to that of Sakiyama *et al.* [13], who have discussed details such as boundary conditions.

Our model treats a mixture of helium and humid air (1% H_2O, 20% O_2 and 79% N_2). The reaction set is shown in table 4.1, consisting of seven ionic species (He^+, He_2^+, N_2^+, O_2^+, O^-, O_2^- and H_2O^+) with fifteen neutral species (He, He^*, He_2^*, O_2, O_2 ($a^1\Delta$), O, O (^1D), N_2, N_2 ($A^3\Sigma$), N_2 ($B^3\Pi$), N, N (^{2}D), H_2O, OH, and H). Reactions R_{1-14} in table 4.1 follow the He-N_2 reaction scheme of Golubovski et al [44]. The oxygen reaction scheme is given by reactions R_{14-22}, nitrogen reactions by R_{23-28} and H_2O reactions by R_{29-31} in table 4.1. A helium purity of 99.999% is used here. The electron transport and electron impact reaction rates are preprocessed by solving the zero dimensional Boltzmann equation using the *Bolsig+ solver* software [72] with collision cross section data from the *Lxcat* database [3] for a range of helium-air mixtures. The ion transport values are taken from literature [75] and the corresponding diffusion coefficients are calculated using the Einstein relation. The sinusoidal applied voltage with frequency of $f = 13.56MHz$ is given by $V_{applied}Sin(2\pi ft) + V_{dc}$ where $V_{applied}$ is the applied voltage amplitude and V_{dc} represents the self bias voltage due to a serial blocking capacitance component in the matching circuit.

The phase averaged production rates for the neutral species formed by the plasma dynamics are coupled to a mass transport model for the reacting and convecting mixture of neutral species,

Ref	Reaction	Rate
R_1 [72]	e+He→He+e	*BOLSIG+*
R_2 [72]	e+He→He*+e	*BOLSIG+*
R_3 [72]	e+He→2e + He$^+$	*BOLSIG+*
R_4 [100]	e+He* →e+He	2.9×10^{-15}
R_5 [44]	e+He_2^+ →He*+He	$8.9 \times 10^{-15}(T_g/T_e)^{1.5}$
R_6 [44]	He$^+$+2He→He+He_2^+	1.1×10^{-43}
R_7 [44]	He*+2He→He+He_2^*	2×10^{-46}
R_8 [44]	He*+He* →e+He_2^+	1.5×10^{-15}
R_9 [44]	He_2^* → 2He	10^4
R_{10} [44]	He_2^*+He_2^* →e+He_2^++2He	1.5×10^{-15}
R_{11} [44]	e+N_2^+ →2N	$4.8 \times 10^{-13}(T_g/T_e)^{0.5}$
R_{12} [44]	He*+N_2 →He+N_2^++e	5×10^{-17}
R_{13} [44]	He_2^*+N_2 →2He+N_2^++e	3×10^{-17}
R_{14} [44]	He_2^++N_2 →He*+N_2^+	1.4×10^{-15}
R_{15} [72]	e+O_2 →2e + O_2^+	*BOLSIG+*
R_{16} [72]	e+O_2 →e+2O	*BOLSIG+*
R_{17} [72]	e+O_2 →e+O+O (^{1}D)	*BOLSIG+*
R_{18} [101]	e+O_2^+ →2O	$6 \times 10^{-11}T_e^{-1}$
R_{19} [72]	e+O_2 →e+O_2 ($a^1\Delta$)	*BOLSIG+*
R_{20} [101]	N_2^++O_2 →N_2+O_2^+	$1.04 \times 10^{-15}T_g^{-0.5}$
R_{21} [102]	He*+O_2 →He+O_2^++e	$2.54 \times 10^{-16}(T_g/300)^{0.5}$
R_{22} [103]	He_2^*+O_2 →2He+O_2^++e	$1 \times 10^{-16}(T_g/300)^{0.5}$
R_{23} [72]	e+N_2 →e+N_2 ($A^3\Sigma$)	*BOLSIG+*
R_{24} [72]	e+N_2 → e+N_2 ($B^3\Pi$)	*BOLSIG+*
R_{25} [72]	N_2 ($B^3\Pi$)→N_2 ($A^3\Sigma$)	1.2×10^5
R_{26} [72]	e+N_2 →e+N (^2D)+N	*BOLSIG+*
R_{27} [72]	e+N→e+N (^2D)	*BOLSIG+*
R_{28} [101]	e+N_2^+ →N (^2D)+N	$1.5 \times 10^{-12}/T_e^{0.7}$
R_{29} [72]	e+ H_2O→2e + H_2O^+	*BOLSIG+*
R_{30} [104]	e+H_2O^+ →OH+H	$2.73 \times 10^{-12}T_g^{-0.5}$
R_{31} [72]	e+H_2O→e+OH+H	*BOLSIG+*
R_{32} [72]	e+O_2 → O+O^-	*BOLSIG+*
R_{33} [101]	e+2O_2 → O_2^- + O_2	$6 \times 10^{-39}T_e^{-1}$
R_{34} [101]	O^- + O_2^+ → O + O_2	$3.464 \times 10^{-12}T_g^{-0.5}$
R_{35} [101]	O_2^- + O_2^+ + M → 2O_2 + M	$3.12 \times 10^{-31}T_g^{-2.5}$

Table 4.1: He - Air Plasma chemistry

which is solved over larger timescales ($t \sim 0.1$ s). These neutrals react to form ozone O_3 (see

Ref	Reaction	Rate Coefficient
R_1 [110]	O+O+M→O_2+M	2.15×10^{-46}exp (345/T_g)
R_2 [110]	O+O_2+M→O_3+M	$6.9 \times 10^{-46}(300/T_g)^{1.25}$
R_3 [110]	O+O_2+O→O_3+O	2.15×10^{-46} exp (345/T_g)
R_4 [110]	O+O_2+O_3 →2O_3	4.6×10^{-47}exp (1050/T_g)
R_5 [110]	O+O_3 →2O_2	1.8×10^{-17}exp (-2300/T_g)
R_6 [104]	O+O (^{1}D) →2O	8×10^{-18}
R_7 [102]	O (^{1}D)+M →O+M	1×10^{-19}
R_8 [104]	O (^{1}D)+O_3 →2O+O_2	1.2×10^{-16}
R_9 [111]	O (^{1}D)+O_2 ($a^1\Delta$)→O+O_2	1.0×10^{-17}
R_{10} [104]	O (^{1}D)+O_2 →O+O_2 ($a^1\Delta$)	1.0×10^{-18}
R_{11} [112]	O_2 ($a^1\Delta$)+O_3 →O+2O_2	5.2×10^{-17}exp (-2840/T_g)
R_{12} [113]	O_2 ($a^1\Delta$)+M → O_2+M	2.01×10^{-26}
R_{13} [102]	O_3+M → O+O_2+M	1.56×10^{-15}exp (-11490/T_g)
R_{14} [110]	O_3+O_3 →O+O_2+O_3	1.65×10^{-15}exp (-11400/T_g)

Table 4.2: Oxygen chemistry

table 4.2), various nitrogen-oxygen species N_xO_x (table 4.3), hydrogen-oxygen species H_xO_x (table 4.4) and hydrogen-oxygen-nitrogen HNO_x species (table 4.4 (R_{14-18})). The short lived reactive neutrals (N (^{2}D), N_2 ($A^3\Sigma$), N_2 ($B^3\Pi$), He*, H and O (^1D)) formed during the plasma dynamics do not convect or diffuse considerably during this stage of the model.

4.3 Results and Discussion

4.3.1 Plasma structure

The plasma model is solved for $V_{applied}$ = 800 V, 900 V and 1000 V for helium flows of 0.4, 0.5, 0.75 and 1 $slpm$ until the average power deposited (P_{av}) reaches a steady state ($t \sim 10$ μs) ($\delta P_{av} < 5\%$) corresponding to convergence in reactive neutral species production. The phase averaged electron density is shown in figure 4.2. A plasma with density $\sim 10^{20}$ m^{-3} forms around the needle tip, but this rapidly decreases to $\sim 10^{16}$ m^{-3} in the downstream region. A thin sheath structure is formed extending from the tip along the needle sides consistent with a high power mode reported for corona discharges of this type [13].

The phase averaged electron mean energy (see figure 4.2) displays peak values over 22 eV near the needle tip, due to the high electric field and the large curvature of the needle at this point. At the sides of the pin, electron mean energy values up to 14 eV are observed. Peak values drop in the bulk of the discharge where the mean electron energy is typically 1-2.5 eV (figure 4.2). These bulk values of electron energy are a key factor in providing the energy required to disassociate and excite air species, and to generate reactive neutral species.

Ref	Reaction	Rate Coefficient
R_1 [112]	N+O+M→NO+M	6.3×10^{-45} exp (140/T_g)
R_2 [104]	N+N+M→N_2+M	8.3×10^{-46} exp (500/T_g)
R_3 [112]	N+O_2 →NO+O	1.5×10^{-17} exp (-3600/T_g)
R_4 [112]	N+NO→N_2+O_2	2.1×10^{-17} exp (100/T_g)
R_5 [104]	N+NO_2 →N_2O+O	5.8×10^{-18} exp (220/T_g)
R_6 [112]	N+OH→H+NO	7.5×10^{-17}
R_7 [112]	N(^2D)+M→N+M	5×10^{-18} exp (-1620/T_g)
R_8 [101]	N(^2D)+O_2 →NO+O (^{1}D)	6×10^{-18} (T_g/300)$^{0.5}$
R_9 [101]	N(^2D)+NO→N_2O	6×10^{-17}
R_{10} [101]	N(^2D)+NO→N_2+O	4.5×10^{-17}
R_{11} [112]	N_2 ($A^3\Sigma$)+M→N_2+M	2.2×10^{-20}
R_{12} [101]	N_2 ($A^3\Sigma$)+O→NO+N(^2D)	7×10^{-18}
R_{13} [101]	N_2 ($A^3\Sigma$)+O_2 →N_2+2O	2.54×10^{-18}
R_{14} [101]	N_2 ($A^3\Sigma$)+N_2O→ N_2+N+NO	1×10^{-17}
R_{15} [112]	N_2 ($A^3\Sigma$)+NO_2 → N_2+NO+O	1.3×10^{-17}
R_{16} [112]	NO+O+M→NO_2+M	$1 \times 10^{-43}(300/T_g)^{1.6}$
R_{17} [112]	NO+O_3 →NO_2+O_2	1.8×10^{-18} exp (-1370/T_g)
R_{18} [112]	NO_2+O_3 →NO_3+O_2	1.4×10^{-19} exp (-2470/T_g)
R_{19} [113]	NO_2+NO_3+M→N_2O_5+M	2.8×10^{-42} (300/T_g)$^{3.5}$
R_{20} [112]	NO_2+O→NO+O_2	6.5×10^{-18} exp (120/T_g)
R_{21} [112]	NO_2+O (^{1}D)→NO+O_2	1.4×10^{-16}
R_{22} [113]	N_2+O (^{1}D)+M→N_2O+M	9×10^{-49}
R_{23} [112]	N_2O+O (^{1}D)→NO+NO	1.4×10^{-16}
R_{24} [112]	NO_3+O→NO_2+O_2	1.7×10^{-17}
R_{25} [113]	N_2O_5+M→NO_2+NO_3+M	$((300 \times 10^{-9})/T_g)^{3.5}$ × exp (-11000/T_g)

Table 4.3: Nitrogen - oxygen chemistry

The helium metastable species He^* and He_2^* follow a similar spatial pattern to the plasma density with peak values of 10^{21} m^{-3} for He^* (see figure 4.3) and 10^{20} m^{-3} for He_2^* along the needle tip and sides. The He_2^+ ion is the dominant ionic species at the needle tip (see figure 4.3). This is due to the relatively small amount of impurity present in this region (~ 10 ppm). Stepwise ionisation (R_8, R_{10} in table 4.1) and the fast charge transfer reaction between He^+ and He_2^+ result in a dominance of the He_2^+ ion around the needle tip. Away from the tip, N_2^+ becomes the dominant ionic species (figure 4.3) with peak values of 10^{17} m^{-3} near the central region approximately 1 mm below the pin. This is due to charge transfer reactions (R_{14} in table 4.1) and increased penning ionisation (R_{12}, R_{13}) with increasing nitrogen in the gas mixture. The charge transfer reaction between N_2^+ and O_2^+ (R_{20} in table 4.1) dominates the ion density in the outer radial region away

Ref	Reaction	Rate Coefficient
R_1 [114]	H+H+M→H_2+M	$1.8 \times 10^{-42}/T_g$
R_2 [29]	H+O+M→OH+M	1.62×10^{-44}
R_3 [113]	H+O_2+M→HO_2+M	$5.4 \times 10^{-44}(T_g/300)^{-1.8}$
R_4 [114]	H+OH+M→H_2O+M	$6.1 \times 10^{-38}/T_g^2)$
R_5 [104]	H+O_3 →OH+O_2	$2.8 \times 10^{-17}(T_g/300)^{0.75}$
R_6 [113]	H+HO_2 →H_2+O_2	5.6×10^{-18}
R_7 [113]	H+HO_2 →H_2O+O	2.4×10^{-18}
R_8 [115]	H+H_2O_2 →OH+H_2O	1.69×10^{-17} exp (-1800/T_g)
R_9 [104]	H+NO_2 →OH+NO	1.47×10^{-16}
R_{10} [104]	H+NO_3 →OH+NO_2	5.8×10^{-16} exp (750/T_g)
R_{11} [104]	H+HNO_2 →H_2+NO_2	2×10^{-17} exp (-3700/T_g)
R_{12} [116]	H+HNO_3 →H_2O+NO_2	$1.39 \times 10^{-20}(T_g/298)^{3.29}$ $\times$ exp (-3160/T_g)
R_{13} [104]	OH+O→H+O_2	2.2×10^{-17} exp (-350/T_g)
R_{14} [104]	OH+O_3 →HO_2+O_2	1.6×10^{-18} exp (-1000/T_g)
R_{15} [29]	OH+OH+M→H_2O_2+M	$6.9 \times 10^{-43}(T_g/300)^{-0.8}$
R_{16} [104]	OH+OH→O+H_2O	8.8×10^{-18} exp (-503/T_g)
R_{17} [104]	OH+H_2 →H+H_2O	3.2×10^{-17} exp (-2600/T_g)
R_{18} [113]	OH+H_2O_2 →HO_2+H_2O	2.9×10^{-18} exp (-160/T_g)
R_{19} [112]	OH+NO+M→HNO_2+M	$7.4 \times 10^{-43}(300/T_g)^{2.4}$
R_{20} [112]	OH+NO_2+M→HNO_3+M	$2.2 \times 10^{-42}(300/T_g)^{2.9}$
R_{21} [113]	OH+NO_3 →HO_2+NO_2	2×10^{-17}
R_{22} [29]	OH+HNO_2 →NO_2+H_2O	1.8×10^{-17} exp (-390/T_g)
R_{23} [112]	OH+HNO_3 →NO_3+H_2O	1.5×10^{-20} exp (650/T_g)
R_{24} [113]	HO_2+O_3 →OH+2O_2	1.4×10^{-20} exp (-600/T_g)
R_{25} [113]	HO_2+HO_2 →H_2O_2+O_2	2.2×10^{-19} exp (600/T_g)
R_{26} [117]	HNO_2+HNO_3 →2NO_2+H_2O	1.6×10^{-23}

Table 4.4: Hydrogen-nitrogen-oxygen chemistry

from the tip (figure 4.3) with peak O_2^+ values of 10^{17} m^{-3} occurring approximately 2 mm below the pin and 1.5 mm from the central region. H_2O^+ ions follow a similar distribution to O_2^+ with peak values of 10^{16} m^{-3} outside the central region.

Negative ions play a dominant role in the outer regions of the discharge (see figure 4.4) as the fraction of O_2 in the gas mixture increases (see figure 4.5 (right)). Peak O^- density of 10^{17} m^{-3} occur at air fractions in the range 10^{-3} to 10^{-2} approximately 2 mm from the centre. An increasing O_2 fraction outside the central region leads to the dominance of O_2^- (see figure 4.4 and reaction R_{33} in table 4.1). Negative ions are the dominant negative charge carrier as the air fraction increases in the range 10^{-2} to 10^{-1}. This eventually leads to a large decrease in the

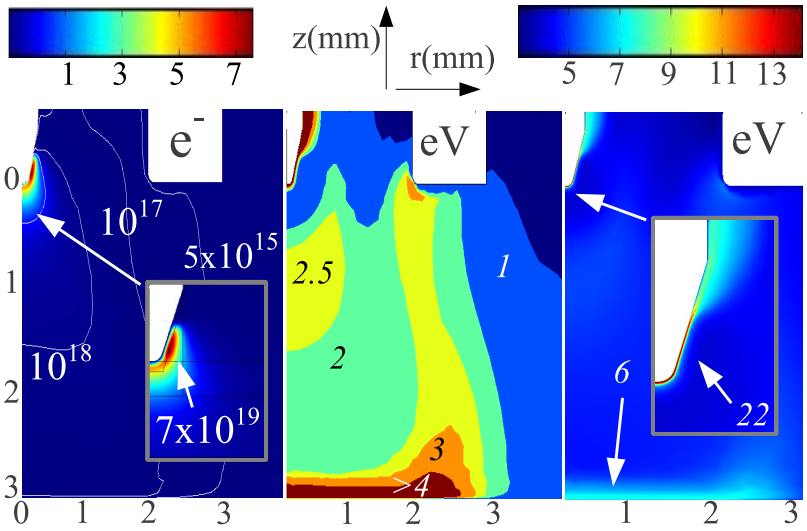

Figure 4.2: Electron (left) phase averaged density m^{-3}, electron energy (filled contour 1-4eV (middle)) and electron energy (right): 0.5 slpm, $V_{applied}$ = 900 V, V_{dc} = 0 V

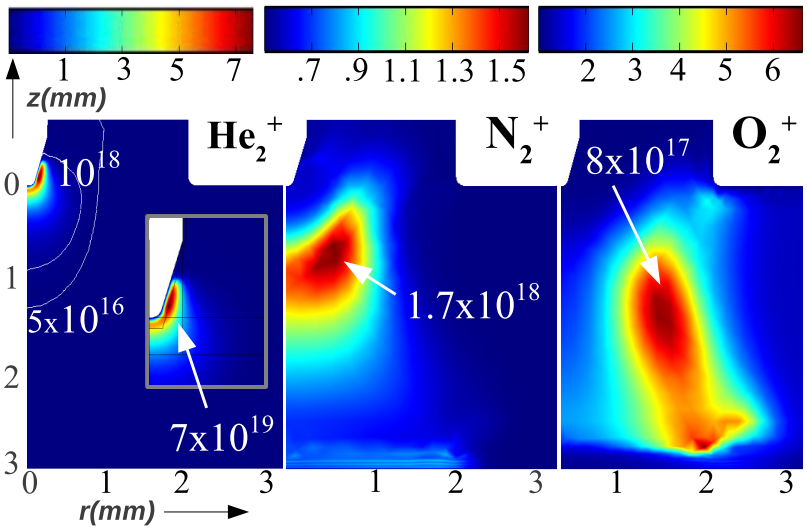

Figure 4.3: He_2^+ (left), N_2^+ (middle) and O_2^+ (right) phase averaged density m^{-3}: 0.5 slpm, $V_{applied}$ = 900 V, V_{dc} = 0 V

plasma density in the outer regions of the discharge as power is increasingly coupled to negative ions over electrons.

4.3.2 Reactive neutrals

The neutral oxygen species produced by the plasma include atomic oxygen O, excited species O (^1D) and the long lived molecular oxygen metastable O_2 ($a^1\Delta$). The phase averaged atomic oxygen production rate is shown in figure 4.5 with corresponding air fraction (right) for a flow

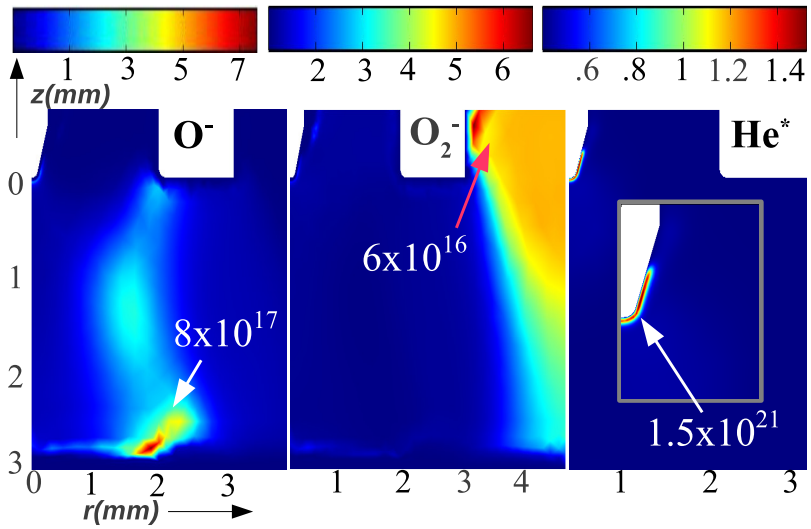

Figure 4.4: O^- (left), O_2^- (middle) and He^* (right) phase averaged density m^{-3}: 0.5 slpm, $V_{applied}$ = 900 V, V_{dc} = 0 V

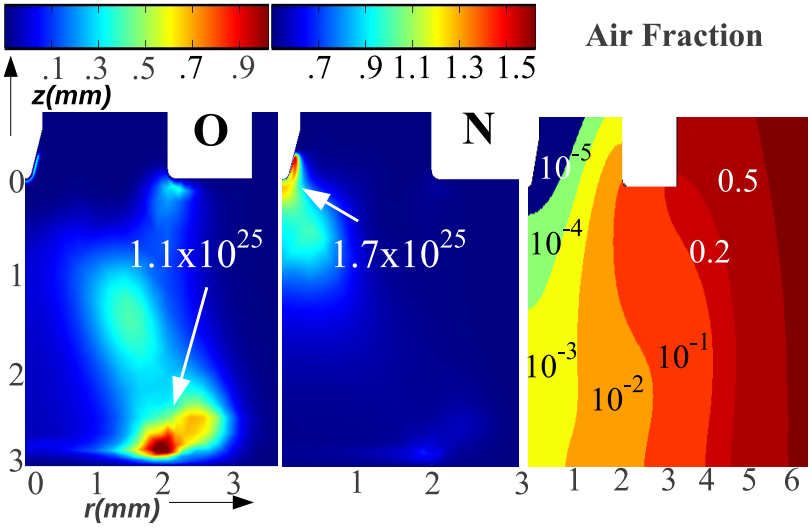

Figure 4.5: O (left), N (middle) phase averaged production rate $m^{-3}s^{-1}$ & air mixture fraction: 0.5 slpm, $V_{applied}$ = 900 V, V_{dc} = 0 V

rate of 0.5 slpm. The spatial peak production of atomic oxygen occurs in the region where the air fraction is of the order 10^{-2} and the plasma density is of the order of 10^{17} m^{-3} (figure 4.2). Values of 1.1×10^{25} $m^{-3}s^{-1}$ are observed in the region of 10^{-3} - 10^{-2} air fraction. Three factors determine the patterning seen here: the interaction of plasma (electron) density, electron energy and the available oxygen density (air fraction). Atomic oxygen is produced via dissociation, due to electron impact by reactions R_{16} and R_{17} with threshold energies of 5.58 eV and 8.4 eV and also by dissociative recombination reaction R_{18} in table 4.1. R_{17} was found to be the dominant reaction

producing atomic oxygen. The production rate of O (^1D) follows a similar pattern to the atomic oxygen production consistent with reaction R_{17} in table 4.1. O_2 ($a^1\Delta$) displays a more diffuse pattern of production in comparison to O and O (^1D) due to its low excitation energy threshold of 0.98 eV. O_2 ($a^1\Delta$) peak production of 5×10^{24} m^{-3} s^{-1} are observed in the region of 10^{-2} air fraction.

The phase averaged N production rates are shown in figure 4.5. Formation of N is by direct dissociation of N_2 (R_{26} table 4.1) and dissociative recombination of N_2^+ (R_{28} table 4.1). The latter reaction proves dominant in the area around the needle tip where N_2^+ ion densities are large. The production rate of N(^2D) follows a similar pattern to the atomic nitrogen production consistent with the chemistry used (R_{27}, R_{28} in table 4.1). The phase averaged N_2 ($A^3\Sigma$) and N_2 ($B^3\Pi$) spatial production patterns show similar behaviour to O_2 ($a^1\Delta$) production with peak values of $3.6-5\times10^{25}$ m^{-3} s^{-1} observed. OH and H are formed via the direct dissociation and dissociative recombination of H_2O and H_2O^+ (R_{29-31} table 4.1) and show a similar production pattern as O. Peak values of 9×10^{22} m^{-3} s^{-1} are found.

4.3.3 Reactive species at surface

The steady state oxygen and ozone distribution on the grounded surface is shown in figure 4.6 for 0.4, 0.5, 0.75 and 1 slpm inlet flows at 900 V. Peak O and O_3 values shift outwards in tandem (separated by approximately 1 mm) as the available air fraction decreases in the central region at higher flows. The decrease in the peak magnitude is due to the lower plasma density and electron energy available outside the central region. At flows of 0.4 slpm peak oxygen values of over 250 ppm (5.5×10^{21} m^{-3}) occur within 2 mm of the centre.

The balance between the competitive reactions in table 4.2 determine the *atomic oxygen-ozone balance* in the region below the pin. Ozone generation is dominated by reaction with helium in the central region and N_2, O_2 outside the central region (R_2 in table 4.2). Quenching of ozone is due to reactions with hydrogen-oxygen radicals (OH, H, HO_2) ($R_{5,14,24}$ in table 4.4) and nitrogen-oxides (NO, NO_2) ($R_{17,18}$ in table 4.3) but is dominated by quenching by O_2 ($a^1\Delta$) (R_{11} in table 4.2) with rate values of the order of 10^{23} m^{-3} s^{-1} across the domain.

The steady state distribution of nitrogen-oxygen species is shown in figure 4.7 for an inlet flow of 0.4 slpm and applied voltage of 900 V. Atomic nitrogen was found in the central region in excess of 17 ppm. Nitrous oxide N_2O was found to be the dominant nitrogen-oxygen species with peak values in the central region of 40 ppm. Values of NO and NO_2 found were less than 13 ppm and 4 ppm peaking in the central region.

Figure 4.7 (right) shows the steady state density for hydrogen-oxygen-nitrogen species. Peak values of 12 ppm hydrogen peroxide H_2O_2 and 8.5 ppm of hydroperoxyl radical HO_2 were found at the treatment surface with maximum values occurring within 5 mm of the centre. Nitrous acid HNO_2 and nitric acid HNO_3 values of less than 5 ppm are shown in figure 4.7 (right).

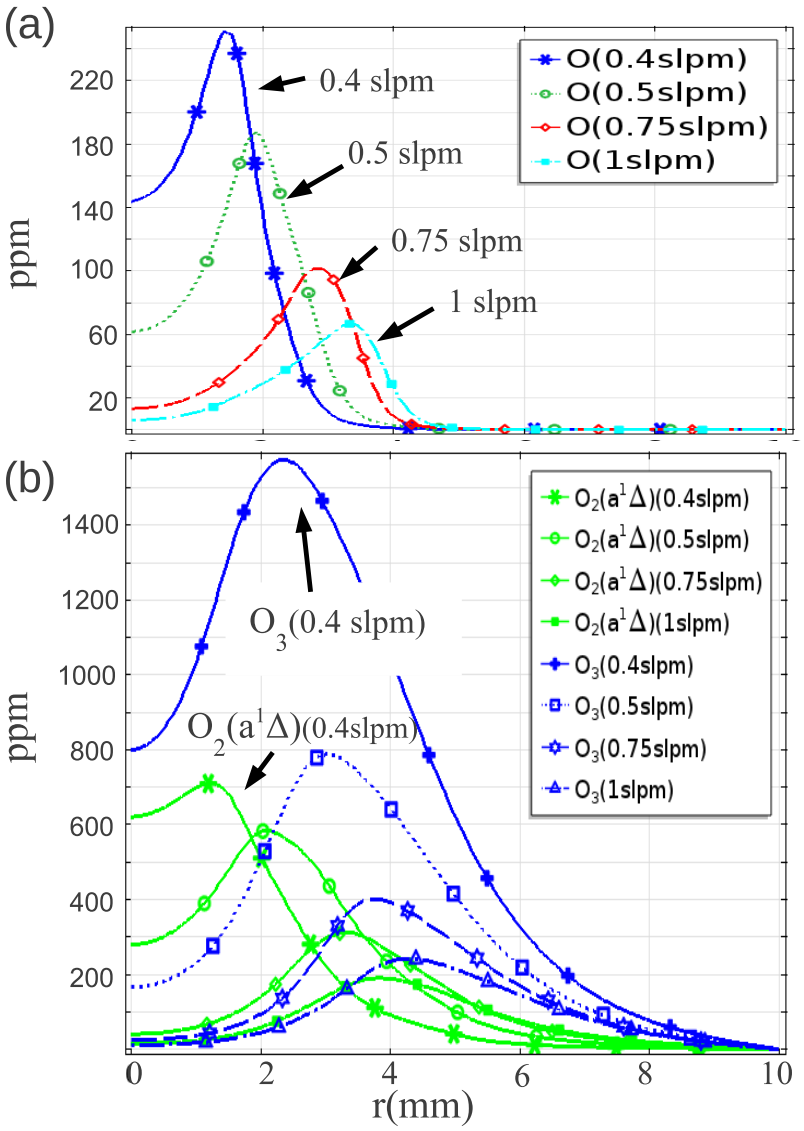

Figure 4.6: O (a) & O_3, O_2 ($a^1\Delta$) (b) on surface (ppm): 0.4 slpm, 0.5 slpm, 0.75 slpm & 1 slpm. $V_{applied}$ = 900 V

4.3.4 Experimental comparison

In this section a comparison of our model results from optical diagnostics on a plasma needle treated surface by Sakiyama *et al.* [54] is discussed. Sakiyama's report presents atomic oxygen density values on a treated surface corroborating earlier studies by Goree *et al* [12, 53] on circular and annular killing patterns observed on plasma needle treated *S. Mutans* bacterial samples. The grounded surface used by Sakiyama in this report is a quartz cuvette (SiO_2) which is a largely *inactive surface* to oxidation by the plasma produced RONS (O, O_3, O_2 ($a^1\Delta$), ..). This allows direct comparison with results discussed in section 4.3.3 for an inactive solid treatment surface

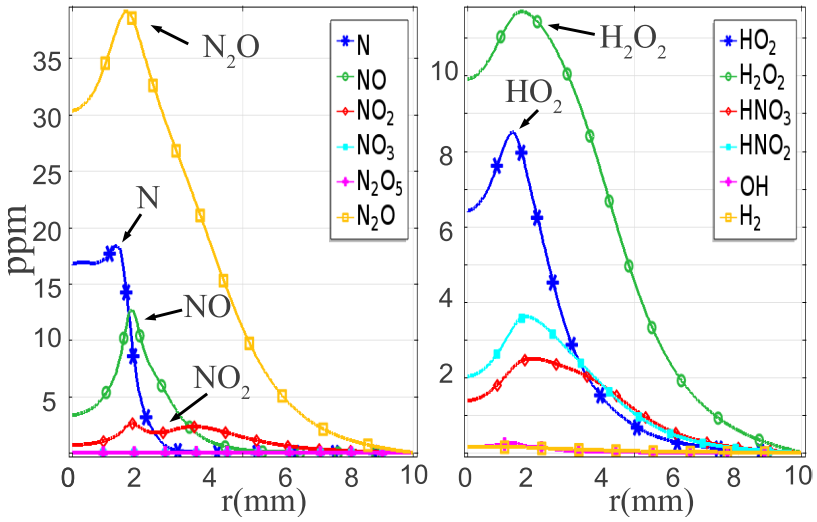

Figure 4.7: Reactive Oxygen Nitrogen Species (RONS) density at surface (ppm): 0.4 slpm, $V_{applied}$ = 900 V

(boundary CE in figure 4.1). Figure 4.8 shows atomic oxygen density at inlet flows of 0.4 slpm and 1 splm for a range of applied voltages. Peak values at 0.5 slpm as reported by Sakiyama et al. show an atomic oxygen density peak of 5×10^{21} m^{-3} within 2 mm of the centre. This is in good agreement with similar peak values for 0.4 slpm at 900-1000 V shown in figure 4.8. At 1 slpm inlet flows Sakiyama reports a peak in the atomic oxygen at 3 mm outside the central region with density of 4×10^{21} m^{-3}. Figure 4.8 shows a similar density peaking at 3 mm but with lower peak values of 2×10^{21} m^{-3}. Such a divergence of results is possibly due to unmatched power conditions used experimentally (applied voltage conditions not reported) or the DC bias voltage which is not accounted for in this numerical study.

4.3.5 Surface interaction

The interaction of plasma produced RONS with *active surfaces* is highly dependent on the surface properties of the material being treated. Atmospheric pressure plasmas have been shown to increase the surface energy (wetability) of various solid surfaces of hydrocarbon polymers such as perspex or polystyrene [118], to kill bacteria, promote wound healing in mammalian cells and kill cancerous cells [15, 16, 119]. These applications occur in both aqueous and dry environments adding to the complexity of interaction. In this section we discuss the interaction of the plasma needle with *reactive* solid and aqueous boundaries in the context of the results presented above.

4.3.5.1 Solid surface interaction

Adsorption of plasma produced RONS on a *dry* solid surface of a non-biological or biological polymer initially causes radical formation which propagates a chain reaction of radical production on the surface. Initial radical formation breaks C-H, C-O and C-C bonds on the polymer surface

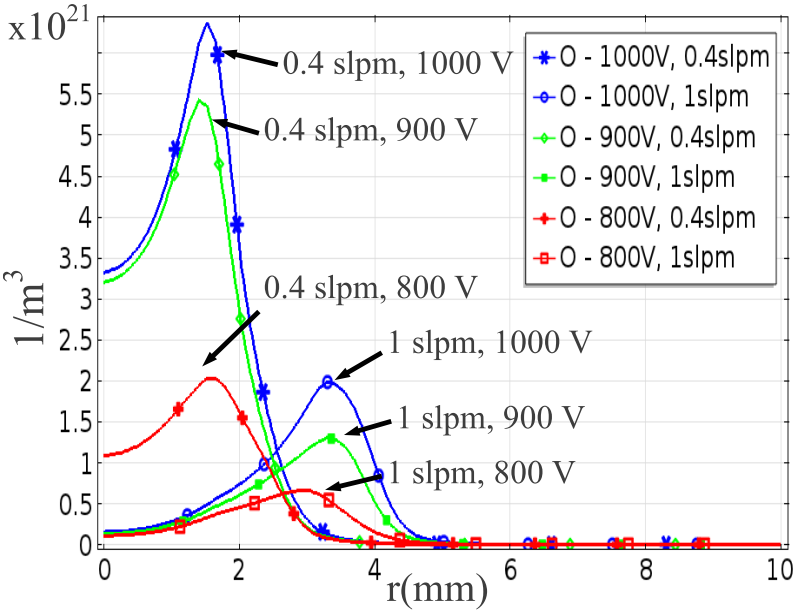

Figure 4.8: Atomic oxygen density at surface (m^{-3}): 0.4 slpm and 1 slpm for $V_{applied}$ = 800, 900, 1000 V

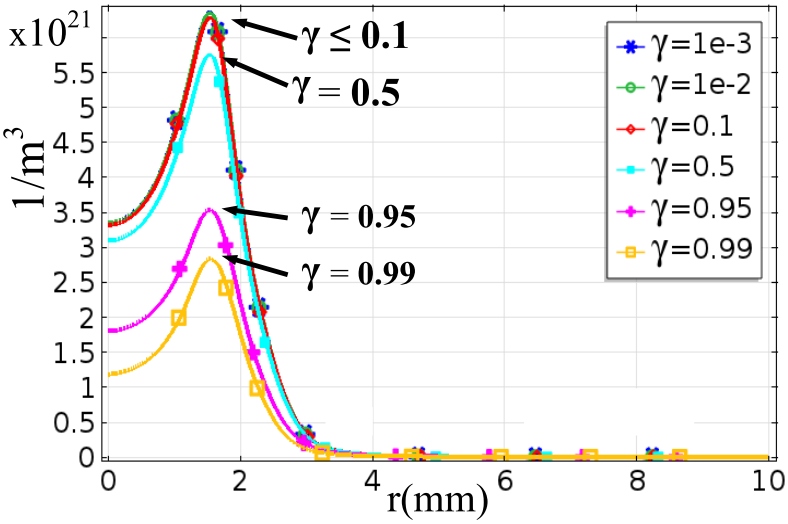

Figure 4.9: Atomic oxygen density at a reactive solid surface (m^{-3}) for a range of adsorption probabilities (γ): 0.4 slpm, $V_{applied}$ = 1000 V

such as peptidoglycan in bacteria cell walls [120], lipid layers in animal cell membranes [121] or plastic materials such as polypropolene [29]. RONS flux loss at a treated surface is primarily dependent on the density of available reaction sites and the reaction rate for each species adsorption. The initiated radical formation on a treated surface is followed by a sequence of radical reactions (propagation) and eventual radical termination often producing a sequence of gaseous by-products which may interact with plasma RONS at the interface. A full model of this interaction for various

surfaces is beyond the scope of this report.

Here we investigate surfaces losses at a reactive treatment surface by considering a simplified model of flux loss for a variety of adsorption probability values (γ) where ($1 > \gamma > 0$) for each species [59]. The flux loss at the treated boundary (CE in figure 4.1) is given by the product $\gamma_i \Gamma_{surf,i}$ where $\Gamma_{surf,i}$ is the normal component of the surface flux for species i. Our reacting gas model is solved using the same flux loss probability γ for O, O_3 and O_2 ($a^1\Delta$) reactive oxygen species [59]. Steady state results for the atomic oxygen density at the treated surface for various reaction probabilities γ are shown in figure 4.9. We see that for values of $\gamma > 0.1$ species density at the surface (central region) begin to drop significantly. Figure 4.9 shows that atomic oxygen surface reactions with reaction/adsorption probabilities $\gamma > 0.1$ will be limited significantly by the atomic oxygen flux from the plasma. Reaction probabilities for atomic oxygen interacting with polypropylene surfaces [29] have been estimated as typically < 0.01 while reaction probabilities on biological polymers such as lipid layers of cell membranes are not yet fully understood.

Ref	Reaction	Rate Coefficient
R_1 [110]	O+H_2O→2OH	1.0×10^{-17} exp (-550/T_g)
R_2 [110]	O+O+H_2O→O_2+H_2O	2.15×10^{-46} exp (345/T_g)
R_3 [110]	O+O_2+H_2O→O_3+H_2O	$6.9 \times 10^{-46}(300/T_g)^{1.25}$
R_4 [79]	O_2 ($a^1\Delta$)+H_2O→O_2+H_2O	3×10^{-24}
R_5 [102]	O_3+H_2O→O+O_2+H_2O	1.56×10^{-15}exp (-11490/T_g)
R_6 [112]	N+O+H_2O→NO+H_2O	6.3×10^{-45} exp (140/T_g)
R_7 [104]	N+N+H_2O→N_2+H_2O	8.3×10^{-46} exp (500/T_g)
R_8 [112]	NO+O+H_2O→NO_2+H_2O	$1 \times 10^{-43}(300/T_g)^{1.6}$
R_9 [113]	NO_2+NO_3+H_2O→N_2O_5+H_2O	$2.8 \times 10^{-42}(300/T_g)^{3.5}$
R_{10} [113]	N_2O_5+H_2O→NO_2+NO_3+H_2O	$1 \times 10^{-9}(300/T_g)^{3.5}$ exp (-11000/T_g)
R_{11} [29]	OH+OH+H_2O→H_2O_2+H_2O	$6.9 \times 10^{-43}(T_g/300)^{-0.8}$ $\times$ exp (-11000/T_g)
R_{12} [112]	OH+NO+H_2O→HNO_2+H_2O	$7.4 \times 10^{-43}(300/T_g)^{2.4}$
R_{13} [112]	OH+NO_2+H_2O→HNO_3+H_2O	$2.2 \times 10^{-42}(300/T_g)^{2.9}$

Table 4.5: Surface H_2O chemistry

4.3.5.2 Water surface interaction

Many application environments such as treatment of living tissues involve biological targets covered in a liquid layer predominately constituted of water. In this scenario the plasma produced RONS are effected remarkably by interaction with a H_2O liquid layer. The gas mixture at the liquid interface is saturated with water vapour which reacts with plasma produced RONS. To estimate this water vapour density we consider the *Antoine equation* allowing the calculation of the (saturated) partial pressure of the water vapour in the gas mixture at the interface [122]. Assuming

a temperature of 293.15 K the partial pressure of H_2O vapour was calculated as 0.023 fraction of the total atmosphere [79]. The average gas density at the surface (boundary CE) for an inlet flow of 0.4 slpm is 2.2 $\times 10^{25}$ m^{-3} giving an average H_2O gas density of 5×10^{23} m^{-3} at the interface. We consider the effects of interaction with this vapour layer on RONS species by including an additional reaction chemistry at the surface CE in our model. An additional chemistry shown in table 4.5 is considered on the boundary CE with a H_2O density 0.023 fraction of the total gas density across the boundary.

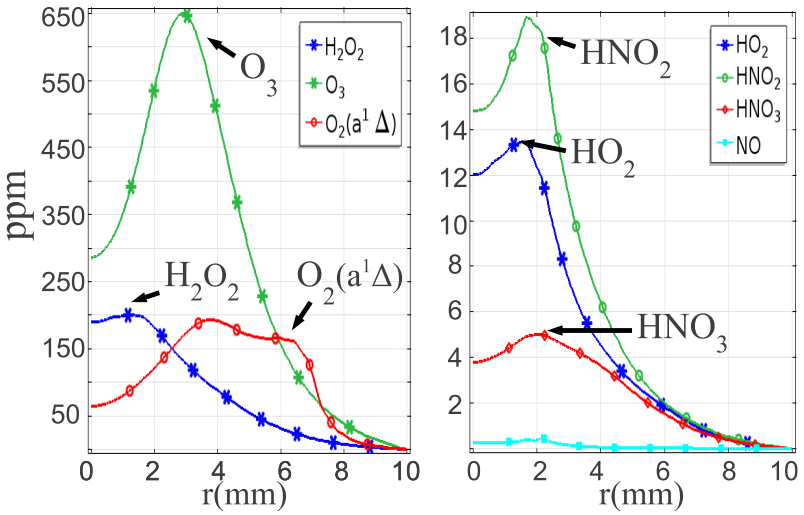

Figure 4.10: Reactive Oxygen Nitrogen Species (RONS) density at water surface (ppm): 0.4 slpm, $V_{applied}$ = 1000 V

Results shown in figure 4.10 represent the non-equilibrium (undissolved) gaseous species density at the water surface for 1000 V applied voltage at an inlet flow of 0.4 slpm. Atomic oxygen reacts strongly with the H_2O vapour layer to form OH (R_1 in table 4.5) which further reacts with H_2O to form hydrogen peroxide H_2O_2 (R_{11} in table 4.5). Reaction of O_3 with the vapour layer results in further O formation. Comparison of O_3 values on an inactive surface show a 50% drop in O_3 density over an aqueous surface. This atomic oxygen production due to O_3 reaction with water is responsible for a more diffuse H_2O_2 pattern on the treated surface when compared with the O spatial pattern over a solid surface. Peak values of H_2O_2 of 200 ppm in the central region are shown in figure 4.10 (left) falling to 50 ppm at 5 mm from the centre. O_2 ($a^1\Delta$) is quenched considerably to O_2 when it interacts with the H_2O vapour layer (R_4 in table 4.5). Comparison of O_2 ($a^1\Delta$) values on an inactive surface show a $\sim$600% drop in density in the central region over an aqueous surface. At 4 mm from the center however O_2 ($a^1\Delta$) actually increases by approximately 100-200% due to the decrease in O_3 before tending to zero beyond 9 mm.

Equilibrium occurs due to dissolution of gaseous species into the water volume which is assumed to proceed reaction at the interface. Henry's law constants shown in table 4.6 represent the concentration ratio of undissolved and dissolved gases once equilibria is reached. If we assume

Species	K_H^{cc}	1/ (1+K_H^{cc})	1/ (1+1/K_H^{cc})
He	1.514e-5	0.99999	1e-5
O_2	5.32e-4	0.9995	5e-4
N_2	2.66e-5	0.99997	3e-5
O_3	4.91e-5	0.99995	5e-5
NO	7.77e-5	0.99992	8e-5
NO_2	1.68e-3	0.998	2e-3
N_2O	1.02e-3	0.999	1e-3
NO_3	7.37e-2	0.93	7e-2
N_2O_5	8.59e-2	0.92	0.08
H_2	3.19e-5	0.99997	3e-5
OH	1.19	0.457	0.543
HO_2	233	4e-3	0.996
H_2O_2	2905	3e-4	0.9997
HNO_2	2.01	0.33	0.67
HNO_3	8593	1e-4	0.9999

Table 4.6: Henry's law constant (solubilities) in water at T=298.15K [14]

that the total available species ($n_{total} = n_{gas} + n_{aqueos}$) for dissolution is equal to the non-equilibrium distributions shown in figure 4.10 the fraction of dissolved and undissolved species in equilibria is given by the ratios 1/ (1+K_H^{cc}) and 1/ (1+1/K_H^{cc}) respectively shown in table 4.6. Table 4.6 clearly shows that H_2O_2, HNO_2, HO_2 and HNO_3 (see figure 4.10 (right)) with solubilities of 99.99%, 67%, 99.6% and 99.99% respectively (given by 1/ (1+1/K_H^{cc})) are the most important species for treatment of aqueous surfaces.

4.4 Conclusion

In this chapter the role of gas mixing in a corona plasma jet source with a helium carrier gas is investigated. The mixing of helium and air species is shown to define the shape and composition of the plasma region. The plasma consists of an electro-positive central region of electrons and positive ions. This core is surrounded by an electro-negative region dominated by positive and negative ion charge carriers. The increasing air fraction in the gas mixture away from the center of the device leads to increasing negative ion dominance over electrons. At the edge of the discharge region high electro-negativity results in poor power coupling as negative ions do not respond as efficiently as electrons to the applied external fields. This dynamic is responsible for the spatial behaviour of the plasma region formed at various gas flow conditions and helium-air mixture profiles.

Peak production of atomic oxygen due to interaction of the plasma with air species occurred at regions of air fraction from 10^{-3} to 10^{-2}. Increasing the gas flow shifted the peak atomic oxygen at the surface from the central to the outer discharge regions correlating to solid circular and annular type atomic oxygen distributions previously reported [12, 54]. Peak atomic oxygen density of 10^{21} and ozone density of 10^{22} m^{-3} were presented here. Surface loss studies revealed that atomic oxygen surface reactions on a reactive solid surface with adsorption probabilities greater than 0.1 are limited by the flux of atomic oxygen from the plasma. Interaction of the source with an aqueous surface showed hydrogen peroxide as the dominant species at this interface with significant hydroperoxyl radical, nitrous acid and nitric acid densities also present.

Chapter 5

Capacitively coupled plasma jet

Abstract

A numerical study of the reactive species generated in a radio frequency capacitively coupled plasma jet operating in the ambient is presented. Generation efficiency of atomic oxygen by O_2 admixing to helium is studied for a range of admixtures and applied voltage conditions. Excessive O_2 admixing lead to negative ion dominance over electrons eventually quenching the plasma. Steady state spatial profiles of reactive uncharged (neutral) species produced by the plasma are presented for a range of surface to device separations. Atomic oxygen is shown to quickly convert to ozone for increasing device to surface separation due to the increasing molecular oxygen present in the gas mixture. Equivalent results for the device mixing in open air (without a solid boundary) show significantly different species density highlighting considerations for accurate source characterisation in either scenario. Gas heating by the plasma is shown to be dominated by elastic electron collisions and positive ion heating. Comparison with experimental measurements for atomic oxygen show good agreement. Interaction of the source with an aqueous surface showed hydrogen peroxide as the dominant species at this interface.

5.1 Introduction

The capacitively coupled source consists of two parallel metallic electrodes representing a planar geometry for plasma generation. Unlike corona sources this design limits significant mixing of ambient air species into the discharge region. Atmospheric gases such as oxygen are typically admixed to the helium carrier gas in order to generate reactive species. In this chapter we investigate the effects of oxygen admixture on plasma behaviour and study the influence of gas dynamics

*Generation of reactive species by an atmospheric pressure plasma jet, Plasma Sources Science and Technology, 23, 6, 065013, 2014, http://dx.doi.org/10.1088/0963-0252/23/6/065013

on reactive species delivery to treatment surfaces. Generation efficiency of atomic oxygen by O_2 admixing to helium is investigated for a range of admixtures and applied voltage conditions. Reactive oxygen species produced by O_2 admixing to the plasma are presented at a range of surface to device separations. Gas heating is of critical importance in applications of atmospheric plasma jets to thermally sensitive surfaces. The influence of gas flow on heating and treatment surface temperatures are investigated here. Reaction of the plasma produced chemistry over inactive, active and aqueous surfaces are discussed.

The *micro-Atmospheric Pressure Plasma Jet* (μAPPJ) [7, 123] source is a low temperature radio-frequency driven plasma jet for research of surface engineering and biomedical applications [5]. The device utilises a planar geometry consisting of 1 mm thick parallel stainless steel electrodes 30 mm in length operated at electrode gaps of 0.5 - 2 mm. Two sides of the discharge region are covered by quartz allowing optical access to the plasma core and guiding helium flows between the electrodes. Typical operational inlet flows [123] remove all atmospheric gases from the discharge region with an admixture of atmospheric gases such as O_2 is added to generate *reactive oxygen nitrogen species* (RONS). One dimensional modelling of the plasma discharge is employed and coupled to two dimensional modelling of the gas dynamics. Phase averaged production rates are extrapolated from the plasma dynamics as a source of reactive neutral species generation in a 2-D model of the jet gas dynamics and neutral species reaction.

This chapter extends on previous numerical studies [56, 61] of the μAPPJ source focusing on issues of reactive species generation and behaviour. The volumetric diffuse α mode of operation [55] for this device is considered. Previous numerical investigations of the plasma dynamics for helium-oxygen mixtures in this source [56, 58, 59, 60, 61, 63, 90] reveal the crucial role of helium metastable in penning ionisation processes [56, 60, 63], the effect of gap size on plasma formation [58, 63] and production mechanisms for atomic oxygen [59, 61]. Global models [90, 91] have revealed the dominant charged and uncharged species in the plasma region allowing subset chemistries for spatially resolved fluid models to be constructed. Yang et al. [59] discussed the behaviour of plasma produced species in the jet effluent in a helium-oxygen atmosphere and its interaction with a reactive surface using a 1-D model and approximations of the gas flow. Hemke et al. [61] used 2-D models of the capacitively coupled jet convecting in a helium-oxygen atmosphere providing further insight into the composition of the jet effluent. The efficiency of reactive species production by admixture of O_2 (section 5.3.1) in the plasma, the subsequent spatial profiles of reactive species produced at various distances below the device (section 5.3.3) and the interaction of plasma produced reactive species with treatment surfaces (section 5.3.5) is discussed. Gas mixing and heating by the plasma is discussed in section 5.3.2. Experimental comparison of the numerical results is discussed in section 5.3.4.

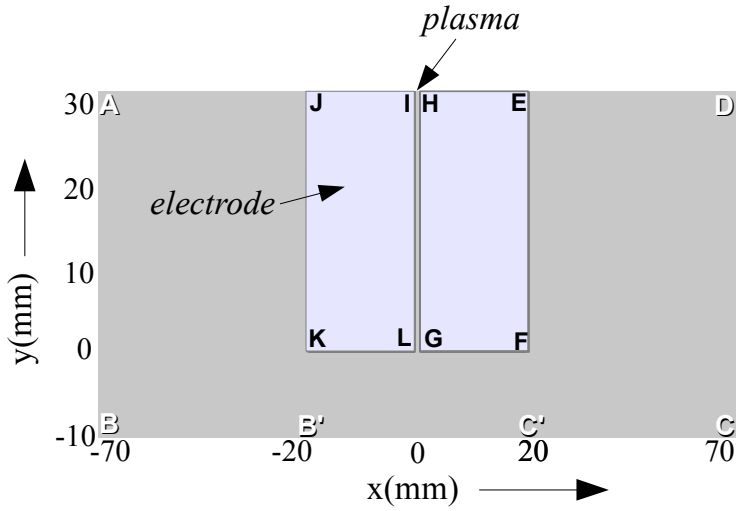

Figure 5.1: Model geometry

5.2 Model description

The model strategy employed in this work exploits the approximate one dimensional (1-D) nature of the plasma dynamics in the μAPPJ source as utilised in previous reports [55, 56, 57, 58, 59, 60]. A 1-D model of the plasma dynamics is initially solved until steady state power conditions are reached. Phase averaged (over the applied voltage phase) reactive neutral (uncharged) species production rates are then extrapolated and coupled to a 2-D model of the reacting and mixing helium carrier jet in the ambient. The use of phase averaged production rates as source terms in a 2-D study of a reacting gas of uncharged species decouples the gas dynamics from the plasma dynamics. This decoupling allows tractable solutions of the neutral species behaviour on the time scale of the gas flow ($\sim$ 0.1 s) which is much larger than the time scale of the plasma dynamics ($\sim$ 0.1 μs). Such a decoupling relies on the assumption that the charged and neutral species produced by the plasma are weakly interacting. The plasma density ($\sim 10^{17}$ m^{-3}) in this context is typically several orders of magnitude lower than the steady state densities of O, O_2 ($a^1\Delta$) and O_3 ($\sim 10^{21}$ m^{-3}) [56, 59, 90]. Uncharged plasma produced species density are therefore not significantly effected by losses due to interaction with charged species. Charged and exited species densities in the plasma may however be changed remarkably by the influence of plasma produced reactive oxygen species. Niemi et al. [60] showed that the helium meta-stables are predominately quenched by penning ionisation with O_2 over O_2 ($a^1\Delta$), O_3 and O interaction. Charge transfer effects due to O_2 ($a^1\Delta$), O_3 and O interaction can change the composition of negative charge carriers depending on the O_2 admxiture [90]. These charge transfer interactions are however not likely to lead to large inaccuracies in the *overall electrical behaviour* of the plasma given the similar reaction pathways and transport properties of these negative charge carriers [90, 91]. Production trends for uncharged reactive species which is of focus in this report are therefore

preserved in this context.

The commercial finite element partial differential equation solver COMSOL Multi-physics (version 4.3a) [65, 108] is used in this report. Continuity equations for the electron density, electron energy and heavy species densities are solved with Poisson's equation for the electric field for a cross section of the planar geometry (see figure 5.1). A log substitution ($N_i = ln\, n_i$) for species density n_i from the standard (linear) species continuity equation is used [65]. The plasma chemistry used in this report consists of six ionic species (He^+, He_2^+, N_2^+, O_2^+, O^- and O_2^- with thirteen neutral species (He, He^*, He_2^*, O_2, O_2 ($a^1\Delta$), O, O (^1D), N_2, N_2 ($A^3\Sigma$), N_2 ($B^3\Pi$), N, N (^{2}D)). Table 5.1 shows the He-O_2 reaction scheme employed here. The He-N_2 chemistry is detailed in chapter 4. A helium purity of 99.999 % is assumed here (10^{-5} air fraction) with the impurity considered to be made up of 20 % O_2 and 80 % N_2. Electron transport and electron impact reaction rates are preprocessed by solving the zero dimensional Boltzmann equation using the *Bolsig+ solver* software [72] coupled with collision cross section data from the *LXcat* database [3] for a range of helium-oxygen mixtures. The ion transport values are taken from literature [75] and the corresponding diffusion coefficients are calculated using the Einstein relation. The sinusoidal applied voltage with frequency of $f = 13.56$ MHz is given by $V_{applied} sin(2\pi ft)$ where $V_{applied}$ is the applied voltage amplitude.

Mass and momentum continuity equations (compressible Navier-Stokes) are coupled to a mass transport equation to study the gas dynamics of the helium jet mixing and reacting in the surrounding air. The two dimensional model geometry is shown in figure 5.1. A variable density and dynamic viscosity based on the mixture fraction of gaseous species is utilised. Diffusion coefficients for the neutral gas species are calculated from kinetic gas theory using the Leonard-Jones potential parameters [76]. The boundary *BC* (see figure 5.1) is a wall (no slip boundary condition). Boundaries *AB*, *CD* *DE* and *AJ* represent gaseous boundaries with the surrounding air. A thermal energy equation in the gas and solid phase is solved for the gas mixture and the electrodes. Thermal conductivity, material density and specific heat capacity values at constant pressure for steel electrodes is taken as 44.5 $W/(mK)$, 7850 kg/m^3 and 475 $J/(kgK)$ respectively. Temperature dependent values for thermal conductivity and specific heat capacity for the gas mixture are used [125]. No heat flux is considered at solid boundaries *IJ*, *EH*, *BC* external to the domain and at gaseous boundaries *DE* and *AJ*. At the other gaseous boundaries *AB*, *CD* and *HI* (see figure 5.1) the temperature is fixed at 293 K. Convective effects on charged species and the electro-hydrodynamic (EHD) force of the plasma on the flow is neglected here. Further information on equation formulation and boundary conditions is given in chapter 2 and reports [13, 61, 76, 126]. A reduced area (*EJB'C'* in figure 5.1) is considered to study helium mixing in open air. In order to stabilise the numerical solution a cross flow is introduced to stabilise the jet [64] using a small inlet flow (< 1 m/s) of air at the boundary *KB'*.

Phase averaged production rates for neutral species formed by the plasma dynamics (1D) are extrapolated across the 30 mm discharge domain ($ILGH$ in figure 5.1) as source terms in the

Ref	Reaction	Rate
R_1 [72]	e+He→He+e	*BOLSIG+*
R_2 [72]	e+He→He*+e	*BOLSIG+*
R_3 [72]	e+He→2e + He$^+$	*BOLSIG+*
R_4 [100]	e+He* →e+He	2.9×10^{-15}
R_5 [124]	e+He_2^+ →He*+He	$5.3 \times 10^{-15}/T_e^{0.5}$
R_6 [44]	He$^+$+2He→He+He_2^+	1.1×10^{-43}
R_7 [44]	He*+2He→He+He_2^*	2×10^{-46}
R_8 [44]	He*+He* →e+He_2^+	1.5×10^{-15}
R_9 [44]	He_2^* → 2He	10^4
R_{10} [44]	He_2^*+He_2^* →e+He_2^++2He	1.5×10^{-15}
R_{11} [72]	e+O_2 →2e + O_2^+	*BOLSIG+*
R_{12} [72]	e+O_2 →e+2O	*BOLSIG+*
R_{13} [72]	e+O_2 →e+O+O (^{1}D)	*BOLSIG+*
R_{14} [101]	e+O_2^+ →2O	$6 \times 10^{-11} T_e^{-1}$
R_{15} [102]	He*+O_2 →He+O_2^++e	$2.54 \times 10^{-16}(T_g/300)^{0.5}$
R_{16} [103]	He_2^*+O_2 →2He+O_2^++e	$1 \times 10^{-16}(T_g/300)^{0.5}$
R_{17} [72]	e+O_2 → O+O^-	*BOLSIG+*
R_{18} [91]	e+ He + O_2 → O_2^- + He	$3.6 \times 10^{-43} T_e[eV]^{-0.5}$
R_{19} [101]	O^- + O_2^+ → O + O_2	$3.464 \times 10^{-12} T_g^{-0.5}$
R_{20} [101]	O_2^- + O_2^+ → O + O_2	$3.464 \times 10^{-12} T_g^{-0.5}$
R_{21} [101]	O^- + O_2^+ + He → O + O_2 + He	$3.12 \times 10^{-31} T_g^{-2.5}$
R_{22} [101]	O_2^- + O_2^+ + He→ 2O_2 + He	$3.12 \times 10^{-31} T_g^{-2.5}$
R_{23} [91]	O^- + O_2 → O_2^- + O	1.5×10^{-18}
R_{24} [72]	e + O_2 → e + O_2 ($a^1\Delta$)	*BOLSIG+*

Table 5.1: He - O_2 Plasma chemistry

Notes: (1) R_i (n) - n indicates reference for i^{th} reaction (2) Rates in units $[m^3/s]$, $[m^6/s]$ (3 body reactions), T_g (K) gas temperature, T_e (K) electron temperature except where stated otherwise (3) M represents background gases He, N_2, O_2.

2-D reacting and mixing gas model. Plasma produced neutrals react to form ozone O_3, various nitrogen-oxygen species N_xO_x and hydrogen-oxygen species H_xO_x. Details oxygen, nitrogen-oxygen and hydrogen-oxygen species reactions used in this chapter are given in chapter 4.

Gas heating by the plasma is considered by inclusion of a phase averaged heating term extrapolated from solutions of the 1-D plasma model across the 30 mm discharge domain ($ILGH$ in figure 5.1) as a source term in a 2-D heat model which is coupled to the reacting and mixing gas model. Ion heating by the electric field, elastic heating between electrons and the background gas and enthalpy contributions from inelastic collisions are considered here [13, 79].

Surface losses at a reactive solid treatment surface (*BC* figure 5.1) are considered using a simplified model of flux loss for a variety of adsorption probability values (γ) where ($1 > \gamma > 0$) [59]. The flux loss at the treated boundary is given by the product $\gamma\Gamma_{surf,i}$ where $\Gamma_{surf,i}$ is the nor-

Ref	Reaction	Rate Coefficient
R_1 [110]	O+H_2O→2OH	1.0×10^{-17} exp (-550/T_g)
R_2 [110]	O+O+H_2O→O_2+H_2O	2.15×10^{-46} exp (345/T_g)
R_3 [110]	O+O_2+H_2O→O_3+H_2O	$6.9 \times 10^{-46}(300/T_g)^{1.25}$
R_4 [79]	O_2 ($a^1\Delta$)+H_2O→O_2+H_2O	3×10^{-24}
R_5 [102]	O_3+H_2O→O+O_2+H_2O	1.56×10^{-15}exp (-11490/T_g)
R_6 [112]	N+O+H_2O→NO+H_2O	6.3×10^{-45} exp (140/T_g)
R_7 [104]	N+N+H_2O→N_2+H_2O	8.3×10^{-46} exp (500/T_g)
R_8 [112]	NO+O+H_2O→NO_2+H_2O	$1 \times 10^{-43}(300/T_g)^{1.6}$
R_9 [113]	NO_2+NO_3+H_2O→N_2O_5+H_2O	$2.8 \times 10^{-42}(300/T_g)^{3.5}$
R_{10} [113]	N_2O_5+H_2O→NO_2+NO_3+H_2O	$1 \times 10^{-9}(300/T_g)^{3.5}$ exp (-11000/T_g)
R_{11} [29]	OH+OH+H_2O→H_2O_2+H_2O	$6.9 \times 10^{-43}(T_g/300)^{-0.8}$ $\times$ exp (-11000/T_g)
R_{12} [112]	OH+NO+H_2O→HNO_2+H_2O	$7.4 \times 10^{-43}(300/T_g)^{2.4}$
R_{13} [112]	OH+NO_2+H_2O→HNO_3+H_2O	$2.2 \times 10^{-42}(300/T_g)^{2.9}$

Table 5.2: Surface H_2O chemistry

mal component of the surface flux for species i. Species flux losses are considered on the treated boundary for a range of adsorption probabilities γ_i in the 2-D reacting gas flow model. Surface reactions are also considered on a liquid covered treatment surface. In this scenario the gas mixture at the liquid interface is saturated with water vapour which reacts with plasma produced *reactive oxygen nitrogen species* (RONS). In order to estimate this water vapour density we consider the *Antoine equation* which allows calculation of the (saturated) partial pressure of the water vapour in the gas mixture at the interface [122]. For a temperature of 293 K the partial pressure of H_2O vapour was calculated as 0.023 fraction of the total atmosphere [79]. An additional chemistry shown in table 5.2 is considered at the treatment boundary coupled with an additional reaction chemistry for the hydrogen-oxygen-nitrogen $H_xN_xO_x$ species generated. Following reaction at the H_2O saturated vapour layer gaseous species dissolve into the water volume. Details of the $H_xN_xO_x$ species reactions considered are given in chapter 4.

5.3 Results & Discussion

Numerical investigations of reactive species production and behaviour in the micro-Atmospheric Pressure Plasma Jet (μAPPJ) as a function of O_2 admixture to helium is discussed. Admixing efficiency results are presented in section 5.3.1. Gas mixing and heating results are presented in section 5.3.2. Section 5.3.3 discusses results of reactive neutral species density and spatial profiles for a range of device to surface separations with comparison to equivalent profiles for a jet convecting from the device into open air. Surface reactions over a solid and aqueous reactive surface are considered in section 5.3.5. Comparison of 2-D numerical results for O_2 admixing with Molecular Beam Mass Spectrometry (MBMS) [62] results is discussed in section 5.3.4.

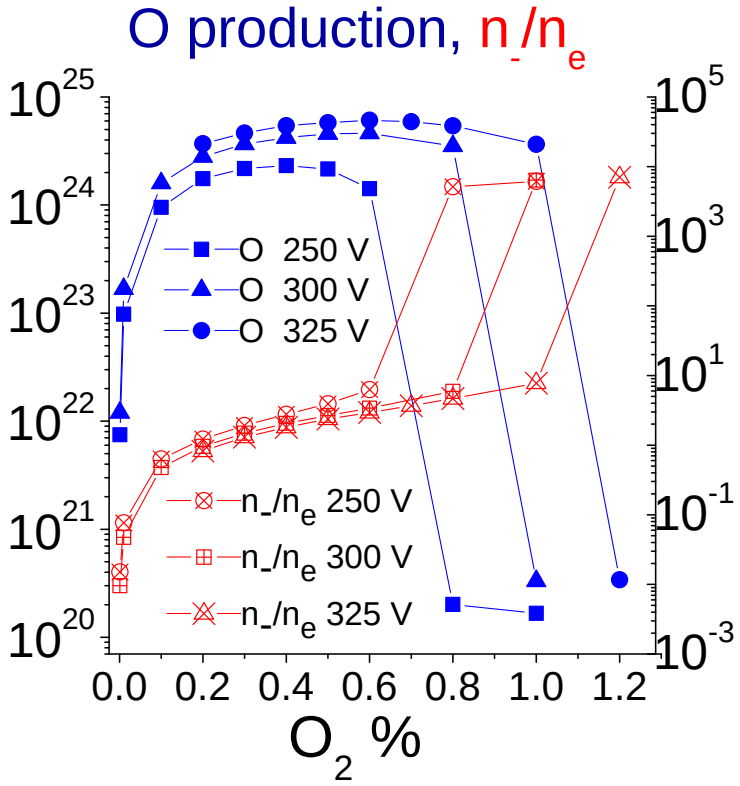

Figure 5.2: Volume and phase (applied voltage phase) averaged O production (left axis) and electronegativity (n_-/n_e) (right axis) for $V_{applied}$ = 250, 300, 325 V for a range of O_2 admixtures

5.3.1 O_2 Admixing efficiency

1-D plasma model results for a cross section of the discharge region are presented in this section for variation in O_2 admixture at an electrode separation of 1 mm for a range of applied voltage conditions ($V_{applied}$ = 250, 300 and 325 V (230 V_{RMS} [62])). Atomic oxygen production results (phase and volume averaged) are shown in figure 5.2. At $V_{applied}$ = 250 V peak O production occurred in the range 0.3 - 0.5 % with production dropping sharply after 0.6 % admixture. Excessive admixing of O_2 increases the plasmas electro-negativity (figure 5.2 (right axis)) reducing power coupling to the electrons (see figure 5.3) which eventually quenches the discharge. At $V_{applied}$ = 300 V peak O production occurred at in the range 0.4 - 0.6 %. Increased power sustains the plasma at higher admixtures before a sharp drop occurs after 0.8 % admixture. At $V_{applied}$ = 325 V peak O production occurred in the range 0.4 - 0.8 %. This result is consistent with previous experimental reports [127, 128] for optimum O_2 admixture for the device operation in the α mode [55]. Increased power again sustains the plasma density at higher admixtures before a sharp drop occurs after 1 % admixture. For admixtures < 0.2 % the power deposited to the plasma at $V_{applied}$ = 325 V increased greatly. This lead to a large growth in discharge current and divergence of our plasma model. This is interpreted to signify a transition towards high current conditions in the

plasma which lead to the formation of a constricted and inhomogeneous plasma. Further investigation of secondary electron emission processes is required to understand this transition clearly and this dynamic is currently beyond the scope of our model. At these lower O_2 admixtures a decrease of electron attachment (reactions R_{29}, R_{30} in table 5.1) occurs and penning ionisation of He^* with O_2 (reactions R_{21}, R_{22} in table 5.1) increases the plasma density towards these high current conditions. At background gas impurity levels of O_2 (2 ppm) the power deposited to the discharge returned to a value of 0.98 W.

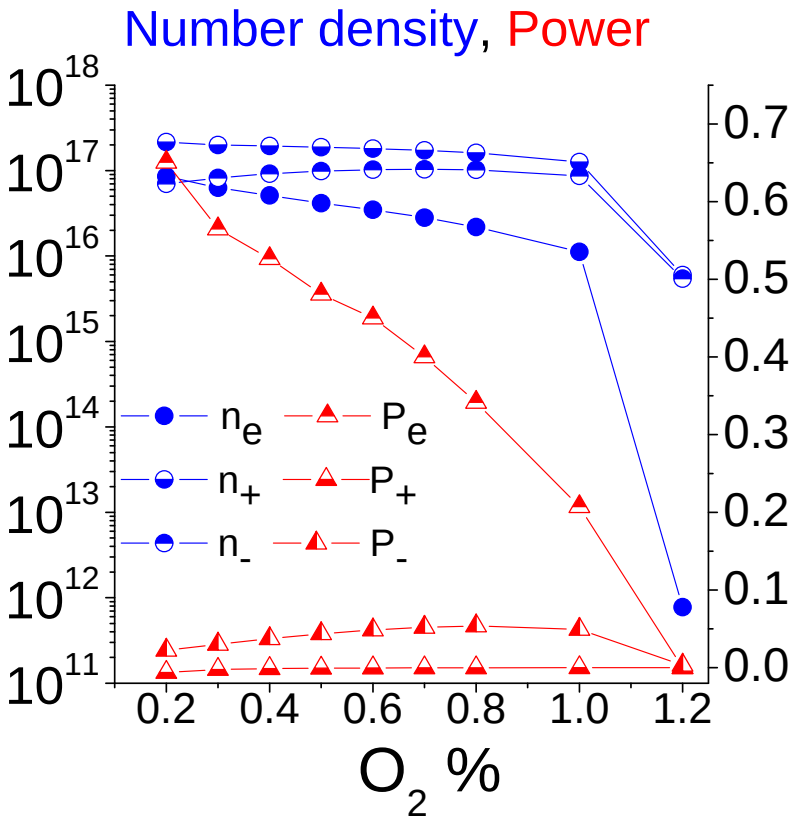

Figure 5.3: Average charged species number density (1/m^3) (left axis) and Power (W) (right axis) for $V_{applied}$= 325 V for a range of O_2 admixtures

Negative ion values shown in figure 5.3 of 2 $\times$ 10^{16} - 1 $\times$ 10^{17} 1/m^3 in the 0.4 - 0.8 % O_2 admixture range correspond to electro-negativity (see figure 5.2 (right)) in the range 1.8 to 4.7. Peak O production at $V_{applied}$ = 325 V occurred at 0.6 % admixture corresponding to an electro-negativity of 2.9. For $V_{applied}$ = 250 V and 300 V peak O production occurred at 0.5 % and at 0.6 % admixtures respectively.

Power coupling and species densities (phase and volume averaged) are shown in figure 5.3 for various admixtures at $V_{applied}$ = 325 V. The volume enclosed by the electrodes is assumed as 30 mm^3 here (30 mm $\times$ 1 mm $\times$ 1 mm). At higher O_2 admixtures the power deposited to negative

ions is found to overtake the electron power deposition. Increased negative ion density leads to a reduction in the electron density and subsequently O production (figure 5.2). Electron density values of the order of 10^{16} 1/m^3 were found at the admixture for peak atomic oxygen production (see figure 5.3) in 0.4 - 0.8 % O_2 admixture range in contrast to electron density values of the order of 10^{12} 1/m^3 at higher O_2 admixtures of 1.2 % where the total power deposited is almost exclusively to negative ions in the plasma. Electron mean energy (phase and volume averaged) values at $V_{applied}$ = 325 V were found to range between 3.922 eV at 0.2 % O_2 admixture, 3.9 eV at 0.5 % to 3.32 eV 1.2 % O_2.

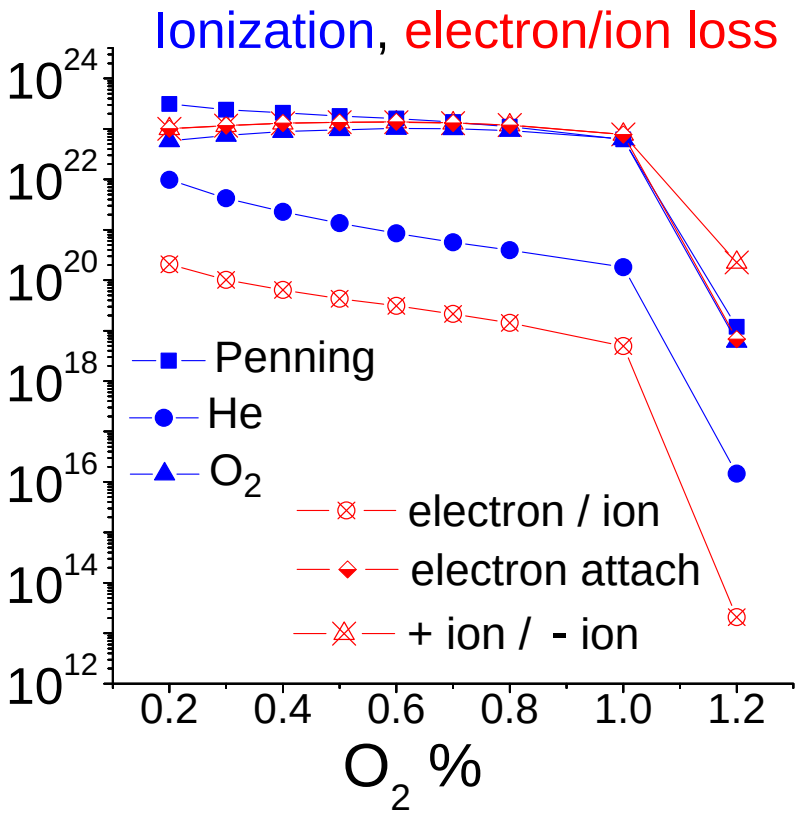

Figure 5.4: Average ionisation reaction rates ($m^{-3}s^{-1}$): Penning ($R_{15,16}$), Helium (R_3), O_2 (R_{11}) (see table 5.1) & electron/ion loss rates ($m^{-3}s^{-1}$): electron-ion recombination ($R_{5,14}$), electron attachment ($R_{17,18}$), O_2 negative/postitive ion recombination (R_{19-22})) for $V_{applied}$= 325 V for a range of O_2 admixtures

Reaction rates for various ionization reactions are shown in figure 5.4 at $V_{applied}$ = 325 V. Penning ionisation ($R_{15,16}$ in table 5.1) of helium metastable species (He^*, He_2^*) with O_2 is shown here as a dominate source of electrons and O_2^+ ions with values of the order 10^{23} 1/m^{3}s at peak O production (O_2 admixture < 0.8 %). Direct ionisation of O_2 (R_{11}) is also significant due to its lower electron energy threshold (12.07 eV) in comparison to direct ionisation of Helium (24.58 eV). Electron and ion loss reaction rates are also shown in figure 5.4 at $V_{applied}$ = 325 V. Negative-positive oxygen ion recombination (R_{19-22}) and electron attachment reactions ($R_{17,18}$) are found

at admixtures < 0.8 % with values of the order 10^{23} 1/m^{3}s. For admixtures > 0.8 % negative-positive oxygen ion recombination reactions dominant as the plasma becomes highly electronegative. Figure 5.5 shows the phase average loss rates of charged species due to collision with the walls. Electron losses dominate here due to there high mobility relative to ions with rate values of the order of 10^{22} 1/m^{3}s for 0.2 - 0.8 % admixtures. At 1.2 % admixture electron wall losses decrease significantly ($\sim 10^{18}$ 1/m^{3}s) correlating to the power loss in the discharge discussed above. Positive ion losses of the order 10^{20} 1/m^{3}s are shown in figure 5.5 with a similar decrease at 1.2 % ($\sim 10^{18}$ 1/m^{3}s) as the plasma density drops. Negative ion wall losses are small here with values of $\sim 10^{16}$ 1/m^{3}s. This is consistent with negative ions being contained in the centre of the discharge between the positive sheath regions at the wall.

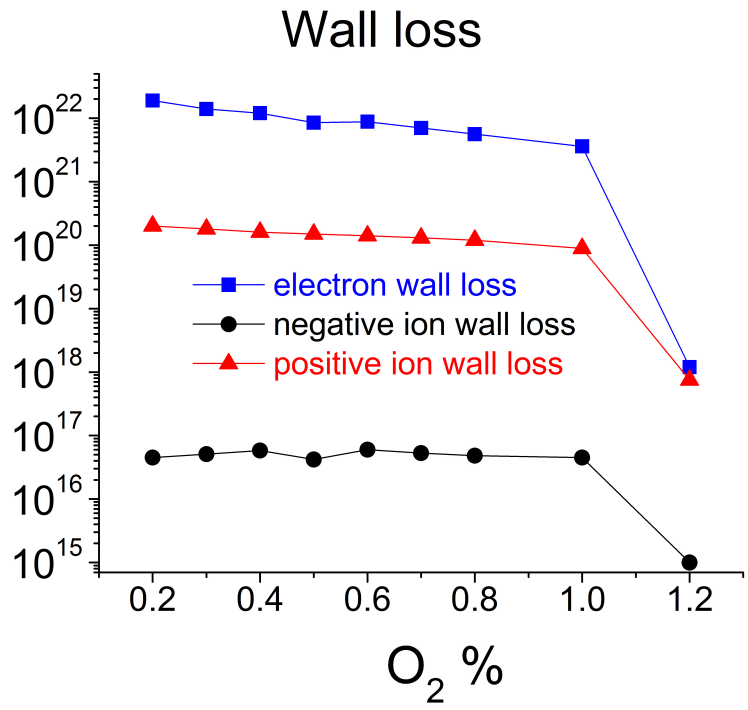

Figure 5.5: Average (phase average) wall loss rates for electrons, total positive and total negative ions 1/m^{3}s

Charged species density (phase averaged) across the discharge domain are shown in figure 5.6 for $V_{applied}$ = 325V and 0.6 % O_2 admixture. O_2^+ is the dominant positive ion here with peak values of 2.8×10^{17} 1/m^3 in the centre of the domain. O^- is the dominant negative charge carrier with peak values of 1.5×10^{17} 1/m^3. O_2^- and electron peak density is 0.8 and 0.6×10^{17} 1/m^3 respectively here.

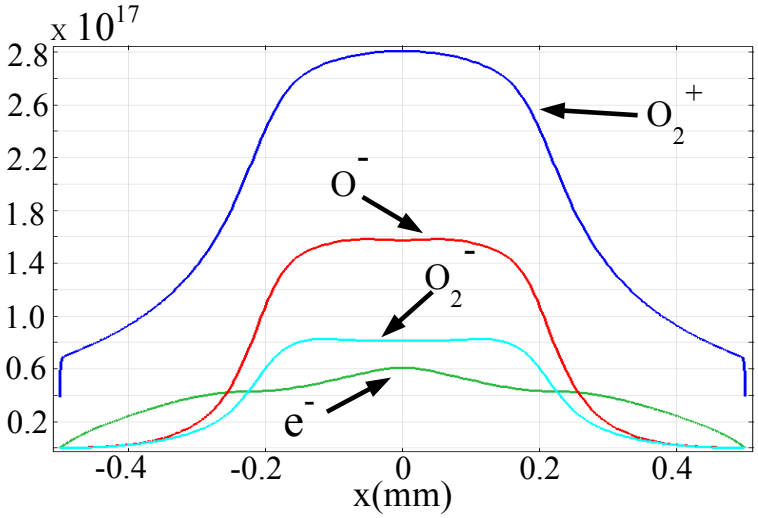

Figure 5.6: Phase averaged charged species density m^{-3} across the discharge domain (1-D cross section) for $V_{applied}$ = 325V, 0.6 % O_2 admixture

5.3.2 Gas mixing & heating

Gas mixture profiles for the device with and without a solid boundary below are discussed in section 5.3.2.1. Results of gas heating from the 1-D plasma model along with subsequent 2-D temperature profiles from a heating and mixing gas model is presented in section 5.3.2.2.

5.3.2.1 Gas mixing

The steady state air percentage for a helium jet (without admixture) is shown over a solid boundary (*BC* in figure 5.1) for a 15 mm device to surface separation in figure 5.7. The area below the gas outlet (radius of 1 mm) is filled predominately with helium and 1 % air. The air percentage increases to 10 % 20 mm from the centre. At lower separations ($\sim$ 3 mm) this area is filled exclusively with helium, the background impurity present in the helium carrier (10 ppm) and any ad-mixed O_2 ($\sim$ 1 %). As the gap between the device and the surface increases the surrounding air begins to mix with the carrier jet in this region.

The air fraction without a solid boundary is shown in figure 5.8. We see a significantly higher air fraction (10 - 20 %) near the device compared to a jet mixing over a solid boundary. The jet is found to mix sharply in the ambient with over 90 % air in the gas mixture found at 5 mm from the centre (x = 0). In section 5.3.3 below we contrast the density and spatial profiles of reactive species generated downstream of the device with and without a solid boundary.

5.3.2.2 Gas heating

In figure 5.9 the average percentage contribution to the total gas heating by the plasma from 1-D plasma model results are shown. The average (volume and phase) total power deposited here is

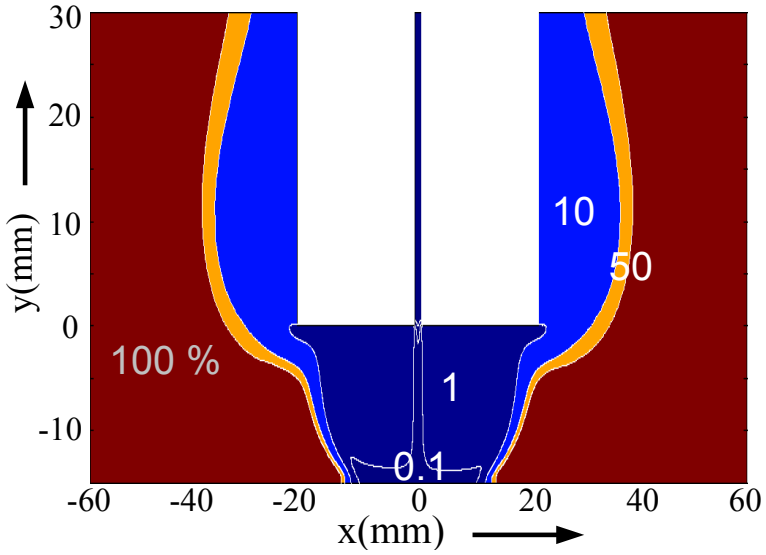

Figure 5.7: Percentage air (filled contour plot) in gas mixture for jet convecting over solid surface 15 mm from device

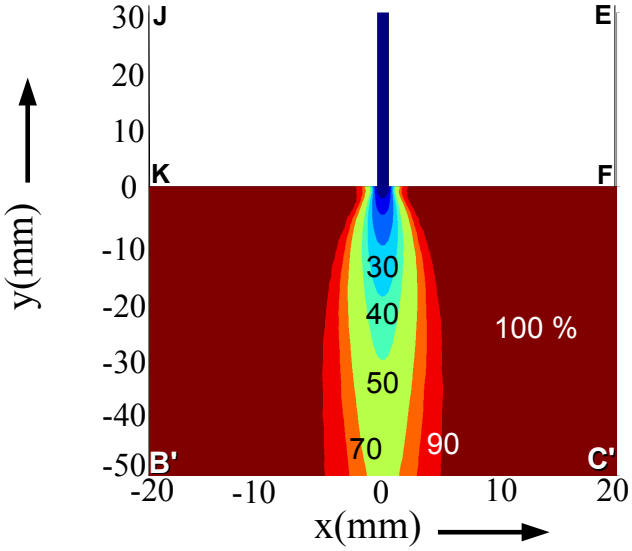

Figure 5.8: Percentage air (filled contour plot) in gas mixture for jet convecting into open air (without boundary). A reduced simulation domain is used here - see figure 5.1 for full domain.

1.49×10^7 W/m^3 (0.45 W). Elastic collisional heating (R_1 in table 5.1) accounts for on average 56.7 % of the heating here. Positive ion heating (O_2^+) by the electric field accounts for 34 % of the heating. Negative ion heating and inelastic heating due to heavy species collisions make up the remainder with contributions of 6.9 % and 2.4 % respectively.

A 2-D temperature profile is shown in figure 5.10 for steady state solutions of gas mixing

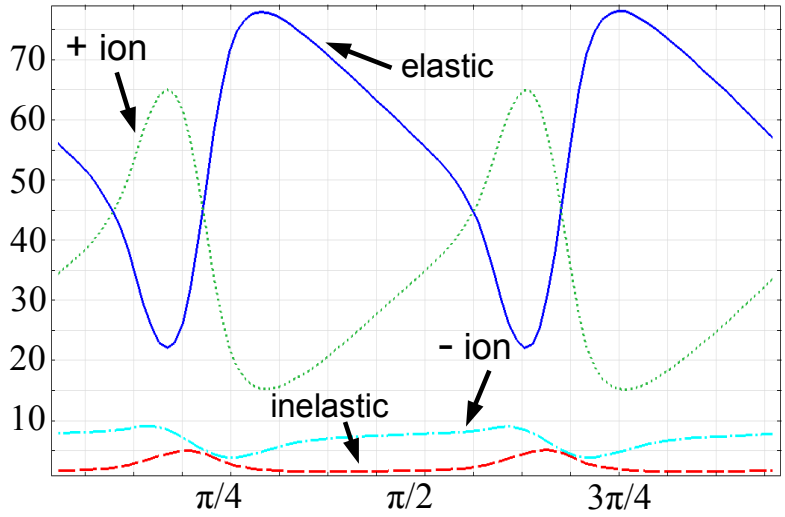

Figure 5.9: Gas heating contributions (average % of total) $V_{applied}$ = 325 V and 0.6% O_2 admixture.

and heating model. A maximum temperature of 315 °K is found in the domain with values ranging from 293 - 315 °K. Figure 5.11 (top) shows the surface temperature on a heat insulated treatment surface (x = 0) for up to 1000 seconds after the device has been started. A steady state temperature is reached after 800 - 1000 seconds here with a maximum temperature of 314 °K . Figure 5.11 (bottom) shows the spatial behaviour at a treatment surface for a range of device to surface separations. For small separations ($\sim$ 3 mm) a temperature of 40 - 41 °C encompasses a radius of approximately 50 mm on the surface. At larger separations (10, 15 mm) the area impacted by higher temperatures decreases to a radius below 30 mm.

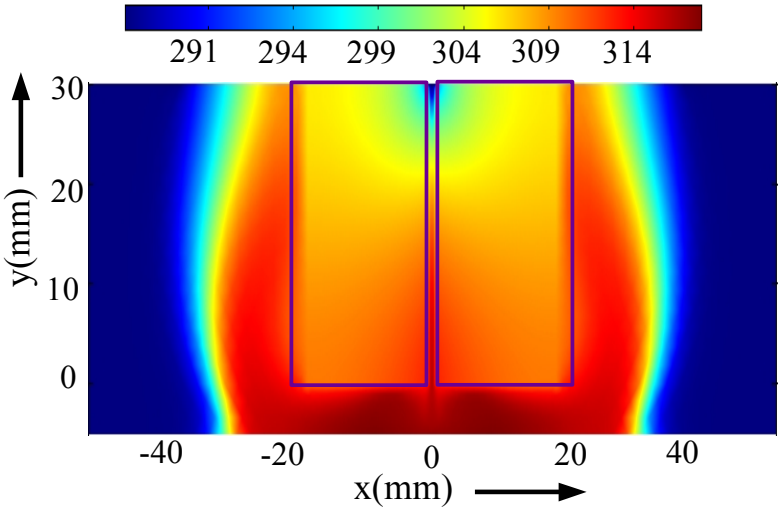

Figure 5.10: 2-D steady state temperature profile (K) for 5 mm device to surface separation. $V_{applied}$ = 325 V, 0.6% O_2, 1.4 slpm.

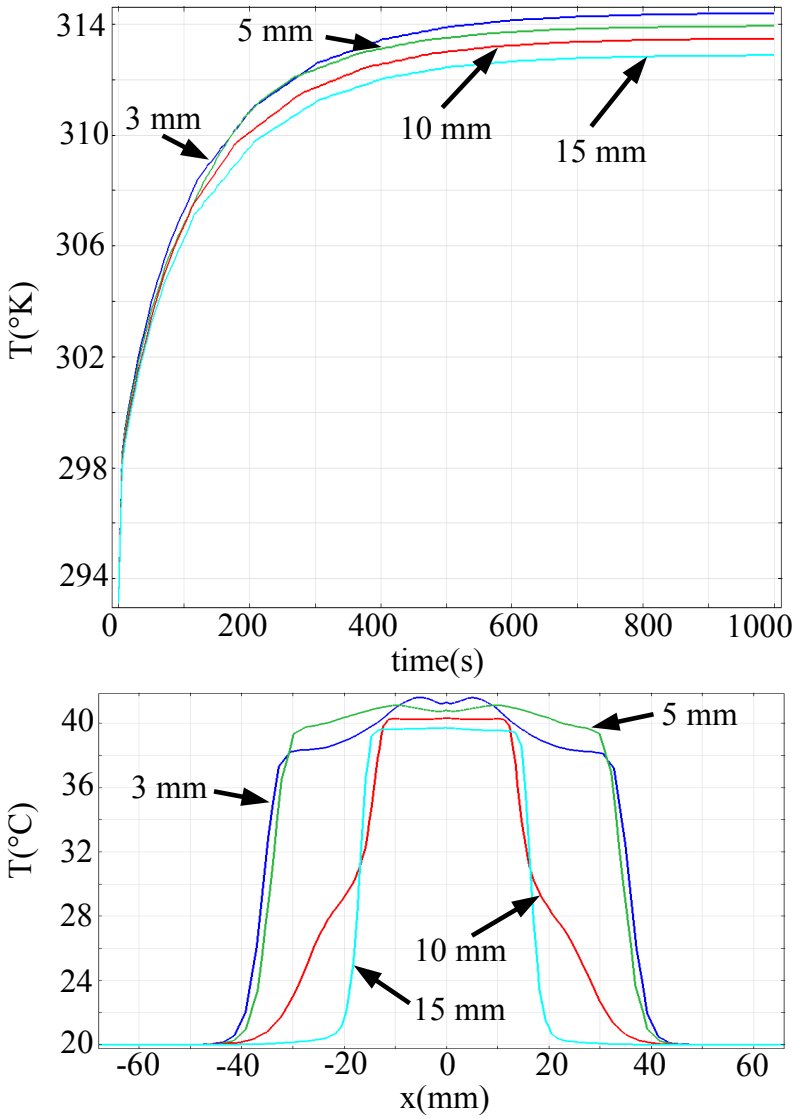

Figure 5.11: Top: surface temperature (K) at various times after start of discahrge for 10 mm device to surface separation. Bottom: surface temperature (C) at treatment surface for a range of device to surface separations. $V_{applied}$ *= 325 V, 0.6% O_2, 1.4 slpm.*

5.3.3 Reactive species

The steady state density of O and O_3 for solutions of our 2-D reacting gas model over an *inactive* solid surface is shown in figure 5.12 for a 5 mm device to surface separation with O_2 admixture of 0.6 % and applied voltage of $V_{applied}$ = 325 V. Peak O density of 4.4 $\times$ 10^{21} m^{-3} is found where the carrier gas exits the device (x = 0). O_3 density peak of 6.9 $\times$ 10^{21} m^{-3} occur in the gap between the device and surface within a radius of 30 mm here (see figure 5.12 top). O_3 production is dominated by three body reactions involving O, O_2 and background gases. Peak (steady state) reaction rates of 4.8 $\times$ 10^{24}, 1.8 $\times$ 10^{21} and 3.4 $\times$ 10^{21} 1/m^3s were found for O_3

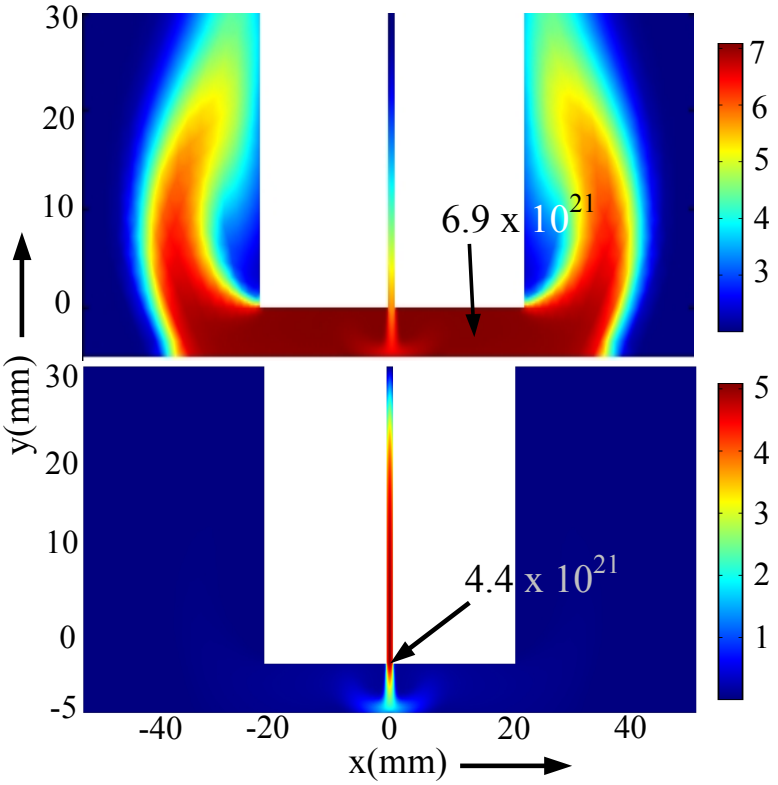

Figure 5.12: O_3 density ($1/m^3$) (top) and O density ($1/m^3$) (bottom) for 5 mm device to surface separation. $V_{applied}$ = 325 V and 0.6% O_2 admixture.

production reactions R_2, R_3 and R_4 (see table 4.2) respectively with spatial behaviour similar to atomic oxygen density profiles indicating strong conversion from O to O_3. The molecular oxygen in the jet and in the region directly below the device above a surface 5 mm below is mostly homogeneous ranging 0.6 % - 0.8 % of the total gas mixture. O_3 destruction (reactions $R_{5,8,11,13,14}$ in table 4.2) is dominated in the region between the plates by interaction with atomic oxygen (R_5) with peak values of 3.6×10^{21} $1/m^3s$. At the gas exit from the device the dominant O_3 destruction mechanism is due to interaction with O (^1D) (R_8) with peak values of 12×10^{23} $1/m^3s$. Outside the central region (radius $>$ 1 mm) and near the surface (x = 5 mm) O_3 destruction is dominated with O_2 ($a^1\Delta$) reaction (R_{11}) with peak values of 2.3×10^{23} $1/m^3s$.

The steady state density (ppm) of O, O_3 and O_2 ($a^1\Delta$) at a solid surface (*inactive*) for variation in device to surface separation is shown in figures 5.13 (a), 5.14 (a) and 5.15 (a) respectively. Atomic oxygen values (figure 5.13 (a)) show a decreasing trend for increasing separation as O is converted to O_3 as O_2 increases in the gas mixture (R_2 in table 4.2). O densities at the centre point $x = 0$ shown in figure 5.13 (a) of 105 ppm (2.6×10^{21} $1/m^3$) for a 2 mm separation, 49 ppm (1.2×10^{21} $1/m^3$) at 5 mm and 7.8 ppm (1.9×10^{20} $1/m^3$) at 15 mm separation are found. The spatial pattern of O at the surface encompasses a radius of maximum 10 mm with peak values increasing

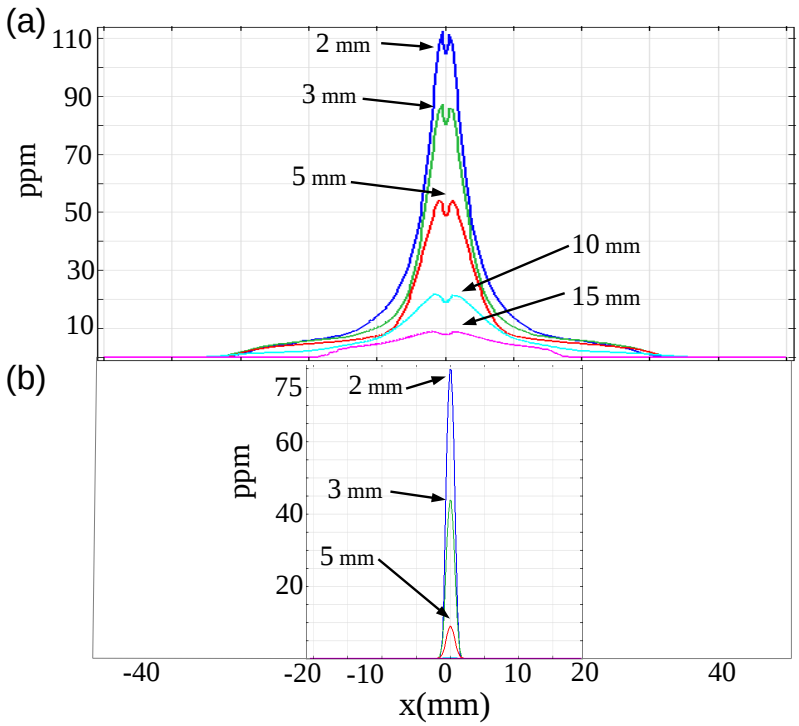

Figure 5.13: (a): O density (ppm) at inactive surface for a range of device to surface separations. (b): equivalent O density (ppm) for a jet convecting in open air (without surface)

in a narrow region for shorter separations. Ozone behaviour shown in figure 5.14 (a) displays a more diffuse spatial pattern with an increasing trend for 2 - 10 mm separations ($x = 0$). Figure 5.14 (a) shows peak values at $x = 0$ for 10 mm separation of 270 ppm (6.6×10^{21} 1/m^3) with the lowest value shown of 228 ppm (5.6×10^{21} 1/m^3) at 2 mm separation. At higher separations ozone production increases due to an increased molecular oxygen fraction available in the gap between the device and surface. Reaction R_2 (see table 4.2) dominates O_3 production here accounting for the decreasing trend in O density at higher admixtures. Peak ozone values at $x = 0$ were found at 10 mm separation before slightly decreasing at 15 mm separation. The spatial pattern of ozone on the surface at various separations is due to the mixing behaviour of the helium jet in air. Helium's density (which is approximately 10 times smaller than that of air) results in an upward mixing of the jet (see figure 5.1). The jets forward (y-axial) velocity ($-V_y$) is redirected in the x-direction as it encounters the solid surface. This results in larger x component of the velocity (V_x) at smaller separations due to the small volume of air between the device and surface. The combination of these upward and outward forces results in a wider O_3 peak on the surface for 2, 3 mm separations with peak O_3 values spanning a radius of 50 mm. This decreases to a peak O_3 radius of 40 mm for 5 mm separation and a 20 mm radius for 15 mm device to surface separation (see figure 5.14 (a)). O_2 ($a^1\Delta$) density (ppm) at a treatment surface shown in figure 5.15 (a) follows a similar spatial pattern to O_3. Peak values of 168 ppm occur at $x = 0$ for 2 mm device to surface separation

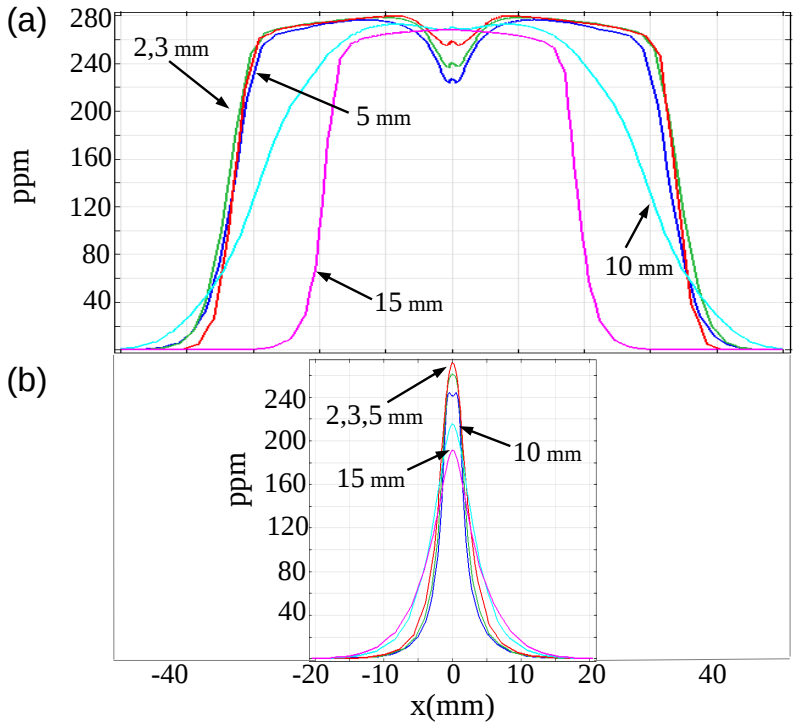

Figure 5.14: (a): O_3 density (ppm) at inactive surface for a range of device to surface separations. (b): equivalent O_3 density (ppm) for a jet convecting in open air (without surface)

within a radius of 50 mm. O_2 ($a^1\Delta$) density decreases to 155 ppm at 5 mm and 107 ppm at 15 mm separations as the peak radius decreases from 40 mm to 20 mm (see figure 5.15 (a)).

O, O_3 and O_2 ($a^1\Delta$) densities at equivalent separations in a jet mixing in open air without a solid boundary are shown in figures 5.13 (b), 5.14 (b) and 5.15 (b) respectively. A similar inlet flow of 1.4 slpm and applied voltage of 325 V (230 V_{RMS}) [62, 64] is used here. Atomic oxygen density decreases from 105 to 80 ppm 2 mm downstream with the omission of a boundary (figure 5.13 (b)). At 5 mm downstream O density rapidly drops from 49 ppm to 9 ppm with values of less than 0.5 ppm for higher separations (10, 15 mm). The increased O_2 density present in the gas mixture (see figure 5.8) at the jet exit for the open air case leads to conversion of the atomic oxygen density to O_3 via reaction R_2 in table 4.2 in a small spatial region around the jet exit. O peak density occurs within a radius of 2 mm of the jet centre compared with peaks within a 10 mm over a surface. O_3 values at $x = 0$ for the jet in open air range from 244 ppm to 218 ppm for distances of 2 - 15 mm downstream. Increased O_3 production (reaction R_2) at smaller distances downstream (< 5 mm) in the vicinity of the gas exit results in higher peak values at $x = 0$. Increased O_3 destruction via reactions R_4 for larger distances (10 and 15 mm) downstream leads to smaller O_3 values (245 and 218 ppm) when compared with the jet impacting a surface. O_3 peak density occurs within a radius of 5 - 10 mm of the centre compared to a jet impacting a surface peak values encompassing a 20 - 50 mm radius.

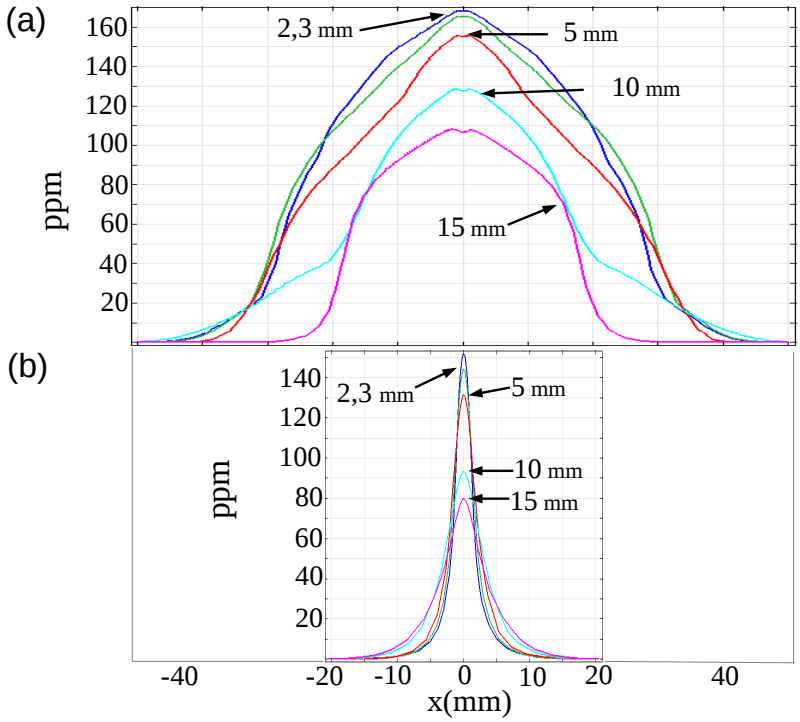

Figure 5.15: (a): O_2 ($a^1\Delta$) density (ppm) at inactive surface for a range of device to surface separations. (b): equivalent O_2 ($a^1\Delta$) density (ppm) for a jet convecting in open air (without surface)

Comparative results of reactive oxygen species density with and without a surface shown here highlight significant differences. The need for inclusion of a surface in accurate experimental characterisations and comparisons such as with *two-photon absorption laser-induced fluorescence* (TALIF) and *molecular beam mass spectrometry* (MBMS) studies is emphasised here.

5.3.4 Experimental comparison

Comparison of our model results with the *molecular beam mass spectrometry* (MBMS) study of Ellerweg et al. [64] is discussed in this section. Ellerweg et al. sampled atomic oxygen and ozone density from a μAPPJ for a range of device to surface (mass spectrometer sampling face) separations for an applied voltage of 325 V, oxygen admixture of 0.6 % and inlet flow of 1.4 slpm. Figure 5.16 shows atomic oxygen and ozone density for a range of device to surface separations at an inlet flow of 1.4 slpm for 0.6 % O_2 admixture and $V_{applied}$ = 325 V. Figure 5.16 also shows averaged atomic oxygen density at the surface for a range of separations. This average is taken over a radius of 20 mm from the centre.

At 2 mm separation an experimental O density of $\sim 7.5 \times 10^{20}$ 1/m^3 is reported by Ellerweg et al. [64]. Figure 5.16 shows a value at x = 0 of 2.6×10^{21} 1/m^3 and an average value of 1.2×10^{20} 1/m^3. The average numerical value at the surface matches experimental values more closely here with significantly higher value given by the model at x = 0. This is possibly due to

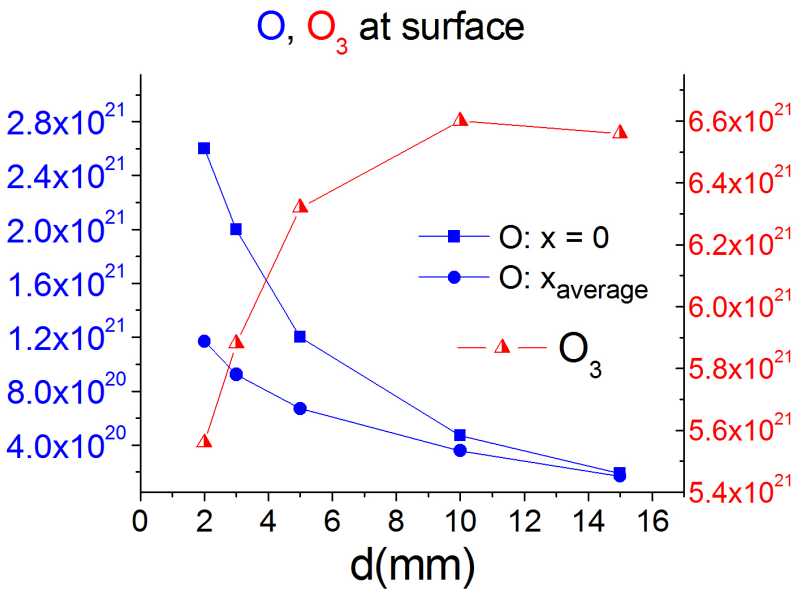

Figure 5.16: O and O_3 density (m^{-3}) at a (inactive)surface for a range of device to surface separations. O density is shown at $x = 0$ and also for an average over 20 mm radius at surface ($x_{average}$). O_3 value is at taken $x = 0$. $V_{applied}$ = 325 V and 0.6% O_2.

the difficulties involved in resolving the sharp peak (figure 5.13) in the atomic oxygen density on the surface at these small separations. At 3 mm the averaged numerical O density value of 9.2 $\times$ 10^{20} 1/m^3 shows better agreement with experimental measurement of $\sim$ 7 $\times$ 10^{20} 1/m^3 [64]. At 5 mm MBMS value of $\sim$ 6.2 $\times$ 10^{20} 1/m^3 [64] agrees well with the average (6.7 $\times$ 10^{20} 1/m^3) numerical value. For higher separations (10, 15 mm) average numerical values of 3.6, 1.7 $\times$ 10^{20} 1/m^3 and peak (x = 0) numerical values converge (see figure 5.16) as the peak surface distribution flattens. Comparison to experimental results of $\sim$ 3 $\times$ 10^{20} 1/m^3 and 1.2 $\times$ 10^{20} 1/m^3 show good agreement.

Ozone density numerical values (figure 5.16) are found to be significantly higher than reported in MBMS study of Ellerweg et al. [64]. Numerical values range from 5.6 $\times$ 10^{21} 1/m^3 at 2 mm to peak values of 6.6 $\times$ 10^{21} 1/m^3 for 10 mm separation. Comparative experimental values of $\sim$ 0.4 $\times$ 10^{21} 1/m^3 at 2 mm, 1.2 $\times$ 10^{21} 1/m^3 at 10 mm and 2.0 $\times$ 10^{21} 1/m^3 at 15 mm separation are significantly smaller. Experimentally, signal uncertainties in atmospheric mass spectrometry include species decay and reaction during transmission, mass dependent transmission issues, interference of the sampling aperture, choice of cross section and calibration species in calculation of absolute species density. Many of these factors such as the choice of cross section data [129] are known to contribute to significant variation in interpreted results [130, 131]. Numerically, failure to account for 3-D behaviour of the gas mixing, the limited reaction chemistry set used and the 1-D approximation of the plasma behaviour all possibly contribute to this observed deviation. In light of this atomic oxygen density values show relatively good qualitative and quantitative agree-

ment here given the many possible sources of error. However future studies are clearly needed to address the deviations discussed here providing further insight into the dynamics of these plasma sources.

5.3.5 Surface interaction

Surface interactions of plasma produced reactive species are highly dependent on the surface properties of the material. The μAPPJ is applied in both aqueous and dry environments adding to the complexity of interaction. In this section we discuss the interaction of the source with *reactive* solid and aqueous boundaries in the context of the results presented above. Section 5.3.5.1 discusses interaction with a dry reactive surface while section 5.3.5.2 considers the source impacting a liquid layer.

5.3.5.1 Solid surface interaction

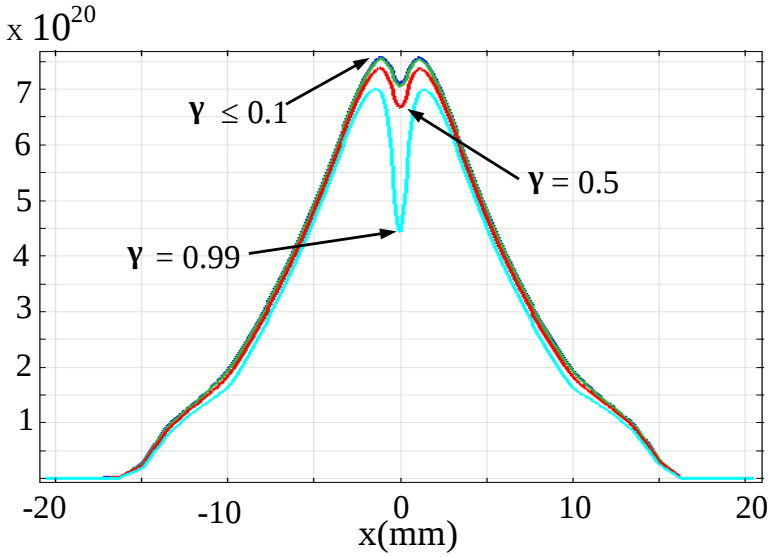

Figure 5.17: O density (1/m^3) at an active surface for a range of adsportion proabilities γ at 10 mm device to surface separation (0.6 % O_2 admixture, $V_{applied}$ = 325 V).

RONS flux loss at a treated surface is primarily dependent on the density of available reaction sites and the reaction rate for each species adsorption. The initiated radical formation on a treated surface is followed by a sequence of radical reactions (propagation) and eventual radical termination often producing a sequence of gaseous by-products which may interact with plasma RONS at the interface. A full model of this interaction for various surfaces is beyond the scope of this report. In this section we investigate surfaces losses at a reactive treatment surface by considering a simplified model of flux loss for a variety of adsorption probability values (γ) where ($1 > \gamma > 0$) for O, O_2 ($a^1\Delta$) and O_3 species [59]. Steady state results for the atomic oxygen

density at the treated surface for various reaction probabilities γ are shown in figure 5.17. For values of $\gamma > 0.1$ the species density on the surface (central region) begins to decrease (see figure 5.17). This indicates that for $\gamma : 0.1 \rightarrow 1$ surface reactions will be limited increasingly by the flux of reactive species available from plasma jet. Similar results are found for O_2 ($a^1\Delta$) and O_3 here. As reported by Yang et al. [59] surface loss rates of reactive species are increasingly independent of the reaction probability in this scenario ($\gamma > 0.1$) as the rate of surface reaction is limited by flux from the plasma and not by the surface adsorption probability. This indicates a regime were dosage may be calculated independent of explicit knowledge of the reaction probability. Reaction probabilities for atomic oxygen interacting with polypropylene surfaces [29] have been estimated as typically < 0.01 while reaction probabilities on biological polymers such as lipid layers of cell membranes are not yet fully understood. The inverted surface peaks shown in figure 5.17 reflect a larger flux of atomic oxygen impacting the central region.

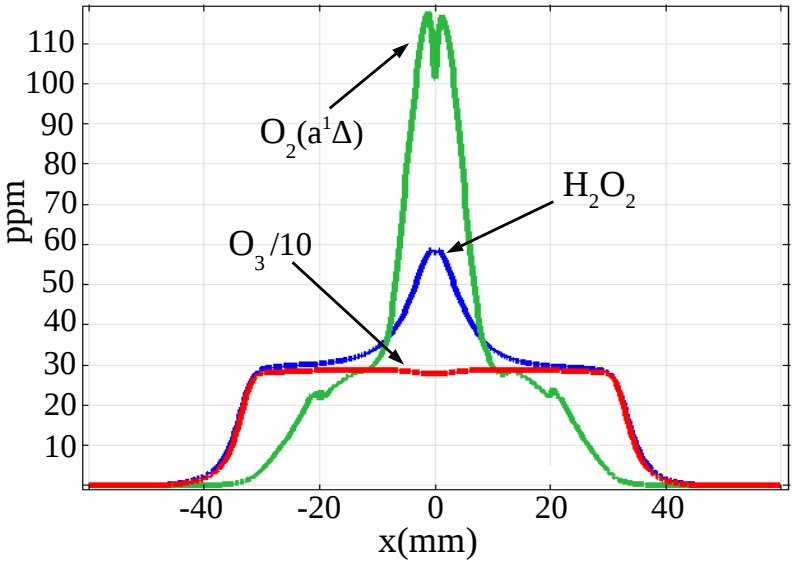

Figure 5.18: H_2O_2, O_2 ($a^1\Delta$) and O_3 (scaled by 10) density (ppm) at an aqeous surface for a 5 mm device to surface separation. $V_{applied}$ = 325 V and 0.6% O_2 admixture.

5.3.5.2 Aqueous surface interaction

The case of the μAPPJ impinging a treatment surface covered with a liquid layer is considered. Many biological application scenarios involve treatment surfaces such as living tissues covered in a thin liquid water layer. The plasma produced RONS are changed significantly by interaction with a H_2O liquid layer. The gas mixture at the liquid interface is saturated with water vapour which reacts with plasma produced RONS to form additional hydrogen radical species (see section 6.2).

Figure 5.18 shows the non-equilibrium (undissolved) gaseous species density at the water surface for steady state solutions of our 2-D reacting gas model. Atomic oxygen reacts strongly

with the H_2O vapour layer to form OH (R_1 in table 5.2) which further reacts with H_2O to form hydrogen peroxide H_2O_2 (R_{11} in table 5.2). Reaction of O_3 with the vapour layer results in further O formation which subsequently reacts to form H_2O_2.

Peak values of H_2O_2 of 58 ppm at $x = 0$ shown in figure 5.18 represent an almost complete conversion of the O density at this interface. Comparison of O_3 values on an inactive surface (figure 5.14) show an increase from 256 ppm to 288 ppm in O_3 density (reaction R_5 in table 5.2) over an aqueous surface due to the decrease in O_2 ($a^1\Delta$). O_2 ($a^1\Delta$) is quenched considerably to O_2 when it interacts with the H_2O vapour layer (R_4 in table 5.2). Peak values at $x = 0$ over a inactive solid surface fall from 155 ppm (see figure 5.15) to 101 ppm here. HO_2 values of 2.5 ppm are found at surface with peak values encompassing a radius of 40 mm. HNO_2 and HNO_3 values of < 0.1 ppm are found at the surface.

Species	K_H^{cc}	1/ (1+K_H^{cc})	1/ (1+1/K_H^{cc})
He	1.514e-5	0.99999	1e-5
O_2	5.32e-4	0.9995	5e-4
N_2	2.66e-5	0.99997	3e-5
O_3	4.91e-5	0.99995	5e-5
NO	7.77e-5	0.99992	8e-5
NO_2	1.68e-3	0.998	2e-3
N_2O	1.02e-3	0.999	1e-3
NO_3	7.37e-2	0.93	7e-2
N_2O_5	8.59e-2	0.92	0.08
H_2	3.19e-5	0.99997	3e-5
OH	1.19	0.457	0.543
HO_2	233	4e-3	0.996
H_2O_2	2905	3e-4	0.9997
HNO_2	2.01	0.33	0.67
HNO_3	8593	1e-4	0.9999

Table 5.3: Henry's law constant (solubility) in water at T=298.15K [14]

Equilibrium between the gas and liquid occurs as gaseous species dissolve into the water volume. Henry's law constants shown in table 5.3 represent the concentration ratio of dissolved and undissolved gases once equilibria is reached. The total available species ($n_{total} = n_{gas} + n_{aqueos}$) for dissolution is equal to the non-equilibrium distributions shown in figure 5.18. The fraction of dissolved and undissolved species in equilibria is given by the ratios 1/ (1+K_H^{cc}) and 1/ (1+1/K_H^{cc}) respectively shown in table 5.3. This shows that H_2O_2, HNO_2, HO_2 and HNO_3 species with solubility of 99.99 %, 67 %, 99.6 % and 99.99 % respectively (given by 1/ (1+1/K_H^{cc})) are the most important reactive species for treatment of aqueous layers in this context.

Diffusion coefficients for gaseous species in water are typically of the order 10^{-5} m^2/s [79].

Assuming a liquid layer thickness in the range of 10 - 1000 μm the time taken for a soluble gaseous species to saturate through the entire water layer will be of the order 1 - 100 s. This provides an estimate for the *treatment time* required for the μAPPJ to saturate such a water layer with H_2O_2 and other soluble species at this interface.

5.4 Conclusion

The effects of gas mixing, gas heating and surface interaction for a plasma jet with a planar geometry is discussed. Production efficiency studies for O production shows peak production in the range 0.2 - 1 % O_2 with electro-negativity values close to unity. This is similar to the 'spatial quenching' which shaped the plasma region for the plasma needle corona jet discussed in chapter 4. O, O_2 ($a^1\Delta$) and O_3 density profiles on a surface below the device were presented at a range of distances. Ambient O_2 is shown to play a key role in the oxygen-ozone balance in the effluent reaching a treatment surface. Atomic oxygen is found to convert to ozone with increasing device to surface separation as more molecular oxygen mixes from the ambient. Comparison at equivalent separations in a jet mixing in open air (without a solid boundary) showed species density to be significantly different in a jet impacting a surface. This highlights the difference between reactive species profiles expected in experimental diagnostics with and without a treatment surface. Comparison with experimental reports for atomic oxygen density values showed good agreement. Gas heating by the plasma is dominated by elastic and positive ion heating with significant contributions from electron impact dissociation of O_2 and negative ion heating. Steady state temperature profiles show maximum steady state temperatures of 315 K reached after approximately 500 seconds of device operation. Surface reactions on a reactive solid surface are demonstrated to be significantly diffusion limited for adsorption probabilities greater than 0.1. Interaction of the source with an aqueous surface showed hydrogen peroxide as the dominant species at this interface.

Chapter 6

Power modulation

Abstract

The effect of power modulation on reactive species generation and gas heating in a capacitively coupled radio frequency helium - oxygen ($\sim 0.6\%$) plasma jet is investigated by numerical modelling. Power is found to be coupled extensively to the electrons with large initial electron losses leading to weak interference between successive modulation phases. Surface densities of reactive oxygen species on a treatment surface below the device are found to typically range over an order of magnitude for variation in the duty cycle above the initial growth phase (~ 20 % in this case). Effects on gas heating show a larger range of temperature control when compared with convection cooling. Power modulation is demonstrated as an effective mechanism to both control reactive species and heat flux to a treatment surface with specific interest to applications in biomedicine and heat sensitive surface engineering.

6.1 Introduction

Control of plasma produced chemistry and heat flux is a key challenge for emerging applications of low temperature atmospheric pressure plasma technology in biomedicine and surface engineering. Power modulation is investigated as a mechanism for control of reactive species and heat flux delivery from a plasma jet to a treatment surface. *Implementation* of low temperature atmospheric pressure plasma technology for surface treatment depends on delivery of a *controlled dosage* of a desired plasma produced chemistry to a surface often sensitive to thermal shock. Dosage of reactive agents to living organisms may dictate the balance between therapeutic and toxic effects. This emphasises a clear need for investigation of control methodologies for delivery of key reactive

*Power modulation in an atmospheric pressure plasma jet, Plasma Sources Science and Technology, 23, 6, 065012, 2014 http://dx.doi.org/10.1088/0963-0252/23/6/065012

species. Limitation of heat flux is a critical constraint for the uptake of plasma technologies in medicine as brief exposure to temperatures above body temperature can lead to undesired cell death. Controlling both reactive species and heat flux delivery to treatment surfaces is discussed here in the context of power modulation of the applied voltage. The study of the continuously powered source in chapter 5 reveals a complex and limited operational range for variation in reactive species production and heat flux. This behaviour due to the electro-negative character of the discharge leads to a non-linear power behaviour with voltage variation. Modulation of the applied power offers a possible alternative mechanism for control of reactive species and heat flux to treatment surfaces which warrants further investigation.

Power modulation effects on plasma growth and decay, reactive species generation and gas heating is discovered. A *capacitively coupled plasma* (CCP) helium jet admixed with oxygen ($\sim$ 0.6 %) driven by a *radio frequency* (rf) voltage (13.56 Mhz) and modulated by a 100 kHz frequency is studied here. The *micro-Atmospheric Pressure Plasma Jet* (μAPPJ) [7] device has emerged as a benchmark source for numerical [55, 56, 57, 58, 59, 60, 61] and experimental investigation [60, 62, 63, 64] of radio frequency plasma jets for development of applications in biomedicine and heat sensitive surface engineering. The μAPPJ consists of two parallel steel electrodes of 1 mm thickness and 30 mm in length surrounded on two sides by 1 mm thick transparent quartz allowing optical diagnosis of the plasma core. Small admixtures of atmospheric gases such as O_2 can be added to a helium carrier gas to generate *reactive oxygen nitrogen species* (RONS). Reports on experimental [132, 133] and numerical studies [93, 94] of radio frequency CCP jets have discussed the effect of power modulation on electro-positive gas mixtures in helium. This chapter presents numerical evidence for behaviour in an electro-negative gas mixture of helium and oxygen. The effects of duty cycle variation on reactive oxygen species generation and gas heating is investigated in this context.

6.2 Model description

The commercial finite element partial differential equation solver COMSOL Multi-physics (version 4.3a) [65] is used in this work. A sinusoidal applied voltage $V_{applied}sin(2\pi ft)$ with an rf frequency of $f = 13.56$ MHz is considered where $V_{applied}$ is the applied voltage amplitude. A frequency of 100 kHz is used over a range of duty cycles to modulate the applied power. Solutions of continuity equations for the electron density, electron energy and heavy species densities are coupled with solutions of Poisson's equation for the electric field over a 1-D cross section across the electrode gap ($HILG$ in figure 6.1). Reactive neutral species production and gas heating rates are extrapolated from solutions of the 1-D plasma model across the 2-D electrode domain for use as source terms in a 2-D model of a reacting, mixing and heating gas of uncharged species convecting through the electrodes on to a substrate below the device. Decoupling of plasma dynamics from the gas and heat dynamics in this manner allows tractable solutions for the study of uncharged

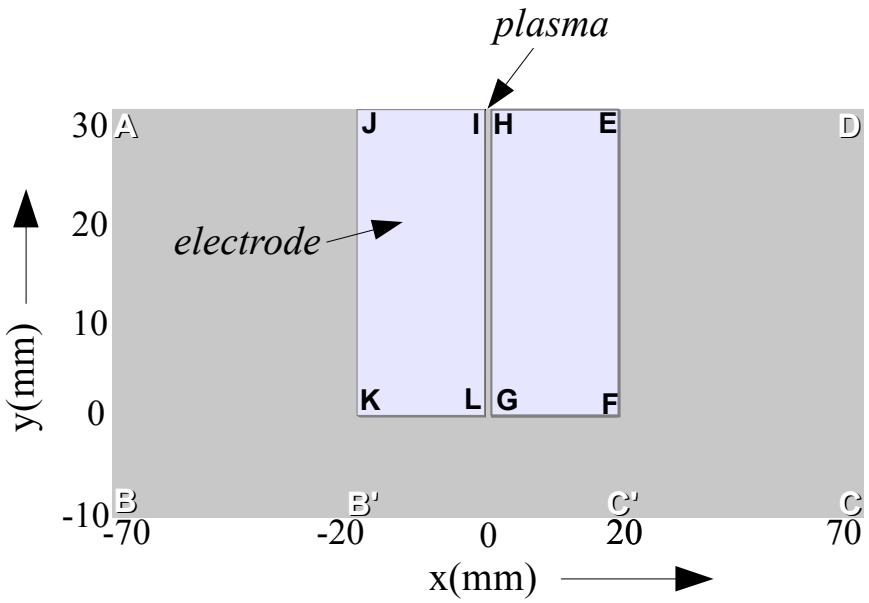

Figure 6.1: Model geometry

reactive oxygen nitrogen species (RONS) and gas heating over longer time-scales. Such a decoupling relies on the assumption that the charged and neutral species produced by the plasma are weakly interacting. The plasma density ($\sim 10^{17}$ m^{-3}) in this context is typically several orders of magnitude lower than the steady state densities of O, O_2 ($a^1\Delta$) and O_3 ($\sim 10^{21}$ m^{-3}) [56, 59, 90]. Uncharged plasma produced species density are therefore not significantly effected by losses due to interaction with charged species. Charged and exited species densities in the plasma may however be changed remarkably by the influence of plasma produced reactive oxygen species. Niemi et al. [60] showed that the helium meta-stables are predominately quenched by penning ionisation with O_2 over O_2 ($a^1\Delta$), O_3 and O interaction. Charge transfer effects due to O_2 ($a^1\Delta$), O_3 and O interaction can change the composition of negative charge carriers depending on the O_2 admixture [90] but are assumed here not to lead to large inaccuracies in the *overall electrical behaviour* of the plasma given the similar reaction pathways and transport properties of these negative charge carriers [90, 91]. Electron attachment for negative charge carriers with atomic oxygen is however included here (see below) due to its importance in the decaying plasma.

Gas dynamics are studied by solution of mass and momentum continuity equations (compressible Navier-Stokes). A mass transport convection-diffusion formulation is coupled to the Navier stokes equations to study the transport and interaction of plasma produced reactive neutral (uncharged) species. A thermal energy equation in the gas and solid phase is solved for the temperature of the gas mixture and electrodes. Thermal conductivity, material density and specific heat capacity values at constant pressure for steel electrodes is taken as 44.5 $W/(mK)$, 7850 kg/m^3 and 475 $J/(kgK)$ respectively here. Temperature dependent values for thermal conductivity and

specific heat capacity for the gas mixture are used [125]. Further details of equation formulation, boundary conditions and transport properties can be found in chapter 2 and reports [13, 126].

Ref	Reaction	Rate
R_1 [72]	e+He→He+e	*BOLSIG+*
R_2 [72]	e+He→He*+e	*BOLSIG+*
R_3 [72]	e+He→2e + He$^+$	*BOLSIG+*
R_4 [100]	e+He* →e+He	2.9×10^{-15}
R_5 [124]	e+He_2^+ →He*+He	$5.3 \times 10^{-15}/T_e^{0.5}$
R_6 [44]	He$^+$+2He→He+He_2^+	1.1×10^{-43}
R_7 [44]	He*+2He→He+He_2^*	2×10^{-46}
R_8 [44]	He*+He* →e+He_2^+	1.5×10^{-15}
R_9 [44]	He_2^* → 2He	10^4
R_{10} [44]	He_2^*+He_2^* →e+He_2^++2He	1.5×10^{-15}
R_{11} [72]	e+O_2 →2e + O_2^+	*BOLSIG+*
R_{12} [72]	e+O_2 →e+2O	*BOLSIG+*
R_{13} [72]	e+O_2 →e+O+O (^{1}D)	*BOLSIG+*
R_{14} [101]	e+O_2^+ →2O	$6 \times 10^{-11} T_e^{-1}$
R_{15} [102]	He*+O_2 →He+O_2^++e	$2.54 \times 10^{-16}(T_g/300)^{0.5}$
R_{16} [103]	He_2^*+O_2 →2He+O_2^++e	$1 \times 10^{-16}(T_g/300)^{0.5}$
R_{17} [72]	e+O_2 → O+O^-	*BOLSIG+*
R_{18} [91]	e+ He + O_2 → O_2^- + He	$3.6 \times 10^{-43} T_e[eV]^{-0.5}$
R_{19} [101]	O^- + O_2^+ → O + O_2	$3.464 \times 10^{-12} T_g^{-0.5}$
R_{20} [101]	O_2^- + O_2^+ → O + O_2	$3.464 \times 10^{-12} T_g^{-0.5}$
R_{21} [101]	O^- + O_2^+ + He → O + O_2 + He	$3.12 \times 10^{-31} T_g^{-2.5}$
R_{22} [101]	O_2^- + O_2^+ + He→ 2O_2 + He	$3.12 \times 10^{-31} T_g^{-2.5}$
R_{23} [91]	O^- + O_2 → O_2^- + O	1.5×10^{-18}
R_{24} [102]	O^- + O → O_2 + e	$5 \times 10^{-16} T_g^{0.5}$
R_{25} [102]	O_2^- + O → O_3 + e	$1.5 \times 10^{-16} T_g^{0.5}$
R_{26} [72]	e + O_2 → e + O_2 ($a^1\Delta$)	*BOLSIG+*

Table 6.1: He - O_2 plasma chemistry

Notes: (1) R_i (n) - n indicates reference for i^{th} reaction (2) Rates in units $[m^3/s]$, $[m^6/s]$ (3 body reactions), T_g (K) gas temperature, T_e (K) electron temperature except where stated otherwise (3) M represents background gases He, N_2, O_2.

The plasma chemistry consists of six ionic species (He^+,He_2^+, N_2^+, O_2^+, O^- and O_2^- with thirteen neutral species (He, He*, He_2^*, O_2, O_2 ($a^1\Delta$), O, O (^1D), N_2, N_2 ($A^3\Sigma$), N_2 ($B^3\Pi$),

N, N (^{2}D)). A helium purity of 99.999 % is assumed here (10^{-5} air fraction) with the impurity considered to be made up of 20 % O_2 and 80 % N_2. The helium-oxygen plasma chemistry is shown in table 6.1. Electron detachment reactions R_{24} and R_{25} included in table 6.1 are dependent on the atomic oxygen density. Steady state atomic oxygen density develops on much larger timescales ($\sim$ 0.1 s) compared with the smaller ($\sim \mu$s) timescale of charged species behaviour. In order to approximate the atomic oxygen density a fixed value based on O_2 depletion rates of 0.3% for conversion of O_2 to O is used here. This depletion rate is consistent with measured [64] atomic oxygen density ($\sim 10^{21}$ m^{-3}) values for the μAPPJ source. Air impurities in the helium carrier gas are assumed to be made up of 79% N_2, 20 % O_2 and 1% H_2O. Further details of the helium - nitrogen plasma chemistry and the uncharged species chemistry employed here can be found in chapter 4.

Average variation in power, heating and species density with pulse modulation is investigated by solving an additional time dependent variable given by the following.

$$K_{avg}(t > \tau) = \frac{1}{\tau}\int_{t-\tau}^{t}\left(\frac{1}{d}\int_{0}^{x=d} K(x,t)\ \mathrm{d}x\right)\mathrm{d}t \tag{6.1}$$

The applied voltage period is given by τ (s) here. The length d (m) represents the electrode separation. K_{avg} (t) represents a continuous time average over the interval [$t-\tau$,t] for the average over the discharge region ([0,d]) of the model variable K (x,t).

6.3 Results & Discussion

Results of the 1-D and 2-D numerical models for a μAPPJ helium/oxygen (0.6 %) plasma jet powered with voltage amplitude of 325 V, a frequency of 13.56 Mhz and modulated by a frequency of 100 kHz is discussed here. The duty cycle of the power pulse width lasting 10 μs is varied to investigate the interaction of successive pulses focusing on the effects of gas heating and reactive species generation. Plasma power and species density behaviour is discussed in section 6.3.1. Gas heating by the plasma and the resulting gas temperatures impacting a treatment surface is discussed in section 6.3.2. Production rates of reactive species due to power modulation and resultant species density at the treatment surface are discussed in section 6.3.3.

6.3.1 Power modulated plasma behaviour

The average power (P_{avg} (t)) deposited to the plasma is shown in figure 6.2 for a range of duty cycles. An initial period of exponential growth is bounded by asymptotic convergence to a steady state power (Δ $P_{avg} < 5$ %) beyond a 30 % duty cycle. Changes in duty cycles between 20 - 90 % shown in figure 6.2 do not effect substantially the length of this power growth phase. This demonstrates the weak interference between neighbouring power pulses for duty cycles up to 90%

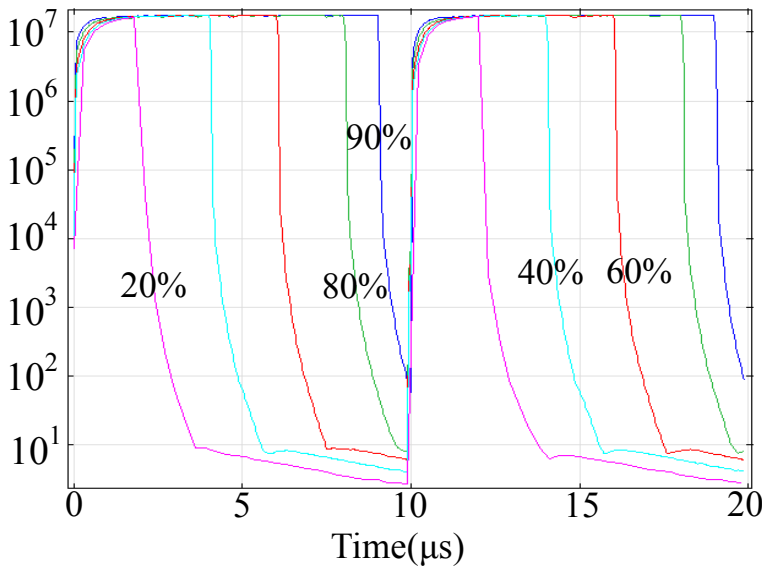

Figure 6.2: Power P_{avg} (t) W m^{-3} (continuous phase and volume averaged) for a range of duty cycles over a 100 kHz modulation period

observed. In the following discussion we will see how this behaviour is linked to the large electron decay in the first 0.5 μs during the power off phase.

The majority of the power is found to be coupled to electrons here with average values of 86.3 % of the steady state power of 1.71 W m^{-3}. The remaining contribution is dominated by power coupling to negative ions accounting for 13.4 %. Figure 6.2 shows that increasing the duty cycle above 20 - 30 % increases the period of power sustained at the steady state power. The average (over modulation period) plasma power varies here from 14.1 % of the continuous power at a 20 % duty cycle to 88.7 % at a 90 % duty cycle.

The electron, total positive and negative ion density is shown in figure 6.3 for a 60 % duty cycle (6 μs power-on, 4 μs power-off). The electron density increases initially from a background value of $\sim 3 \times 10^{15}$ m^{-3} of residual electrons from the previous power cycle. Steady state densities are reached after 20 - 30% of the modulation cycle (2 - 3 μs) corresponding to 27 - 41 cycles of the applied voltage (13.56 Mhz). The average electro-negativity is 1.6 in the power-on phase (0 - 6 μs). O^- and O_2^- negative ion species have an average density of $\sim 3.7 \times 10^{16}$ m^{-3} and $\sim 2.2 \times 10^{16}$ m^{-3} respectively. O_2^+ is the dominant positive ion with average density of 1.4×10^{17} m^{-3}. Mean electron energy values of 0.26 eV occurring at 2 μs increase to 4.03 eV at 6 μs. Average values for the power-on (0 - 6 μs) phase were 3.8 eV here. During the power-off phase average energy values drop to 0.08 eV at the end of the modulation period (10 μs).

Figure 6.4 shows the electron density behaviour for a range of duty cycles. Electron density growth which determines the degree to which consecutive modulation periods interfere shows similar behaviour to power growth shown in figure 6.2. Increase in duty cycle from 20 % to 90 % results in an increase of the initial average electron density from 1.9×10^{15} m^{-3} to 8.3 $\times$

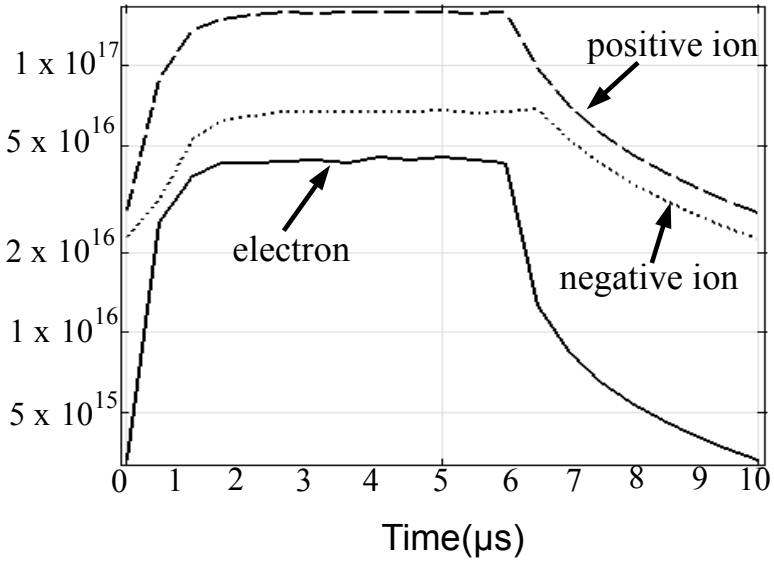

Figure 6.3: Average (continuous phase and volume averaged) charged species density (1/m^3) behaviour over a modulation period for a 60% duty cycle.

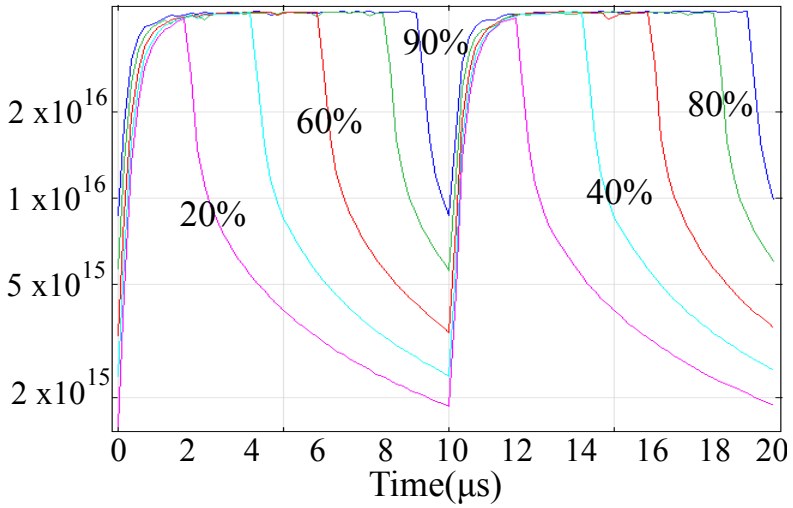

Figure 6.4: Electron density (continuous phase and volume averaged) 1/m^3 for a range of duty cycles over two modulation periods: $V_{applied}$ = 325 V, O_2 admixture = 0.6%, modulation frequency 100 kHz.

10^{15} m^{-3}. This initial residual electron density corresponds to 4.1 % and 18.7 % respectively of the average electron density of 4.5 $\times$ 10^{16} m^{-3} in a continuously powered plasma. Clearly large electron loss occurs in power-off phase for the first 10 % (1 μs) of the duty cycle.

The balance of diffusive, migrative and collisional forces determines the rate of charged

species decay. The rate of electron loss is given by

$$\frac{\partial n_e}{\partial t} = Q_e - \nabla \cdot \Gamma_e \tag{6.2}$$

$$\Gamma_e = \mu_i n_e E - D_e \nabla n_e \tag{6.3}$$

Electron number density n_e, flux Γ_e, production/loss term Q_e . Migrative and diffusional losses of electron density are given by $\nabla . \Gamma_e$ m^{-3} s^{-1}. Collisional losses due to electron attachment (R_{17} in table 6.1) and ion-electron recombination (R_{14}) reactions and gains by detachment ($R_{24,25}$) reactions is given by Q_e m^{-3} s^{-1}. Migrative and diffusional losses of charged species in the absence of an external electric field is constrained by charge neutrality. Electron mobility is typically $\sim$ 100 times that of ionic mobilities [4] due to their mass differential. This mobility differential leads to the emergence of an electric field known as the *ambi-polar electric field* which accelerates ion free diffusion and retards electron free diffusion. If we consider positive and negative ion mobilities are approximately equal ($\mu_p \approx \mu_n \approx \mu_i$ and $D_p \approx D_n \approx D_i \approx \mu_i$ T_i) an effective migrative and diffusional electron loss term $\hat{D}_e$ $m^2 s^{-1}$ is given by the following [134].

$$\frac{\partial n_e}{\partial t} + \nabla \cdot (\hat{D}_e \nabla n_e) = Q_e \tag{6.4}$$

$$\hat{D}_e = \frac{\mu_i T_e (n_p + n_n)}{n_e + \mu_i/\mu_e (n_p + n_n)} + \mu_i T_i \tag{6.5}$$

Here n_e, n_p and n_n are the electron, positive and negative ion density. When the electro-negativity (n_n/n_e) is small $n_e \mu_e \gg \mu_i (n_p + n_n)$ with $\hat{D}_e^+ \approx \mu_i (T_e + T_i)$. For high electro-negativity $n_e \mu_e \ll \mu_i (n_p + n_n)$, $\hat{D}_e^- \approx \mu_e T_e$. For $T_e \gg T_i$ the ratio $D_e^-/D_e^+ \approx \mu_e/\mu_i \approx 100$ [134]. Electron diffusion in electronegative portions of the plasma where $T_e \gg T_i$ have therefore significantly higher rates than in electron-positive portions.

Components of electron loss due to collisional and migrative-diffusive forces are shown in figure 6.5 (b) in the power-off phase. Migrative-diffusive losses dominate initially with peak values of 4.1×10^{23} $m^{-3}s^{-1}$ occurring at 6.02 μs. After 1 μs collisional and migrative-diffusive losses become comparable. This trend continues throughout the rest of the decay period with electro-negativity tending towards a steady state. Figure 6.5 (b) shows the total electron loss rate (right axis) $m^{-3}s^{-1}$ in the power-off period (6 - 10 μs) for a 60% duty cycle. Electron loss rates show a peak value of 4.3×10^{23} $m^{-3}s^{-1}$ occurring at 6.05 μs. Electron losses in the first 0.1 μs, 0.5 μs and 1 μs of the 4 μs power-off phase account for 15.1 %, 71.1 % and 80.9 % respectively of the overall electron loss. The majority of electrons are lost here in the first 0.5 μs. This initial decay period sets a limit for interference between power pulses which significantly shortens the initial growth period in electron density. Figure 6.5 (b) shows the average electro-negativity in the power-off period (6 - 10 μs). The first $\sim$ 1 μs of the plasma decay phase (6 - 7 μs) results in a large increase in electro-negativity with an average (volume) values increasing from 1.6 to 6.3 between 6 and 7 μs. This is due to electron attachment reaction R_{17} in table 6.1.

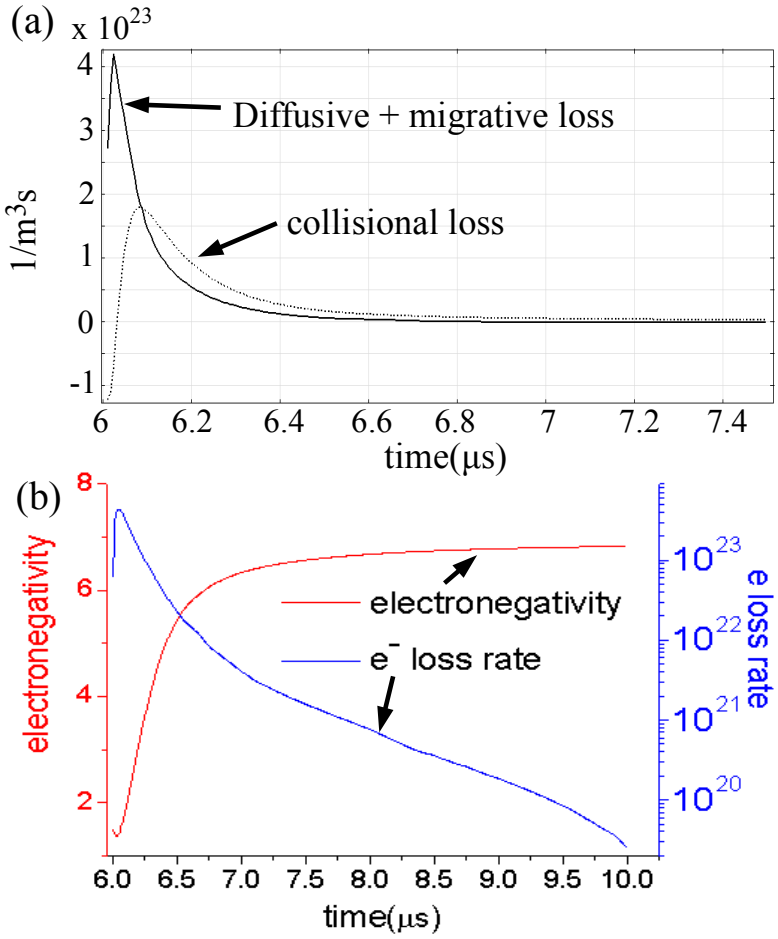

Figure 6.5: (a) Collisional and diffusive-migrative average electron loss rate $m^{-3}s^{-1}$ in the power-off period (6 - 10 μs) for a 60% duty cycle (b) average electro-negativity (left axis) and electron loss rate (right axis) $m^{-3}s^{-1}$ in the power-off period (6 - 10 μs) for a 60% duty cycle

Figure 6.6 shows the spatial distribution of charged species across the discharge gap at the start of the power-off period (6 μs) (figure 6.6 (a)). The electric field across the domain is shown in figure 6.7. At t = 6 μs a sheath in the left hand domain results in electron movement from the right hand side to preserve quasi-neutrality. Figure 6.8 shows the effective electron diffusion coefficient $\hat{D}_e$ (equation 6.4) across the discharge gap. At t = 6 μs peak effective diffusion coefficients occur near x = -0.5 mm with values of $\sim$ 0.36 m^2s^{-1}. The large initial electro-negativity in the left hand side of the domain in the first 0.05 μs results in large electron loss (D_e^- equation 6.4) from the left hand side of the domain. After 0.2 μs we see in figure 6.6 (b) that the electron density is concentrated in the centre of the discharge gap along with the other charged species. The plasma density is enclosed between sheath regions of $\sim$ 0.2 mm width here. Figure 6.7 at t = 6.5 μs shows an electric field which is equal and opposite in the sheath region characteristic of ambipolar diffusion.

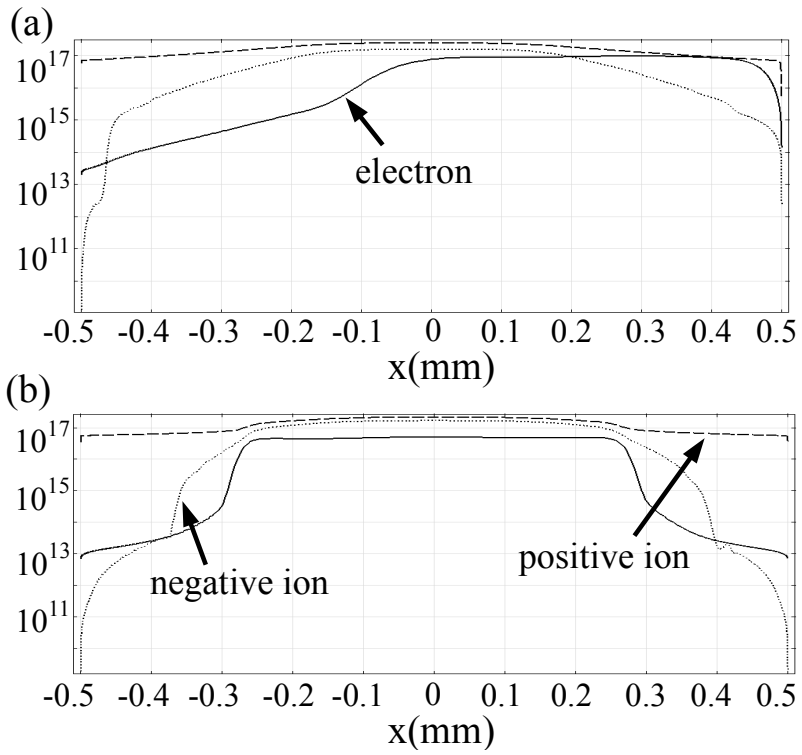

Figure 6.6: Charged species density m^{-3} across discharge domain at (a) t = 6μs and (b) t = 6.2μs for a 60% duty cycle

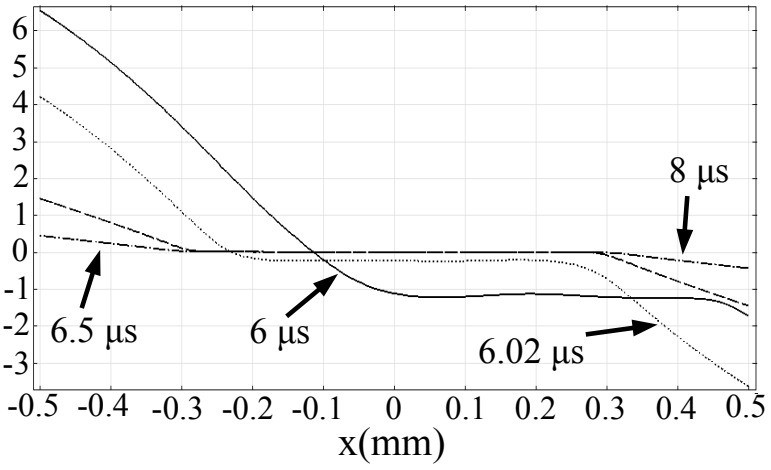

Figure 6.7: Electric field E (kV/cm) across discharge gap at various times in power-off phase for 60% duty cycle

6.3.2 Power modulated gas heating

The contribution from various plasma heating mechanisms to gas heating is shown in figure 6.9 for a duty cycle of 60 %. The average (volume and phase) steady state gas heating by the plasma

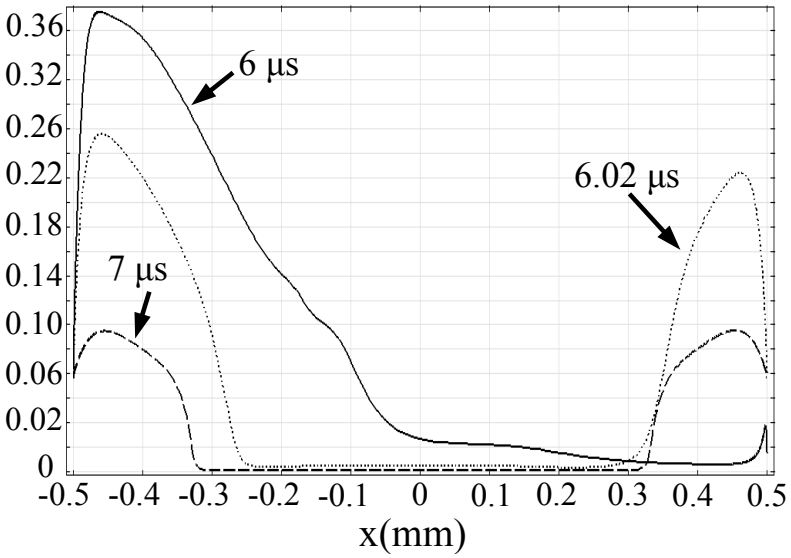

Figure 6.8: $\hat{D}_e$ (m^2/s) across discharge gap at various times in power-off phase for 60% duty cycle

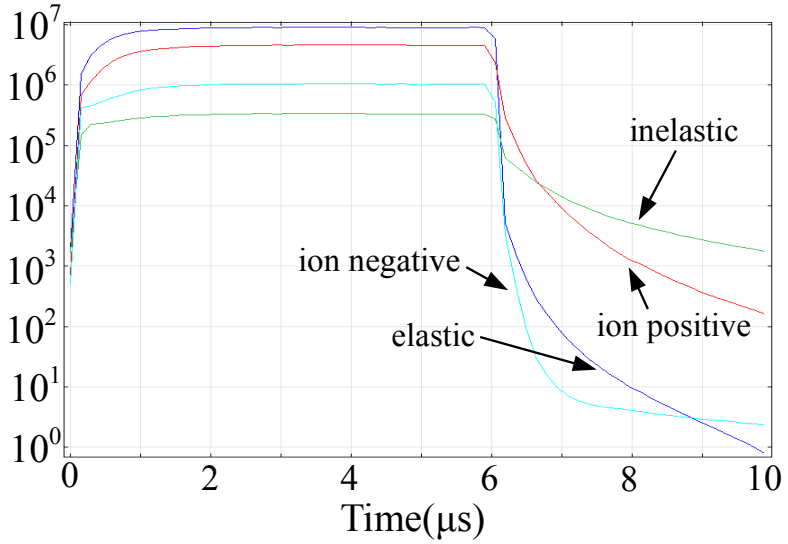

Figure 6.9: Gas heating contributions ($W\ m^{-3}$) over a modulation period: $V_{applied}$ = 325 V, O_2 admixture = 0.6%, modulation frequency 100 kHz, 60% duty cycle

is 1.49×10^7 W/m^3 (0.45 W) during the power pulse. In the steady state power phase (> 3 μs) elastic collisional heating dominates for on average 56.7 % of the heating. Positive ion heating (O_2^+) accounts for 34 % of the heating. Negative ion heating and inelastic heating due to heavy species collisions make up the remainder with contributions of 6.9 % and 2.4 % respectively. In the power off period (> 6 μs in figure 6.9) gas heating is dominated by inelastic heating due to heavy species collisions (ion recombination reactions in table 6.1) with values several orders of

magnitude lower than steady state contributions. Figure 6.10 shows results for the continuous phase and volume averaged total gas heating (Q_{avg} (t): see section 6.2) over a modulation cycle for a range of duty cycles. The gas heating behaves similarly to the power growth shown in figure 6.2.

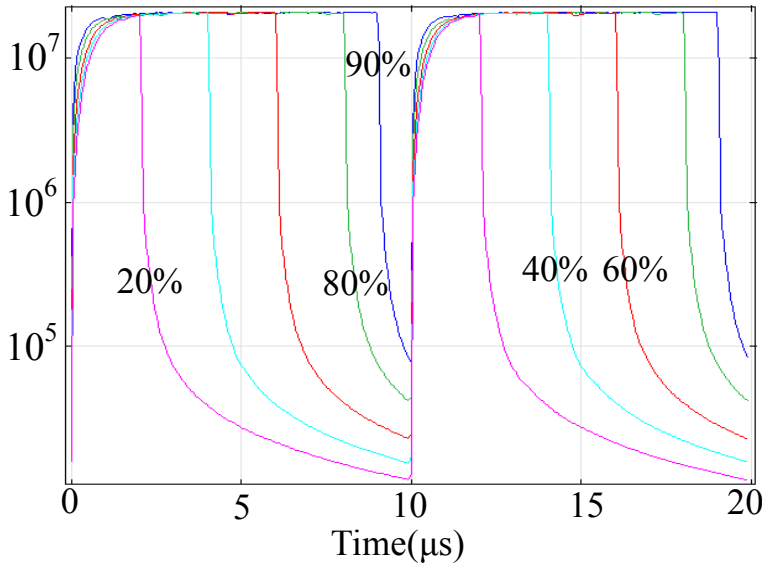

Figure 6.10: Total gas heating Q_{avg} (t) (W m^{-3}) over a modulation period for a range of duty cycles: $V_{applied}$ = 325 V, O_2 admixture = 0.6%, modulation frequency 100 kHz

Solutions of a 2-D gas mixing and heating model (see section 6.2) are given in figure 6.11 which shows the steady state surface temperature on a heat insulated treatment surface (BC in figure 6.1) 10 mm below the device for a range of duty cycles. Peak surface temperatures are contained here within a radius of 25 mm from the centre. The gas temperature at the surface is reduced from a peak value of 44 °C at 100 % duty cycle to 23 °C at 20% duty cycle. At 5 mm device to surface separation a similar range of steady state surface temperatures of 23 °C to 44 °C at 20 % and 100 % respectively are found. At a 15 mm separation a range of 22.9 °C to 43.2 °C is found. Increasing the device to surface separation in this range results in quiet a small decrease in peak gas temperatures at the treatment surface.

The effects of convective cooling on the gas temperature on a treatment surface (BC in figure 6.1) is shown figure 6.12. Steady state surface temperatures for volumetric flow rates of 1 - 2.5 slpm are shown here. Peak surface temperatures (x = 0) in the range of 44.6 °C - 35.8 °C are found for increasing gas flow. The spatial behaviour of the surface temperatures shown in figure 6.12 shows larger volumes of heated gas impacting an increasing surface area at higher flows at lower temperatures. At 40 mm from the centre the temperature rises from 20 °C at 1 slpm to 35 °C at 2.5 slpm as greater volumes of heated helium displace colder ambient around the device. A comparison of power modulation and convection cooling is shown in figure 6.13. The duty cycle is varied for an inlet flow of 1 slpm here. Figure 6.13 demonstrates a significantly larger

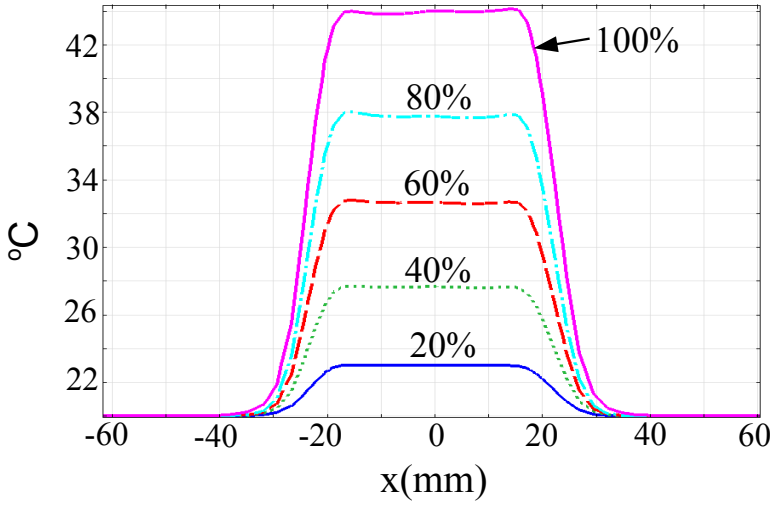

Figure 6.11: Gas temperature (°C) at an insulated treatment surface (BC in figure 6.1) at 10 mm below the device for a range of duty cycles: gas flow = 1.0 slpm (inlet at HI in figure 6.1), $V_{applied}$ = 325 V, O_2 admixture = 0.6%, modulation frequency 100 kHz

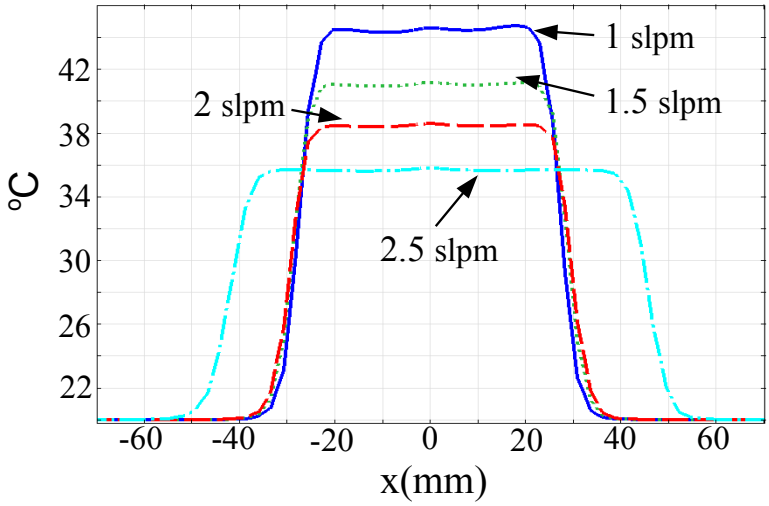

Figure 6.12: Gas temperature (°C) at an insulated treatment surface (BC in figure 6.1) at 10 mm below the device for a range of volumetric flow rates (inlet at HI in figure 6.1), $V_{applied}$ = 325 V, O_2 admixture = 0.6%, modulation frequency 100 kHz for a 100 % duty cycle

range of temperature control using power modulation than gas cooling by convection. Convection cooling shows a saturation behaviour at higher gas flows in comparison to duty cycle variation between 20 - 100 % which gives linear control of surface temperatures. Lowering heat flux to a treatment surface at a prescribed distance without changing the gas flow maybe advantageous in some application scenarios. For example in the use of atmospheric jets in clinical settings where patients find large gas flows uncomfortable or when large gas flows may undesirably disturb

surface materials.

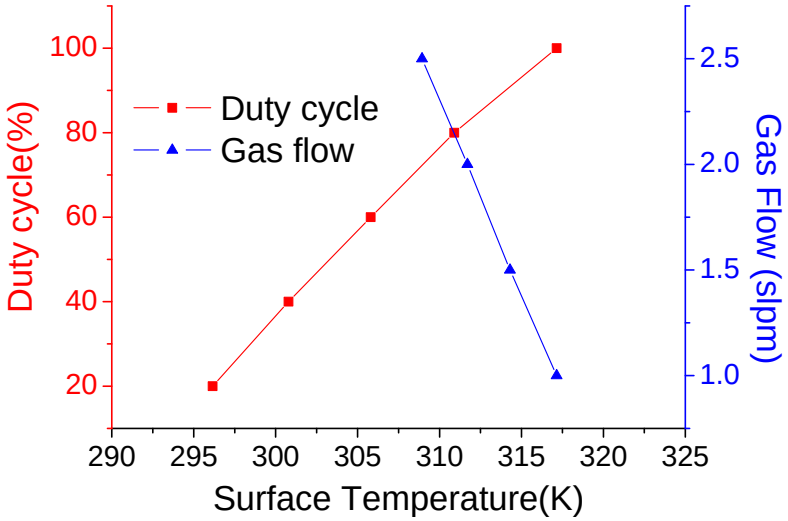

Figure 6.13: Comparison of steady state surface temperature (°K) over an insulated surface (BC in figure 6.1) at 10 mm below the device for variation in duty cycle (at 1 slpm) and volumetric flow rate (1 - 2.5 slpm) $V_{applied}$ = 325 V, O_2 admixture = 0.6%, modulation frequency 100 kHz

6.3.3 Power modulated reactive species behaviour

The continuous phase and volume averaged atomic oxygen production R_{avg} (t) (see section 6.2) is shown in figure 6.14 for a range of duty cycles. Atomic oxygen production follows the power growth here (see figure 6.2). This is due to the strong coupling of power to the electron density and energy which directly effect the dominant O production reactions (R_{12}, R_{13} in table 6.1). Peak production values at a steady state power (> 3 μs) of 6.4 $\times$ 10^{24} $m^{-3}s^{-1}$ are shown in figure 6.14.

2-D solutions from a reacting and mixing gas model of neutral (uncharged) plasma produced reactive species (see section 6.2) with a fixed gas temperature of 300 K is shown for O density (ppm) in figure 6.15 on a treatment surface (BC in figure 6.1) for a range of duty cycles. Peak O values are contained here within a radius of 20 - 25 mm from the centre corresponding to the device width (KL-GF in figure 6.1). Peak O density of 19 ppm (4.9 $\times$ 10^{20} 1/m^3) occurs in the centre ($x \sim 0$) for 100 % duty cycle with values of 17.9, 15, 11.3 and 6.3 ppm for 80, 60, 40 and 20 % duty cycle respectively. The change between 40 - 100 % show a similar increment of $\sim$ 3 ppm per 20 % increase in duty cycle. The larger O increase from 20 - 40 % ($\sim$ 5 ppm) is due to the operation at a steady state power ($> 30\%$) for a portion of the duty cycle. At a smaller device to surface separation of 5 mm surface O density is found to range from 15 ppm to 49 ppm for 20% - 100 % duty cycle variation. Limited conversion of atomic oxygen to ozone via O_2 (O + O_2 + He $\rightarrow$ O_3 + He (see R_2 in table 4.2 in chapter 4) results in a larger O density at the treated surface here. This is a result of lower O_2 concentration in the gas mixture and reduced residence time for O conversion to O_3 at smaller separations. For a larger device separation of 15 mm a range of 1.7

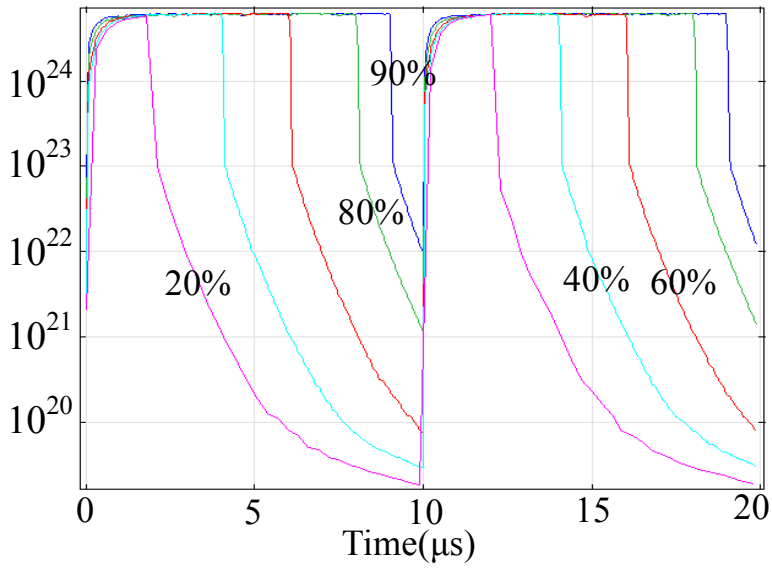

Figure 6.14: Atomic oxygen production R_{avg} (t) $m^{-3}s^{-1}$ over a modulation period for a range of duty cycles: $V_{applied}$ = 325 V, O_2 admixture = 0.6%, modulation frequency 100 kHz

ppm to 7.8 ppm for 20% - 100 % duty cycle variation is found consistent with higher O losses due to increased O_2 and reaction time at higher device to surface separations.

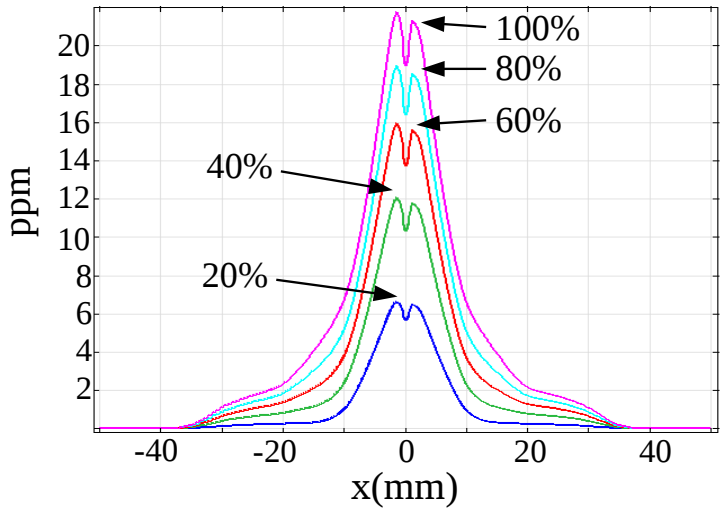

Figure 6.15: O density at surface (BC in figure 6.1) at 10 mm below the device for variation in duty cycle: Gas flow = 1 slpm, $V_{applied}$ = 325 V, O_2 admixture = 0.6%, modulation frequency 100 kHz

Surface plots for O_2 ($a^1\Delta$) and O_3 density for steady state solution of the 2-D reacting and mixing gas model is shown in figures 6.16 and 6.17. O_2 ($a^1\Delta$) values at the central peak range from 127 ppm (3.1×10^{21} $1/m^3$) at 100 % duty cycle, 100 ppm at 80 %, 75 ppm at 60 %, 49 ppm at 40 % and 22 ppm at 20%. O_3 values at the central peak range from 270 ppm (6.6×10^{21} $1/m^3$)

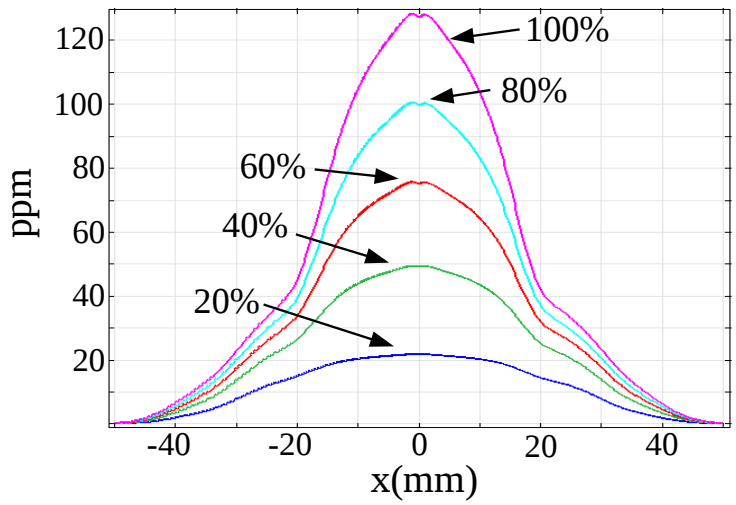

Figure 6.16: O_2 ($a^1\Delta$) density at surface (BC in figure 6.1) at 10 mm below the device for variation in duty cycle: Gas flow = 1 slpm, $V_{applied}$ = 325 V, O_2 admixture = 0.6%, modulation frequency 100 kHz

at 100 % duty cycle, 234 ppm at 80 %, 195 ppm at 60 %, 143 ppm at 40 % and 74 ppm at 20%. At smaller separations between the device and surface of 5 mm; surface O_2 ($a^1\Delta$) range from 155 - 24 ppm while O_3 from 258 - 67 ppm for 100% - 20 % duty cycle variation. At a 15 mm separation surface O_2 ($a^1\Delta$) range from 107 - 19 ppm and O_3 range from 268 - 73 ppm for 100% - 20 % duty cycle variation. The increase of O_2 ($a^1\Delta$) at 5 mm and decrease at 15 mm is due to its interaction with O_3 (O_2 ($a^1\Delta$) + $O_3 \rightarrow$ O + $2O_2$ (see R_{11} in table 4.2 in chapter 4).

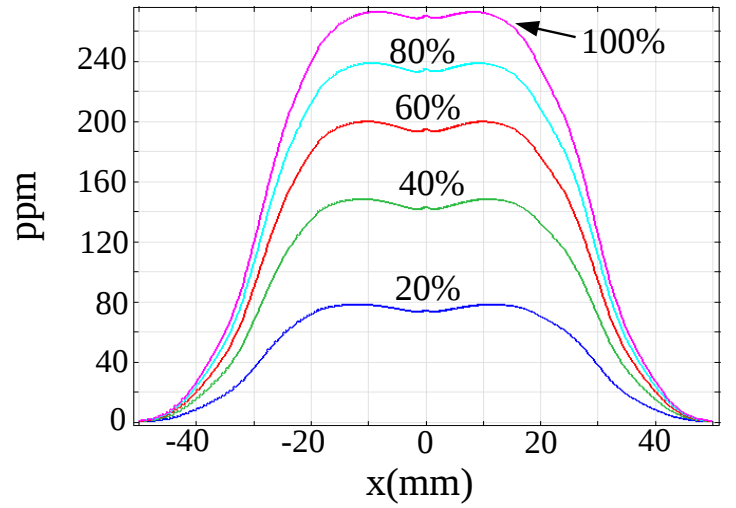

Figure 6.17: O_3 density at surface (BC in figure 6.1) at 10 mm below the device for variation in duty cycle: Gas flow = 1 slpm, $V_{applied}$ = 325 V, O_2 admixture = 0.6%, modulation frequency 100 kHz

6.4 Conclusion

Power modulation is demonstrated as an effective mechanism here for control of reactive species and heat flux delivery to a surface. Reactive species generation and gas heating in a power modulated capacitively coupled radio frequency plasma jet is investigated by numerical modelling. Power growth consists of an initial phase of exponential growth before transition to asymptotic convergence to a steady state value ($\sim$ 2 - 3 μs). Power is found to be coupled extensively to the electrons with electron loss rates determining the interference between successive modulation phases. Plasma decay is characterised by a large initial electron loss with $\sim$ 80 % of the steady state density lost in the first 0.5 μs. This period is followed by increasing electro-negativity in the plasma and a decay dominated by ions of opposite charge for the remainder of the power-off period. Large initial electron losses lead to weak interference between successive modulation phases. The initial decay period sets a limit for interference between successive power pulses which could significantly shorten the initial growth period in electron density ($\sim$ 2 - 3 μs).

Power modulation effects on gas heating are shown to limit heat more effectively than cooling by convection at a treated surface. Surface densities of O, O_2 ($a^1\Delta$) and O_3 reactive oxygen species on a treatment surface 10 mm below the device are found to typically range over an order of magnitude for variation in the duty cycle above the initial growth phase ($\sim$ 20 %).

Chapter 7

Frequency variation

Abstract

Control of reactive oxygen species generation and gas heating by variation in the applied voltage frequency for a dielectric barrier discharge is discussed. A $\sim$ kHz frequency driven device operating in a glow discharge mode at atmospheric pressure in helium with oxygen admixtures is considered. Frequency increase interrupts plasma decay between gas breakdown in each half cycle of the voltage phase leading to greater power deposition. Spatial behaviour of species density in a vertically orientated large area device operating in the ambient is presented. Steady state atomic oxygen, molecular oxygen metastable and ozone density are shown to increase uniformly along the central axis of the device for increase in frequency. Molecular oxygen metastable and ozone production is found to be coupled strongly to the amount of oxygen admixture. Gas heating by the plasma is dominated by positive ion heating with significant contributions from elastic electron collisional and negative ion heating.

7.1 Introduction

The study of atmospheric pressure plasmas offers not only the potential for new technological advances but improvements and cost reductions to many existing industrial plasma processes. One immediate advantage is the removal of pressure systems which often limit in-line addition of plasma treatments to existing industrial infrastructures. *Dielectric barrier discharge* sources have been applied in a variety of material treatments [25, 26]. One popular arrangement of the source is an extension of the planar capacitively coupled geometry to include a layer of dielectric material on one or both of the electrodes. This allows plasma formation at larger gap widths ($\sim$ 5 mm) than capacitively coupled counterparts. Dielectric barrier discharges are typically driven at $\sim$ kHz frequencies to allow sufficient time for surface charge to accumulate on the dielectrics. Voltage induced by this surface charge results in the pulsed plasma behaviour characteristic of the source (see chapter 3). Conditions for a diffuse mode of plasma operation with a helium carrier

gas known as a *glow discharge* [8, 9] is considered here.

Frequency variation is investigated here as a mechanism for varying the power deposition to the plasma allowing control of reactive species production and heat flux. The pulsed nature of this ∼kHz driven discharge (see chapter 3) allows frequency variation to significantly alter power deposition to the plasma by interrupting the period between plasma growth and decay. Variation in frequency allows more frequent plasma pulsing compared with voltage variation which increases the intensity of each plasma pulse. Voltage variation has a lower limit to sustain the plasma and upper limit at plasma transition to an arcing mode. This range of operational powers is often small having a non-linear behaviour for a given frequency and oxygen admixture. This behaviour limits the control potential of voltage variation and therefore alternative control opportunities via frequency variation is of interest here. In comparison to vacuum constrained plasma treatments open air systems can continually pass a material between a plasma device allowing high volume throughput and the possibility of in-line integration to existing industrial systems. Examples of industrial scale implementations of atmospheric pressure DBD's include the *Dow Corning Labline* and *SE-1000 AP4* atmospheric pressure plasma pilot systems [135, 136, 137]. The geometry constructed here represents a large scale implementation of a dielectric barrier discharge for *surface engineering applications* in an open air environment. This *chapter* focuses on the potential to control the reactive oxygen species production and gas heating by varying the frequency using O_2 admixtures $\sim 1\%$ typically employed in industrial applications. The critical role of small amounts of N_2 impurity in plasma formation for helium discharges via penning ionisation has been studied numerically in several previous reports [44, 95, 96]. Numerical investigations for helium-O_2 mixtures [97, 98, 99] for the source have considered the 'quenching' effects of small oxygen admixtures ($\sim$ 10 ppm) on plasma dynamics and the ability of frequency variation to recover the glow mode of operation. Similar to earlier studies of the plasma needle and μAPPJ investigation of the plasma produced reactive species, heating and gas dynamics provides a novel insight into the reactive species and heat flux produced by an industrial scale implementation of this source.

In section 7.2 the model strategy is outlined. Section 7.3 details results of one and two dimensional numerical models employed here. Electrical parameters and charged species behaviour is discussed in section 7.3.1. Gas mixing and heating results from 2-D models are outlined in section 7.3.2. The steady state reactive oxygen species density produced in the device are finally discussed in section 7.3.3.

7.2 Model description

The *dielectric barrier discharge* (DBD) consists of two dielectric quartz layers of thickness 1 mm sitting on 4 mm steel electrodes with a separation between the dielectric layers of 5 mm. One electrode is driven with a sinusoidal applied voltage while the other electrode is grounded. The sinusoidal applied voltage with frequency f is given by $V_a sin(2\pi ft)$ where V_a is the applied volt-

age amplitude. A 1-D model of the plasma dynamics is solved until steady state power conditions are reached in the plasma ($\sim \mu$s). Phase averaged (over the applied voltage phase) reactive uncharged species production rates (O, O_3..) are then extrapolated from the 1-D plasma model across the 2-D discharge domain ($ILGH$ in figure 7.1) and coupled to a 2-D model of the reacting and mixing helium carrier jet in the ambient. The 2-D geometry employed here is shown in figure 7.1.

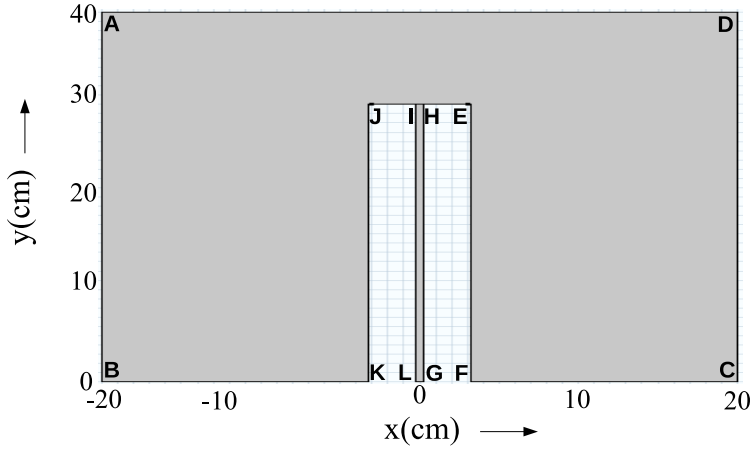

Figure 7.1: Dielectric barrier geometry

The device geometry spans 300 mm and has a vertical orientation with a gas flow inlet at the bottom of the domain (LG in figure 7.1). Mass and momentum continuity equations (compressible Navier-Stokes) are coupled to a mass transport equation to study the two dimensional gas dynamics of the helium jet mixing and reacting in the surrounding air. Gas heating by the plasma is considered by inclusion of a phase averaged heating term extrapolated from solutions of the 1-D plasma model across the 300 x 5 mm discharge domain ($ILGH$ in figure 7.1) as a source term in a 2-D heat model. Further details of the modelling strategy, boundary conditions and chemistry used here can be found in chapter 5.

7.3 Results and discussion

Results of one and two dimensional models for a helium dielectric barrier discharge with 0.1% and 1% oxygen admixtures for a range of applied voltage frequency up to 200 kHz is discussed here. Electrical parameters, charged species behaviour, power and reactive oxygen species production results from a 1-D plasma model are discussed in section 7.3.1. Gas mixing and heating results from a 2-D model of an uncharged gas (see section 7.2) are outlined in section 7.3.2. The steady state reactive oxygen species density produced in the device are discussed in section 7.3.3.

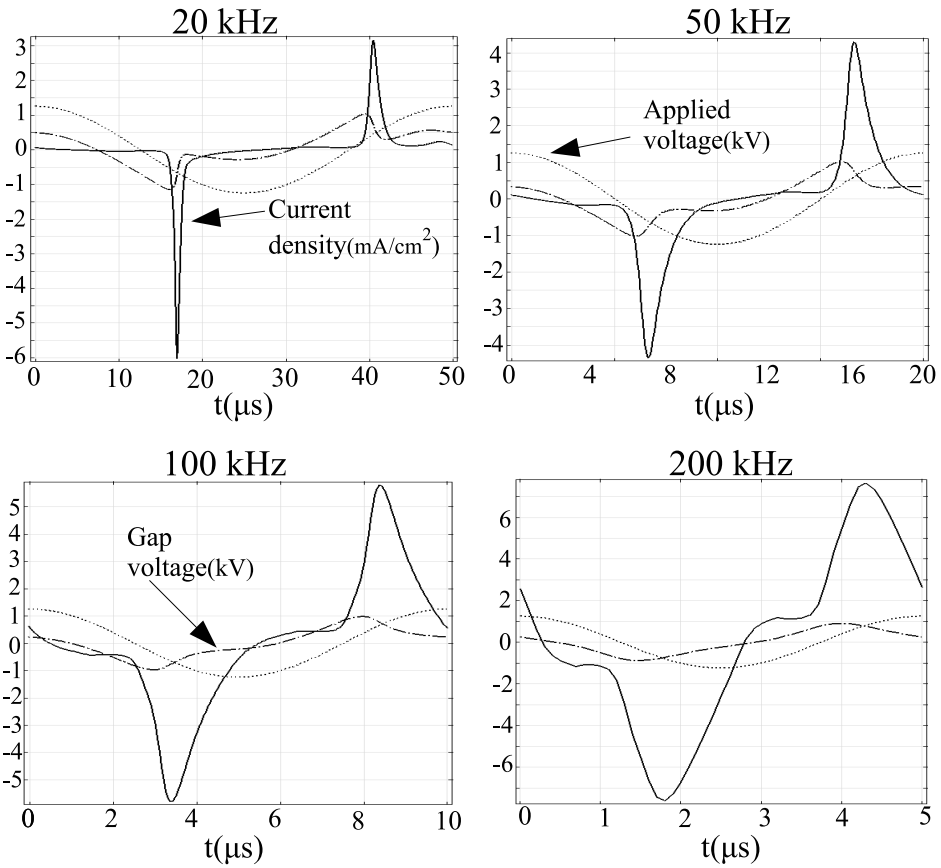

Figure 7.2: Electrical parameters for a range of applied voltages frequency (20 - 200 kHz): V_a = 1.25 kV and O_2 = 0.1 %.

7.3.1 Plasma behaviour

Electrical parameters for a range of applied voltage frequency conditions are shown in figure 7.2 for a fixed voltage amplitude of 1.25 kV and O_2 admixture of 0.1 %. A current pulse is observed on every half cycle of the applied voltage phase characteristic of a glow mode of operation [8, 9, 11, 107]. Surface charge accumulation on the electrodes during each half cycle results in an opposing voltage (memory voltage V_m) to that which is applied. A subsequent peak in the gap voltage (figure 7.2) occurs when the applied voltage polarity switches passing through zero. This dynamic creates a pulsed plasma behaviour where charged species are continually created and destroyed between peaks in the gap voltage as $V_a \rightarrow 0$. Electrical parameters for V_a = 2 kV and O_2 = 1 % admixture from 50 kHz to 200 kHz have a similar behaviour to that shown in figure 7.2. At a 20 kHz frequency however high current amplitudes (> 20 mA/cm^2) occurred signifying arcing behaviour.

Figure 7.2 demonstrates how increasing the applied voltage frequency leads to an increase in the regularity and amplitude of current pulses. This results in an increase in the power deposition

to the plasma. At a O_2 = 0.1 % admixture and an applied voltage amplitude of V_a = 1.25 kV the average (phase and volume) power deposition ranges from 1.19 $\times$ 10^5 Wm^{-3} at 20 kHz, 5.43 $\times$ 10^5 Wm^{-3} at 50 kHz, 1.3 $\times$ 10^6 Wm^{-3} at 100 kHz, 2.07 $\times$ 10^6 Wm^{-3} at 150 kHz to 2.796 $\times$ 10^6 Wm^{-3} at 200 kHz. This represents an approx 22 times increase in power deposition from 20 kHz to 200 kHz. The average percentage of total power coupled to electrons at 20 kHz is 79.7 % increasing to 82.7 % at 200 kHz. The fraction of power coupled to negative ions at 20 kHz is 15.1 % decreasing to 14.6 % at 200 kHz with corresponding average electro-negativity values of 6.07 and 1.03 respectively. At a O_2 = 1 % admixture and an applied voltage amplitude of V_a = 2 kV average powers of 1.3 $\times$ 10^6 Wm^{-3} and 6.75 $\times$ 10^6 Wm^{-3} at 50 kHz and 200 kHz represent a 5 fold increase in power deposition. The average percentage of total power coupled to electrons at 50 kHz is 92.4 % decreasing to 91.6 % at 200 kHz. The power contribution for negative ions is 7.1 % at 50 kHz and 7.3 % at 200 kHz with corresponding average electro-negativity of 2.64 and 2.05 respectively. A smaller decrease in electro-negativity with frequency increase at a 1 % O_2 (V_a = 2 kV) compared to a 0.1 % O_2 (V_a = 1.25 kV) manifests in a smaller increase in average power deposition due to the fact that external power is coupled more efficiently to electrons over negative ions.

The asymmetry in the current density shown in figure 7.2 at 20 kHz arises from a differential in the gas breakdown time between half cycles of the applied voltage phase. The gap voltage and current density peaks occur earlier for the smaller current amplitude than for the larger current peak. Earlier breakdown results in a reduction in the voltage across the gap as the memory voltage is limited by the opposing externally applied voltage. Occurrence of asymmetric behaviour is found to be reduced by frequency increase. This is primarily due to the reduction in electron decay reducing the differential in residual electrons between each half voltage cycles (see chapter 3 for further discussion). Penning ionisation reactions of helium excited species (He^*, He_2) with O_2 are found to be the dominant ionisation source here accounting for 91.6% of the average (volume and phase) total ionisation at 20 kHz and 95 % at 200 kHz (V_a = 1.25 kV, 0.1 % O_2). For V_a = 2 kV and O_2 = 1 % penning ionisation contributions are lower with average values of 64.8 % at 50 kHz and 59.3 % at 200 kHz. The remaining contribution here is from direct ionisation of O_2 with values of 35 % at 50 kHz and 41.1 % at 200 kHz.

The volume average charged species behaviour over an applied voltage cycle for V_a = 1.25 kV and O_2 = 0.1 % is shown in figure 7.3. At 20 kHz (figure 7.3 (left)) the asymmetric electron density reflects the asymmetric current behaviour shown in figure 7.2. The electron density ranges from peak values of $\sim$ 10^{17} m^{-3} to minimum values of $\sim$ 10^{13} - 10^{14} m^{-3} within each half cycle of the applied voltage. The dominant positive charge carrier here is O_2^+ with peak values of $\sim$ 10^{16} - 10^{17} m^{-3}. Negative charge is carried by electrons and negative ions (O^- O_2^-) with average (phase and volume) electro-negativity of 6.07. Figure 7.3 at 20 kHz shows plasma decay between current peaks is dominated by ions of opposite charge with a larger electron loss rate than other charge carriers. Negative charge transfer reactions (electron attachment, detachment)

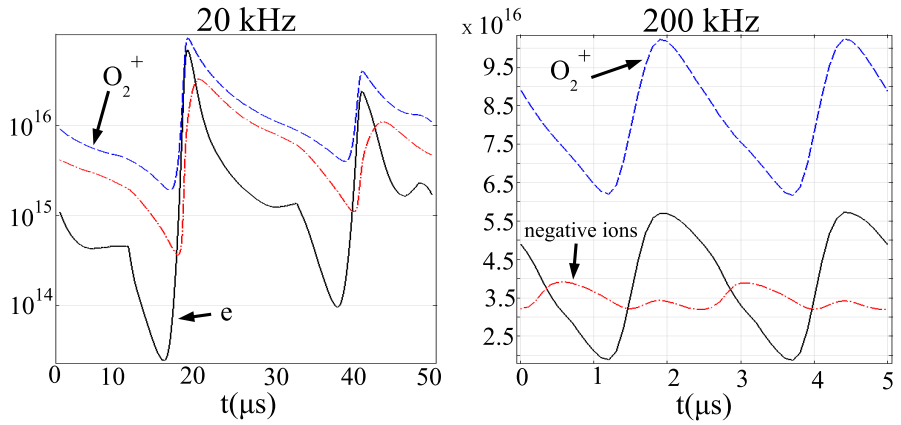

Figure 7.3: Volume averaged charged species density for 20 kHz (left) and 200 kHz (right): V_a = 1.25 kV and O_2 = 0.1 %.

are found to dominate over electron/ion recombination processes in the decay phase of the plasma between current pulses (see chapter 3 for discussion). Mean electron energy values range on average (volume) from 0.97 - 2.79 eV over the applied voltage phase with an overall average (volume and phase) value of 2.26 eV. At 200 kHz the electron density is maintained between 2 - 5.5 $\times$ 10^{17} m^{-3} within each half cycle. Electron decay is limited by the increased regularity of the applied voltage. O_2^+ with peak values of $\sim$ 10^{16} - 10^{17} m^{-3}. O_2^+ values range between $\sim$ 6 - 9.5 $\times$ 10^{16} m^{-3}. Negative ion density are maintained between $\sim$ 3 - 4 $\times$ 10^{16} m^{-3} for average electro-negativity value of 1.03. Mean electron energy values here range from 0.21 - 3.47 eV with an average (volume and phase) value of 1.73 eV.

The volume average reactive oxygen species production over an applied voltage phase is shown in figure 7.4. Peak O production values over the applied voltage cycle for a 0.1 % O_2 (V_a = 1.25 kV) admixture range from 4 - 8 $\times$ 10^{23} $m^{-3}s$ for 50 - 200 kHz frequency variation (figure 7.4 (top)). Average (volume and phase) O production values for 50 - 200 kHz range from 3.3 - 15.3 $\times$ 10^{22} $m^{-3}s$ here. At a 0.1 % O_2 (V_a = 1.25 kV) admixture peak O production increases ranging from 2.2 - 8 $\times$ 10^{24} $m^{-3}s$ over an applied voltage cycle (figure 7.4 (bottom)). Average (volume and phase) O production values range from 4.43 - 24.9 $\times$ 10^{22} $m^{-3}s$ for 50 - 200 kHz. Dissociation of O_2 forming O and O (^{1}D) (reaction R_{17} in table 3.1) dominates production here. Average contributions to O production for a 0.1 % O_2 (V_a = 1.25 kV) admixture at 50 kHz and 200 kHz are 72 % and 70.3 %. At 1 % O_2 (V_a = 2 kV) average contributions of 70.1 % and 70.3 % for 50 kHz and 200 kHz. O_2 dissociation producing two atomic oxygen species (reaction R_{16} in table 3.1) also contributes significantly with average values of 25 % and 25.2 % for O_2 = 0.1 % (V_a = 1.25 kV) at 50 kHz and 200 kHz respectively with corresponding values of 26.6 % and 26.5 % for O_2 = 1 % (V_a = 2 kV). Production of O_2 ($a^1\Delta$) shows a similar pattern to O/O (^{1}D) production with typical peak values $\approx$ 50 % smaller (see figure 7.4). Spatial variation in the atomic oxygen production across the discharge gap is shown in figure 7.5 at 50kHz and 200kHz.

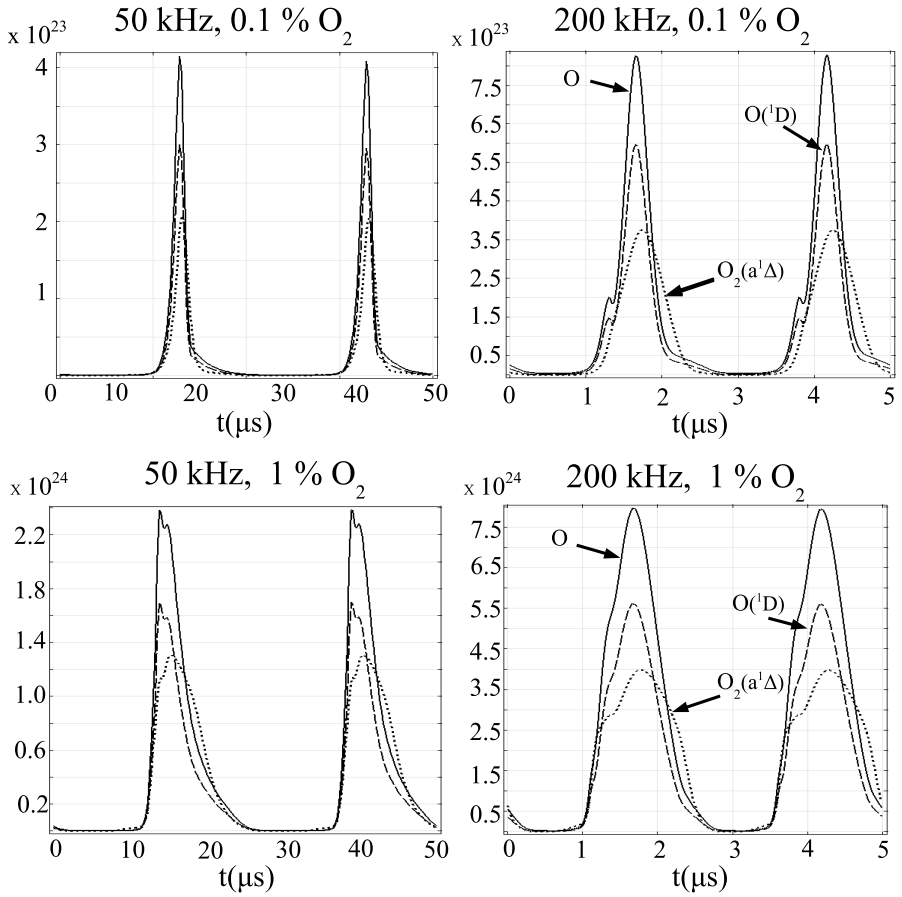

Figure 7.4: Volume averaged O, O_2 ($a^1\Delta$), O (^1D) production m^3s^{-1}. Top: V_a = 1.25 kV and O_2 = 0.1 % and bottom: V_a = 2 kV and O_2 = 1 %

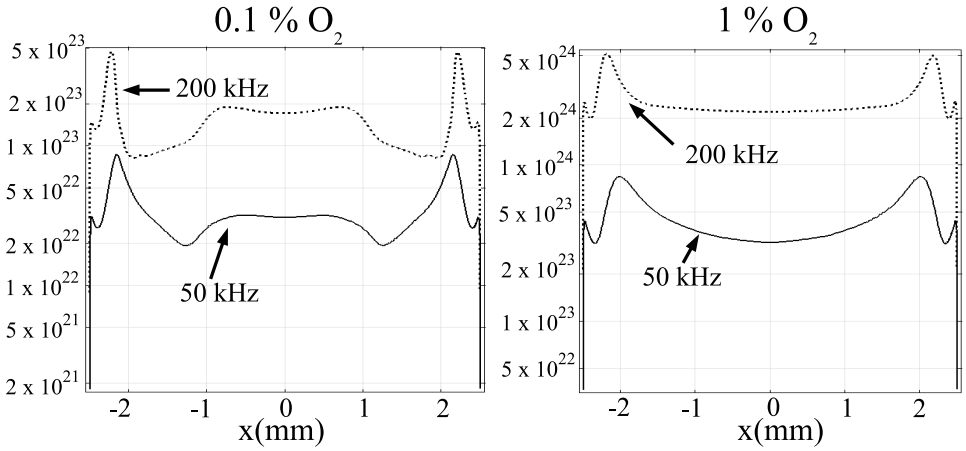

Figure 7.5: Time averaged (over applied voltage phase) O production m^3s^{-1} across discharge gap for V_a = 1.25 kV, O_2 = 0.1 % (left) and V_a = 2 kV, O_2 = 1 % (right)

Peak production values are shown to occur in the edge of the discharge region where maximum density charged particles occur during each current pulse.

7.3.2 Gas mixing & heating

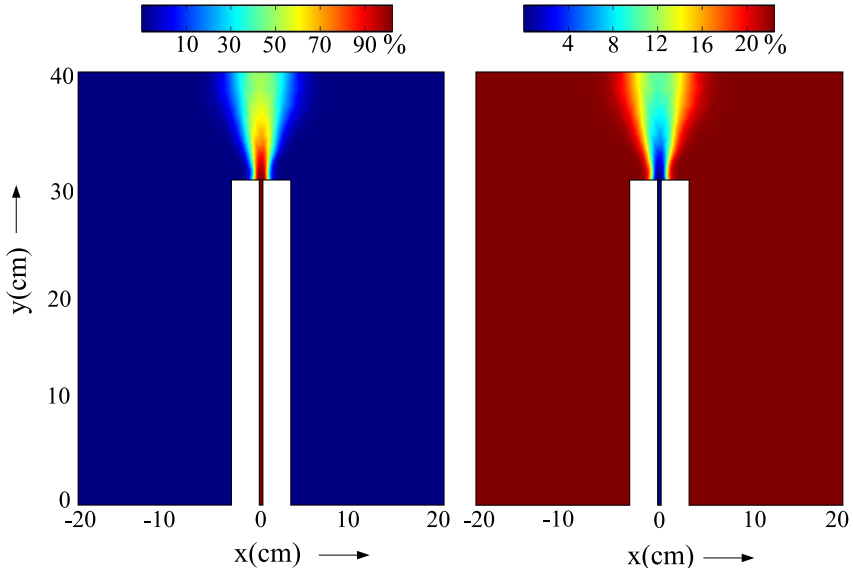

Figure 7.6: Percentage helium (left) and oxygen (right) in gas mixture across domain. Inlet flow = 15 splm

The steady state percentage of helium and oxygen for a helium jet with a 0.1% O_2 admixture is shown in figure 7.6. The oxygen content (figure 7.6 (right)) maintains a uniform percentage of 0.1 % inside the device at the admixed value. Outside the electrode region above the device helium (figure 7.6 (left)) mixes with the ambient oxygen (20 %) and nitrogen (80 %). The on axis (x = 0) gas mixture at y = 40 cm is made up of 46 % helium, 11 % O_2 and 43 % N_2. Lateral mixing of helium is more abrupt with values dropping below 1 % off axis at x = 4 cm, y = 40 cm.

In figure 7.7 we see the percentage contribution to the total gas heating by the plasma at 50 kHz for a 0.1 % O_2 (V_a = 1.25 kV) admixture from our 1-D plasma model results for the volume average heat deposition (W/m^3) over a steady state applied voltage phase. The average (volume and phase) total heat deposited by the plasma to the gas is 8.17 $\times$ 10^5 W/m^3. Positive ion heating by the electric field accounts for 59.1 % of the heating (volume and phase average contribution). Elastic collisional heating (R_1 in table 3.1) accounts for 28.7 % of the heating here. Negative ion heating accounts for 6.8 % of the total heating. The remaining heating is dominated by inelastic collisions between heavy species (5.4 %). For a 0.1 % O_2 (V_a = 1.25 kV) admixture at 200 kHz the average (volume and phase) heat deposited by the plasma to the gas is 3.97 $\times$ 10^6 W/m^3 with similar contributions to gas heating as described for 50 kHz above.

Figure 7.8 shows a 2-D steady state temperature profile for an inlet flow of 15 splm from solutions of the 2-D heating and mixing gas model. Steady state solutions are reached after ap-

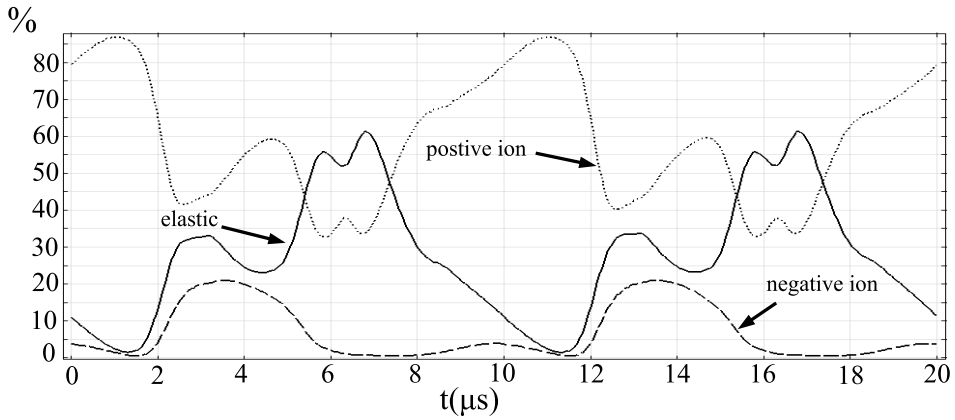

Figure 7.7: Percentage contributions to gas heating over applied voltage phase, f = 50 kHz, V_a = 1.25 kV, O_2 = 0.1 %

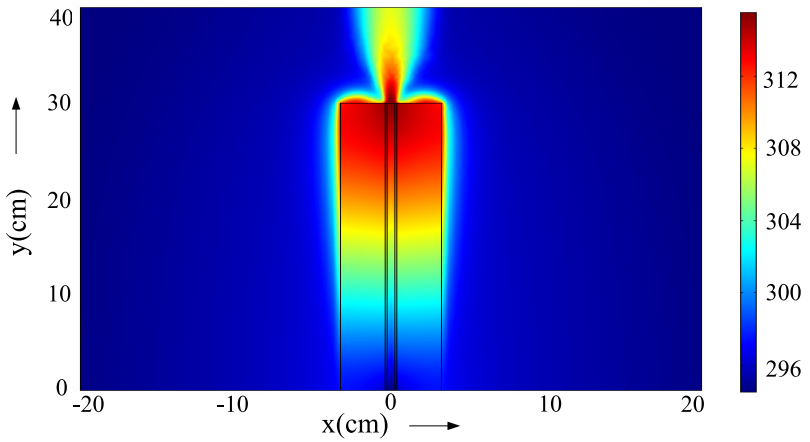

Figure 7.8: Steady state temperature profile for 150kHz, 1.25kV, 0.1% O_2. Inlet flow = 15 splm

proximately 2000 seconds. A maximum temperature of 313 K is found in the domain with values ranging from 293 to 313 K. Figure 7.9 shows the steady state vertical axis (at x = 0) gas temperature for a range of inlet flows. Gas temperature increases in the direction of gas flow with peak values at the top of the device. Significant cooling results from variation in the gas flow here. Peak steady state temperatures occurring at y = 30 cm (see figure 7.9) range from 91.5 °C at inlet flows of 5 slpm to 38.3 °C at 20 slpm. The successive reduction in peak temperature for each 5 slpm increase in flow ranges is given by δT = 32.9 °C for 5 to 10 slpm, δT = 12.9 °C for 10 to 15 slpm and δT = 7.4 °C for 15 to 20 splm. This shows a diminishing trend in heat reduction at higher flows.

Steady state temperature results along the axis (x = 0) for variation in the frequency at an inlet flow of 15 slpm is shown in figure 7.10. For O_2 = 0.1 % (V_a = 1.25 kV) peak steady state temperatures occurring at y = 30 cm (see figure 7.9 (top)) range from 21.87 °C at 20 kHz to 45.7

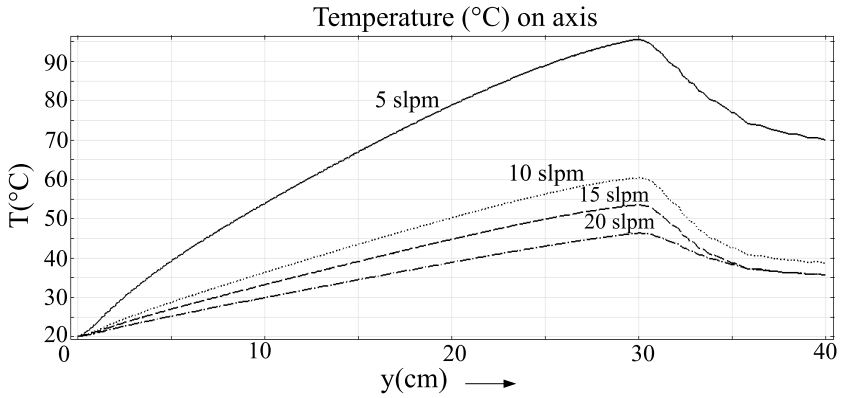

Figure 7.9: Steady state axial temperature (x = 0) for flow variation (5, 10, 15, 20 splm): 200kHz, 1.25kV, 0.1% O_2,

°C at 200 kHz. Peak temperature change (at x = 0) for increase in frequency is found to be more uniform here compared with flow variation with δT = 7 °C for 50 to 100 kHz, δT = 7.1 °C for 100 to 150 kHz and δT = 6.4 °C for 150 to 200 kHz. For O_2 = 1 % (V_a = 2 kV) peak steady state temperatures occurring at y = 30 cm (see figure 7.9 (bottom)) range from 30.7 °C at 50 kHz to 71.4 °C at 200 kHz. Peak temperature change (at x = 0) for increase in frequency has similar behaviour with δT = 13.3 °C for 50 to 100 kHz, δT = 13.7 °C for 100 to 150 kHz and δT = 13.7 °C for 150 to 200 kHz.

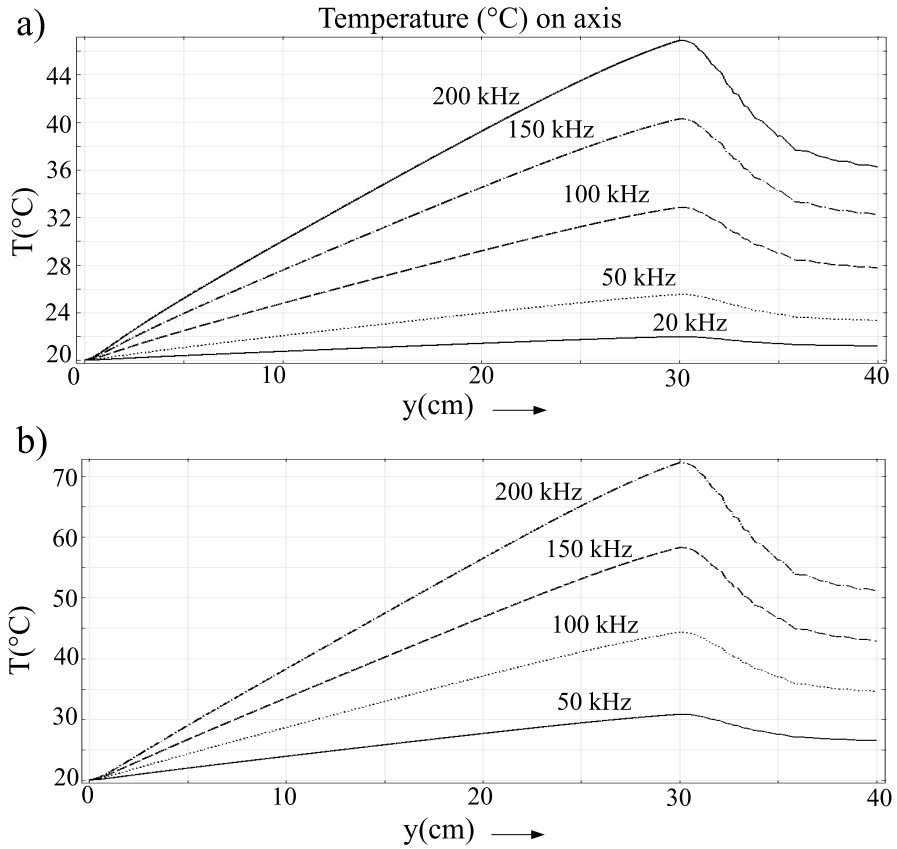

Figure 7.10: Steady state axial temperature (x = 0) for frequency variation (Inlet flow = 15 splm): Top (a): 20 - 200kHz, V_a = 1.25kV, 0.1% O_2. Bottom (b): 50 - 200 kHz: V_a = 2kV, O_2 = 1%

7.3.3 Reactive oxygen species

Figure 7.11 shows the number density of O and O_2 ($a^1\Delta$) for steady state solutions of a 2-D reacting gas model at 200 kHz for a fixed voltage amplitude of 1.25 kV and O_2 admixture of 0.1%. Peak O density of $\sim 7 \times 10^{20}$ is found where the carrier gas exits the device (y = 30 cm). O_2 ($a^1\Delta$) peak density of $\sim 6 \times 10^{20}$ is also found where the carrier gas exits the device (y = 30 cm). Outside the device the atomic oxygen drops sharply due to the increasing O_2 present in the gas mixture (see figure 7.6) which results in conversion to ozone (R_2 in table 4.2). O_2 ($a^1\Delta$) density drops at a slower rate and is primarily quenched by interaction with O_3 (R_{11} in table 4.2).

A 1-D axial plot (x = 0) for O, O_2 ($a^1\Delta$) and O_3 density is shown in figure 7.12. The average axial density (see figure 7.12) taken over the interval $0 < y < 40$ cm for atomic oxygen ranges from 1.5 ppm at 20 kHz to 15.1 ppm at 200 kHz frequency. Axial averages for O_2 ($a^1\Delta$) give a range from 0.8 ppm to 13.4 ppm between 20 kHz and 200 kHz. Axial averages for O_3 give similar values with a range of 1.3 ppm to 12.9 ppm between 20 kHz and 200 kHz. Ozone formation inside the device is dependent here on the O_2 admixture (0.1 %) [90] which reacts (reaction R_2 in table 4.2) with atomic oxygen to form ozone.

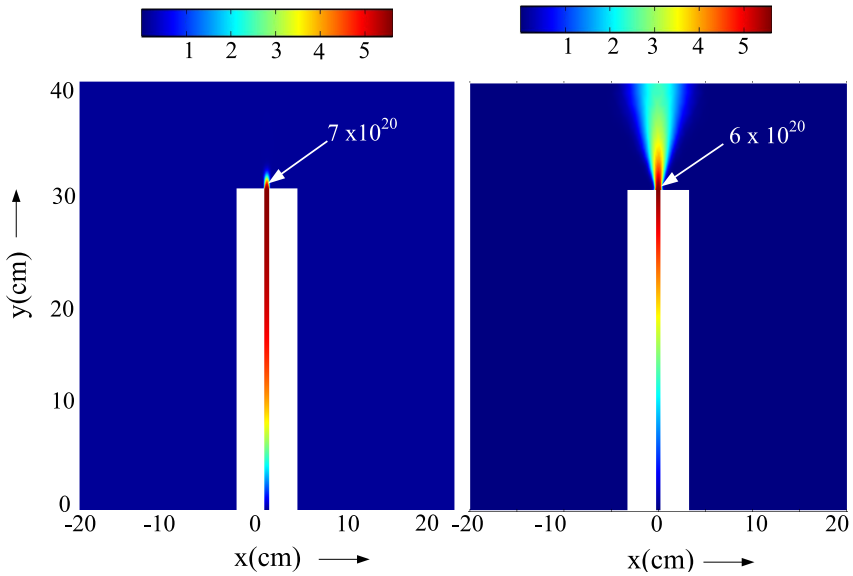

Figure 7.11: Steady state O (left) and O_2 ($a^1\Delta$) (right) density m^{-3} (Inlet flow = 15 splm): V_a = 1.25kV, O_2 = 0.1%

Figure 7.13 shows a similar 1-D axial plot (x = 0) for O, O_2 ($a^1\Delta$) and O_3 for O_2 = 1 % (V_a = 1.25 kV). A significantly higher ozone density is present here as a large proportion of the atomic oxygen generated is converted to ozone due to the 1 % O_2 admixture [90]. For O_2 = 1 % (V_a = 2 kV) the average axial density (see figure 7.13) for atomic oxygen ranges from 12.5 ppm at 50 kHz to 61.9 ppm at 200 kHz frequency. Axial averages for O_2 ($a^1\Delta$) are significantly higher ranging from 48 ppm to 188.6 ppm between 50 kHz and 200 kHz. O_3 axial averages show a large conversion of O to O_3 with values ranging from 91.9 ppm to 349.1 ppm between 50 kHz and 200 kHz.

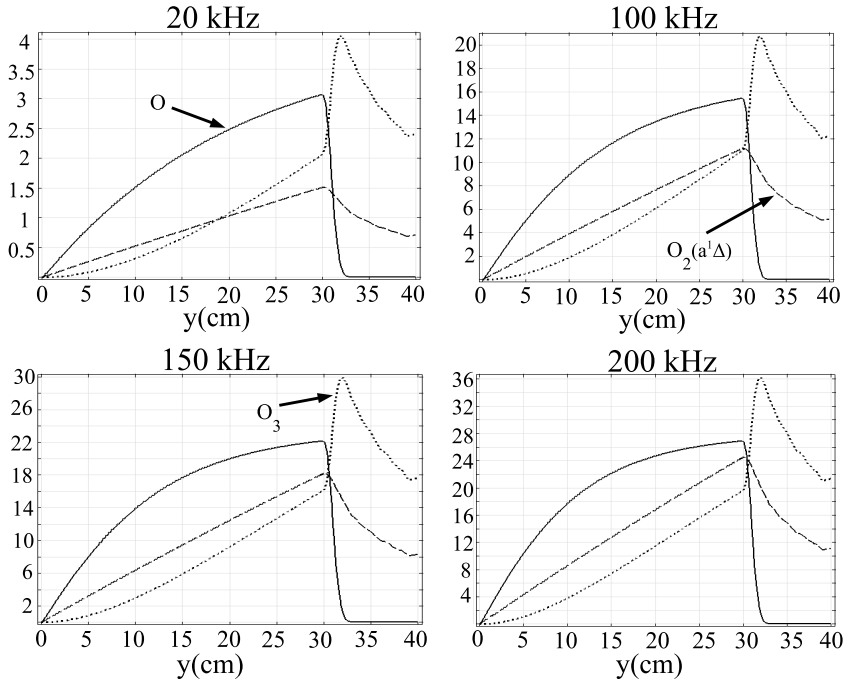

Figure 7.12: Steady state axial (x = 0) O, O_2 ($a^1\Delta$) and O_3 density m^{-3} for frequency variation (Inlet flow = 15 splm): V_a = 1.25kV, O_2 = 0.1%.

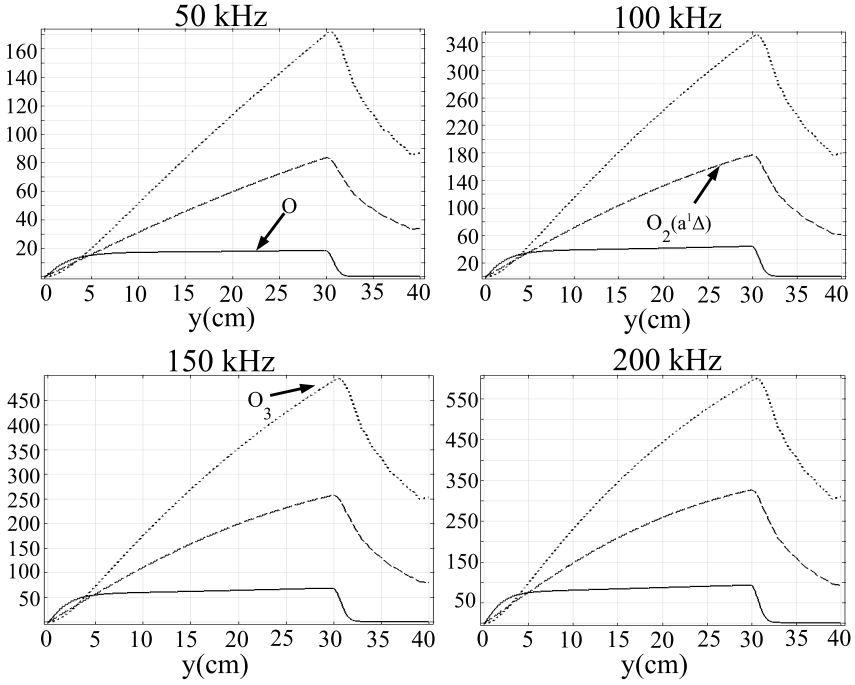

Figure 7.13: Steady state axial (x = 0) O, O_2 ($a^1\Delta$) and O_3 density m^{-3} for frequency variation (Inlet flow = 15 splm): V_a = 2kV, O_2 = 1%.

7.4 Conclusion

Frequency variation is demonstrated as a mechanism to control of reactive species production and heat flux in a large scale vertically orientated dielectric barrier discharge source. Frequency variation for this device typically driven in the $\sim$ kHz frequency range is shown here to vary power deposition to the plasma. Altering the frequency of the applied voltage varies the interval between current pulses occurring in each half cycle of the applied voltage phase. This changes the frequency of current pulses and the length of the plasma decay period within each half voltage cycle. This allows control of reactive species production and gas heating by changing the average power deposition to the plasma.

O, O_2 ($a^1\Delta$) and O_3 density are found to increase uniformly along the central axis of the device in the direction of gas flow for increase in frequency. O_2 ($a^1\Delta$) and O_3 production is found to be coupled strongly to the amount of O_2 admixture. Gas heating by the plasma is dominated by positive ion heating with significant contributions from elastic electron collisional and negative ion heating. Increased gas flow is shown to significantly lower the heating effect of the plasma on the effluent and electrodes.

Chapter 8

Conclusion

The emergence of medical applications of plasma in recent years has demonstrated their effectiveness as anti-bacterial agents, in promoting wound healing, treating skin infections and more recently in cell therapies targeting cancerous cells. The reactive species produced can chemically alter the bacterial or mammalian cellular environment promoting cell death or changing cell functionality. Application of atmospheric plasmas to change surface properties and precipitate thin film deposition opens up new avenues of utility currently restrained by the need for vacuum systems unworkable in many industrial environments. The behaviour of three low temperature atmospheric pressure helium plasma sources is investigated by execution of numerical models in this report. Electrical behaviour and *generation* dynamics for reactive species of oxygen, nitrogen and hydrogen produced by mixing or admixture of atmospheric gases is investigated. The effects of gas heating, gas flow and surface interaction is discussed in this context. Power modulation and frequency variation as *control* mechanisms for reactive species production and gas heating is discovered.

This work contributes in various ways to the advancement of the field. Numerical investigation of plasma jet gas dynamics highlights how the gas mixture determines the electro-positive/electro-negative character of the plasma and production profiles of reactive species. The use of complex geometries reflecting experimental conditions with broad reaction chemistry sets provides a significant advance in the current state of the art. Characterisation of the plasma produced chemistry reaching treatment surfaces and interaction analysis at this interface provides valuable insight into key species and actors in plasma effects in biomedicine and surface engineering applications. Investigation of gas heating informs the thermal stresses likely to influence application surfaces sensitive to thermal shock. Control methodologies outlined offer direction for delivery of reactive species and limitation of surface heating critical to the viability of future applications.

The behaviour of reactive species in the corona 'plasma needle' jet is investigated in *chapter 4*. Average plasma density ranging from 10^{16} to 10^{20} m^{-3} with mean electron energy values of 1 - 2.5 eV in the bulk discharge region were discovered. Peak production of atomic oxygen

due to interaction of the plasma with air species occurred at regions where the air fraction of gas mixture ranged from 10^{-3} to 10^{-2}. Gas flow variation showed surface atomic oxygen profiles which correlated to circular and annular shaped killing patterns previously reported in treated bacteria samples. Peak atomic oxygen density of 10^{21} and ozone density of 10^{22} m^{-3} were presented here. Surface loss studies revealed that atomic oxygen surface reactions on a reactive solid surface with adsorption probabilities greater than 0.1 are limited by the flux of atomic oxygen from the plasma. Interaction of the source with an aqueous surface showed hydrogen peroxide as the dominant species at this interface with significant hydroperoxyl radical, nitrous acid and nitric acid densities also present.

Reactive species generated in the *capacitively coupled* micro-Atmospheric Pressure Plasma Jet (μAPPJ) by admixture and interaction of the plasma effluent with the ambient air is presented in *chapter 5*. Production efficiency studies for O production shows peak production in the range 0.2 - 1 % O_2 with electro-negativity values close to unity. O, O_2 ($a^1\Delta$) and O_3 density profiles on a surface below the device were presented at a range of separations. Atomic oxygen is shown to react to form ozone with increasing device to surface separation as more molecular oxygen mixes from the ambient. Comparison at equivalent separations in a jet mixing in open air (without a solid boundary) highlights the difference between reactive species profiles expected in experimental diagnostics with and without a treatment surface. Comparison with experimental reports for atomic oxygen density values showed good agreement. Gas heating by the plasma is shown to be dominated by elastic and positive ion heating with significant contributions from negative ion heating. Steady state temperature profiles show maximum steady state temperatures of 315 K reached after approximately 500 seconds of device operation. Surface reactions on a reactive solid surface are demonstrated to be significantly diffusion limited for adsorption probabilities greater than 0.1. Interaction of the source with an aqueous surface showed hydrogen peroxide as the dominant species at this interface.

Power modulation is demonstrated as an effective mechanism for control of reactive species and heat flux delivery to a surface in *chapter 6*. Reactive species production and gas heating is found to be strongly coupled to power behaviour in the helium-oxygen capacitively coupled plasma jet discussed. Power growth is found to consist of an initial phase of exponential growth before transition to asymptotic convergence to a steady state value ($\sim$ 2 - 3 μs). Power is found to be coupled extensively to the electrons with electron loss rates determining the interference between successive modulation phases. Plasma decay is characterised by a large initial electron loss with $\sim$ 80 % of the steady state density lost in the first 0.5 μs. This period is followed by increasing electro-negativity in the plasma and a decay dominated by ions of opposite charge for the remainder of the power-off period. Large initial electron losses lead to weak interference between successive modulation phases. Power modulation effects on gas heating is shown to limit heating more effectively than cooling by convection at a treated surface. Surface densities

of O, O_2 ($a^1\Delta$) and O_3 reactive oxygen species on a treatment surface 10 mm below the device typically range over an order of magnitude for variation in the duty cycle above 20 %. This results demonstrate that power modulation is an effective mechanism to control reactive species and heat flux with specific interest to applications in biomedicine and heat sensitive surface engineering.

Frequency variation is demonstrated as a mechanism to control of reactive species production and heat flux in chapter 7. Frequency variation in a dielectric barrier discharge plasma source driven in the $\sim$ kHz frequency range is shown here to vary power deposition to the plasma. Altering the frequency of the applied voltage varies the interval between current pulses occurring in each half cycle of the applied voltage phase. This changes the frequency of current pulses and the length of the plasma decay period within each half voltage cycle. This allows control of reactive species production and gas heating by changing the average power deposition to the plasma. O, O_2 ($a^1\Delta$) and O_3 density increases uniformly along the central axis of the device in the direction of gas flow with frequency increase. O_2 ($a^1\Delta$) and O_3 production is found to be coupled strongly to the amount of O_2 admixture. Gas heating by the plasma is dominated by positive ion heating with significant contributions from elastic electron collisional and negative ion heating.

Bibliography

[1] Y. P. Raizer. *Gas Discharge Physics*. Springer, 1991.

[2] A. Fridman. *Plasma chemistry*. Cambridge University Press, 2008.

[3] LXcat. electron scattering database `http://www.lxcat.laplace.univ-tlse.fr/database.php`. *University of Toulouse*, 2013.

[4] M. A. Liebermann and A. J. Lichtenberg. *Principles of Plasma Discharges and Materials Processing*. Wiley, New York, 1994.

[5] G Y Park, S J Park, M Y Choi, I G Koo, J H Byun, J W Hong, J Y Sim, G J Collins, and J K Lee. Atmospheric-pressure plasma sources for biomedical applications. *Plasma Sources Science and Technology*, 21(4):043001, 2012.

[6] E Stoffels, A J Flikweert, W W Stoffels, and G M W Kroesen. Plasma needle: a non-destructive atmospheric plasma source for fine surface treatment of (bio)materials. *Plasma Sources Science and Technology*, 11(4):383, 2002.

[7] V. Schulz-von der Gathen, V. Buck, T. Gans, N. Knake, K. Niemi, St. Reuter, L. Schaper, and J. Winter. Optical diagnostics of micro discharge jets. *Contributions to Plasma Physics*, 47(7):510–519, 2007.

[8] S. Kanazawa, M. Kogoma, T. Moriwaki, and S. Okazaki. Stable glow plasma at atmospheric pressure. *J. Phys. D: Appl. Phys.*, 21(5):838, 1988.

[9] S Okazaki, M Kogoma, M Uehara, and Y Kimura. Appearance of stable glow discharge in air, argon, oxygen and nitrogen at atmospheric pressure using a 50 hz source. *J. Phys. D: Appl. Phys.*, 26, 1993.

[10] S. Sherwin J. Peiro. *Finite Difference, Finite Element and Finite Volume Methods for Partial Differential Equations*, volume 1.

[11] L Mangolini, C Anderson, J Heberlein, and U Kortshagen. Effects of current limitation through the dielectric in atmospheric pressure glows in helium. *J. Phys. D: Appl. Phys.*, 37(7), 2004.

[12] J. Goree, Liu B., and Drake D. Gas flow dependence for plasma-needle disinfection of s. mutans bacteria. *IEEE Trans. Plasma Sci.*, 34, 2006.

[13] Y. Sakiyama and David B. Graves. Neutral gas flow and ring-shaped emission profile in non-thermal rf-excited plasma needle discharge at atmospheric pressure. *Plasma Sources Sci. Technol.*, 18(2):025022, 2009.

[14] R. Sander. Compilation of henry's law constants for inorganic and organic species of potential importance in environmental chemistry (version 3). *http://www.henrys-law.org*, 2013.

[15] Fridman G, Friedman G, Gutsol A, Shekhter A B, Vasilets V N, and Fridman A. Applied plasma medicine. *Plasma Process. Polym.*, 5:503–533, 2008.

[16] M G Kong, G Kroesen, G Morfill, T Nosenko, T Shimizu, J van Dijk, and J L Zimmermann. Plasma medicine: an introductory review. *New Journal of Physics*, 11(11):115012, 2009.

[17] Felipe Iza, Gon Jun Kim, Seung Min Lee, Jae Koo Lee, James L. Walsh, Yuantao T. Zhang, and Michael G. Kong. Microplasmas: Sources, particle kinetics, and biomedical applications. *Plasma Processes and Polymers*, 5(4):322–344, 2008.

[18] K. D. Weltmann, E. Kindel, T. Von Woedtke, M. Hahnel, M. Stieber, and R. Brandenburg. Atmospheric-pressure plasma sources: prospective tools for plasma medicine. *Pure Applied Chemistry*, 82(6), 2010.

[19] K. D. Weltmann, M. Polak, K. Masur, T. von Woedtke, J. Winter, and S. Reuter. Plasma processes and plasma sources in medicine. *Contributions to Plasma Physics*, 52(7):644–654, 2012.

[20] M. Laroussi, M. G. Kong, G. Morfill, and W. Stolz. *Plasma Medicine: Applications of Low-Temperature Gas Plasmas in Medicine and Biology*. Cambridge University Press, 2012.

[21] Th. von Woedtke, S. Reuter, K. Masur, and K.-D. Weltmann. Plasmas for medicine. *Physics Reports*, 530(4):291 – 320, 2013.

[22] J Ehlbeck, U Schnabel, M Polak, J Winter, Th von Woedtke, R Brandenburg, T von dem Hagen, and K-D Weltmann. Low temperature atmospheric pressure plasma sources for microbial decontamination. *Journal of Physics D: Applied Physics*, 44(1):013002, 2011.

[23] Dirk Hegemann, Herwig Brunner, and Christian Oehr. Plasma treatment of polymers for surface and adhesion improvement. *Nuclear Instruments and Methods in Physics Research Section B: Beam Interactions with Materials and Atoms*, 208(0):281 – 286, 2003.

[24] R. Morent, N. De Geyter, J. Verschuren, K. De Clerck, P. Kiekens, and C. Leys. Non-thermal plasma treatment of textiles. *Surface and Coatings Technology*, 202(14):3427 – 3449, 2008.

[25] P. Leprince C. Tendero. Atmospheric pressure plasmas: A review. *Spectrochimica Acta Part B*, 61(1):2 – 30, 2006.

[26] N N Morgan. Atmospheric pressure dielectric barrier discharge chemical and biological applications. *International Journal of Physical Sciences*, 4(13):885–892, 2009.

[27] David B Graves. The emerging role of reactive oxygen and nitrogen species in redox biology and some implications for plasma applications to medicine and biology. *Journal of Physics D: Applied Physics*, 45(26):263001, 2012.

[28] Seiji Samukawa, Masaru Hori, Shahid Rauf, Kunihide Tachibana, Peter Bruggeman, Gerrit Kroesen, J Christopher Whitehead, Anthony B Murphy, Alexander F Gutsol, Svetlana Starikovskaia, Uwe Kortshagen, Jean-Pierre Boeuf, Timothy J Sommerer, Mark J Kushner, Uwe Czarnetzki, and Nigel Mason. The 2012 plasma roadmap. *Journal of Physics D: Applied Physics*, 45(25):253001, 2012.

[29] Rajesh Dorai and Mark J Kushner. A model for plasma modification of polypropylene using atmospheric pressure discharges. *Journal of Physics D: Applied Physics*, 36(6), 2003.

[30] Sara B. Habib, Eleazar Gonzalez, and Robert F. Hicks. Atmospheric oxygen plasma activation of silicon (100) surfaces. *Journal of Vacuum Science and Technology A*, 28(3), 2010.

[31] F. Massines, N. Gherardi, A Fornelli, and S. Martin. Atmospheric pressure plasma deposition of thin films by townsend dielectric barrier discharge. *Surface and Coatings Technology*, 200(5, 6):1855–1861, 2005. Proceedings of the 32nd International Conference on Metallurgical Coatings and Thin Films.

[32] Waymouth J F. *Electrical Discharge Lamps*. M. I. T. Press, 1971.

[33] Boeuf J P. Plasma display panels: physics, recent developments and key issues. *Phys. D: Appl. Phys*, 36, 2003.

[34] DeGeyter N, Morent R, and Leys C. Penetration of a dielectric barrier discharge plasma into textile structures at medium pressure. *Plasma Sources Sci. Technol.*, 15, 2006.

[35] D. Petrovic, T. Martens, J. van Dijk, W. J. M. Brok, and A. Bogaerts. Modelling of a dielectric barrier discharge used as a flowing chemical reactor. *J. Phys. Conference Series*, 133, 2008.

[36] K. Miyamoto. *Plasma physics for nuclear fusion*. M. I. T. Press, Cambridge, MA.

[37] F. Paschen. *Wied. Ann.*, (69), 1889.

[38] A. Fridman and L. Kennedy. *Plasma Physics and Engineering*. Taylor and Francis, 2004.

[39] N St J Braithwaite. Introduction to gas discharges. *Plasma Sources Science and Technology*, 9(4):517, 2000.

[40] P. Chabert and N. Braithwaite. *Physics of Radio-Frequency Plasmas*. Cambridge University Press, 2011.

[41] Ulrich Kogelschatz. Dielectric-barrier discharges: Their history, discharge physics, and industrial applications. *Plasma Chemistry and Plasma Processing*, 23(1), 2003.

[42] X Lu, M Laroussi, and V Puech. On atmospheric-pressure non-equilibrium plasma jets and plasma bullets. *Plasma Sources Science and Technology*, 21(3):034005, 2012.

[43] F Massines, A Rabehi, P Decomps, R B Gadri, P Ségur, and C Mayoux. Experimental and theoretical study of a glow discharge at atmospheric pressure controlled by dielectric barrier. *J. Appl. Phys.*, 83(6), 1998.

[44] Y. B. Golubovskii, V. A. Maiorov, J. Behnke, and J. F. Behnke. Modelling of the homogeneous barrier discharge in helium at atmospheric pressure. *J. Phys. D: Appl. Phys.*, 36(1):39, 2003.

[45] A. Schutze, J. Y. Jeong, S. E. Babayan, J. Park, G. S. Selwyn, and R. F. Hicks. The atmospheric pressure plasma jet: A review and comparison to other plasma sources. *IEEE Trans. Plasma Sci.*, 26(6), 1998.

[46] Mounir Laroussi. Low temperature plasma-based sterilization: Overview and state-of-the-art. *Plasma Processes and Polymers*, 2(5):391–400, 2005.

[47] Teschke M., Kedzierski J., Finantu-Dinu E.G., Korzec D., and J. Engemann. High-speed photographs of a dielectric barrier atmospheric pressure plasma jet. *IEEE Trans. Plasma Sci.*, 33, 2005.

[48] X Lu and M Laroussi. Dynamics of an atmospheric pressure plasma plume generated by sub-microsecond voltage pulses. *Journal of Applied Physics*, 100(6):063302, 2006.

[49] J-P Boeuf, L L Yang, and L C Pitchford. Dynamics of a guided streamer (plasma bullet) in a helium jet in air at atmospheric pressure. *Journal of Physics D: Applied Physics*, 46(1):015201, 2013.

[50] D. Breden, K. Miki, and L. L. Raja. Self-consistent two-dimensional modelling of cold atmospheric-pressure plasma jets/bullets. *Plasma Sources Sci. Technol.*, 21, 2012.

[51] Y. Sakiyama, David B. Graves, J. Jarrige, and M. Laroussi. Finite element analysis of ring-shaped emission profile in plasma bullet. *Appl. Phys. Lett.*, 96, 2010.

[52] E Stoffels, I E Kieft, R E J Sladek, L J M van den Bedem, E P van der Laan, and M Steinbuch. Plasma needle for in vivo medical treatment: recent developments and perspectives. *Plasma Sources Science and Technology*, 15(4):S169, 2006.

[53] J. Goree, Liu B., Drake D., and Stoffels E. Killing of s. mutans bacteria using a plasma needle at atmospheric pressure. *IEEE Trans. Plasma Sci.*, 34, 2006.

[54] Yukinori Sakiyama, Nikolas Knake, Daniel Schroder, Jorg Winter, Volker Schulz-von der Gathen, and David B. Graves. Gas flow dependence of ground state atomic oxygen in plasma needle discharge at atmospheric pressure. *Applied Physics Letters*, 97(15), 2010.

[55] J. J. Shi and M. G. Kong. Mechanisms of the alpha and gamma modes in radio-frequency atmospheric glow discharges. *Journal of Applied Physics*, 97(2):023306, 2005.

[56] Jochen Waskoenig, Kari Niemi, Nikolas Knake, Lucy Marie Graham, Stephan Reuter, Volker Schulz von der Gathen, and Timo Gans. Diagnostic-based modeling on a micro-scale atmospheric-pressure plasma jet. *Pure and Applied Chemistry*, 82(6):1209, 2010.

[57] K. Niemi, S. Reuter, L. M. Graham, J. Waskoenig, and T. Gans. Diagnostic based modeling for determining absolute atomic oxygen densities in atmospheric pressure helium-oxygen plasmas. *Applied Physics Letters*, 95(15):151504, 2009.

[58] K. McKay, D. X. Liu, M. Z. Rong, F. Iza, and M. G. Kong. Dynamics and particle fluxes in atmospheric-pressure electronegative radio frequency microplasmas. *Applied Physics Letters*, 99(9):091501, 2011.

[59] Aijun Yang, Xiaohua Wang, Mingzhe Rong, Dingxin Liu, Felipe Iza, and Michael G. Kong. 1-d fluid model of atmospheric-pressure rf He + O_2 cold plasmas: Parametric study and critical evaluation. *Physics of Plasmas*, 18(11):113503, 2011.

[60] K Niemi, J Waskoenig, N Sadeghi, T Gans, and D O'Connell. The role of helium metastable states in radio frequency driven helium oxygen atmospheric pressure plasma jets measurement and numerical simulation. *Plasma Sources Science and Technology*, 20(5):055005, 2011.

[61] Torben Hemke, Alexander Wollny, Markus Gebhardt, Ralf Peter Brinkmann, and Thomas Mussenbrock. Spatially resolved simulation of a radio-frequency driven micro-atmospheric pressure plasma jet and its effluent. *Journal of Physics D: Applied Physics*, 44(28):285206, 2011.

[62] D Ellerweg, J Benedikt, A von Keudell, N Knake, and V Schulz von der Gathen. Characterization of the effluent of a He/O_2 microscale atmospheric pressure plasma jet by quantitative molecular beam mass spectrometry. *New Journal of Physics*, 12(1):013021, 2010.

[63] B Niermann, T Hemke, N Y Babaeva, M Boke, M J Kushner, T Mussenbrock, and J Winter. Spatial dynamics of helium metastables in sheath or bulk dominated rf micro-plasma jets. *Journal of Physics D: Applied Physics*, 44(48):485204, 2011.

[64] D Ellerweg, A von Keudell, and J Benedikt. Unexpected O and O_3 production in the effluent of He/O_2 microplasma jets emanating into ambient air. *Plasma Sources Science and Technology*, 21(3):034019, 2012.

[65] Comsol Multiphysics. `http://www.comsol.com`. 2013.

[66] R. W. Hockney and J. W. Eastwood. *Computer Simulation using Particles*. Adam Hilger, 1988.

[67] C. K. Birdsall and A. B. Langdon. *Plasma Physics via Computer Simulation*. Adam Hilger, 1991.

[68] A. Bogaerts and R. Gijbels. Hybrid modelling network for a helium-argon-copper hollow cathode discharge used for laser applications. *J. Appl. Phys.*, 92(11):6408–6422, 2002.

[69] M. J. Druyvesteyn and F. M. Penning. The mechanism of electrical discharges in gases of low pressure. *Rev. Mod. Phys.*, 12.

[70] R J Carman and R P Mildren. Electron energy distribution functions for modelling the plasma kinetics in dielectric barrier discharges. *Journal of Physics D: Applied Physics*, 33(19):L99.

[71] G J M Hagelaar and L C Pitchford. Solving the boltzmann equation to obtain electron transport coefficients and rate coefficients for fluid models. *Plasma Sources Sci. Technol.*, 14(4):722, 2005.

[72] Boltzmann Solver. Bolsig+, electron boltzmann equation solver, `www.siglo-kinema.com/bolsig.htm`, 2012.

[73] Paul M. Belan. *Fundamentals of Plasma Physics*. Cambridge University Press, 2006.

[74] Nicholas A. Krall and Alvin W. Trivelpiece. *Principles of plasma physics*. McGraw-Hill, 1973.

[75] L. A. Viehland and E. A. Mason. Kinetic scheme of the non-equilibrium discharge in nitrogen-oxygen mixtures. *Atomic Data and Nuclear Data tables*, 60:37–95, 1995.

[76] B. B. Bird, W. E. Stewart, and E. N. Lightfoot. *Transport phenomena*. Wiley, New York, 2002.

[77] G. J. M. Hagelaar. *Modeling of Microdischarges for Display Technology*. PhD thesis, Technische Universiteit Eindhoven, 2000.

[78] J. Tu, G. H. Yeoh, and C. Liu. *Computational fluid dynamics: A practical approach*. Elsevier,Butterworth-Heineman, 2008.

[79] NIST Chemistry WebBook: National Institute of Standards and Technology. *http://webbook.nist.gov*, 2013.

[80] Rajani P. Satti and Ajay K. Agrawal. Flow structure in the near-field of buoyant low-density gas jets. *International Journal of Heat and Fluid Flow*, 27(2):336 – 347, 2006.

[81] S. Gordon and B.J. McBride. Computer program for calculation of complex chemical equilibrium compositions, rocket performance, incident and reflected shocks, and chapman-jouquet detonations. *NASA-SP-273*, 1971.

[82] O.C. Zienkiewicz, R.L. Taylor, and P. Nithiarasu. *The Finite Element Method for Fluid Dynamics*. Elsevier, 2005.

[83] A.C. Hindmarsh, P.N. Brown, K.E. Grant, S.L. Lee, R. Serban, D.E. Shumaker, and C.S. Woodward. Sundials: Suite of nonlinear and differential/algebraic equation solvers. *ACM T. Math. Software*, 31(3), 2005.

[84] P. Deuflhard. A modified newton method for the solution of ill-conditioned systems of nonlinear equations with application to multiple shooting. *Numer. Math.*, 22, 1974.

[85] PARDISO. Linear solver `www.pardiso-project.org/`.

[86] O. Schenk and K. Gartner. Solving unsymmetric sparse systems of linear equations with pardiso. *Journal of Future Generation Computer Systems*, 20(3):475 – 487, 2004.

[87] R. Codina. Comparison of some finite element methods for solving the diffusion-convection-reaction equation. *Comput. Methods Appl. Mech. Engrg.*, 156, 1998.

[88] G. Hauke. A simple subgrid scale stabilized method for the advection-diffusion-reaction equation. *Comput. Methods Appl. Mech. Engrg.*, 191, 2002.

[89] Yukinori Sakiyama, David B Graves, Hung-Wen Chang, Tetsuji Shimizu, and Gregor E Morfill. Plasma chemistry model of surface microdischarges in humid air and dynamics of reactive neutral speices. *J. Phys. D: Appl. Phys.*, 45, 2012.

[90] Ding-Xin Liu, Ming-Zhe Rong, Xiao-Hua Wang, Felipe Iza, Michael G. Kong, and Peter Bruggeman. Main species and physicochemical processes in cold atmospheric-pressure helium oxygen plasmas. *Plasma Processes and Polymers*, 7(9-10):846–865, 2010.

[91] Tomoyuki Murakami, Kari Niemi, Timo Gans, Deborah O'Connell, and William G Graham. Chemical kinetics and reactive species in atmospheric pressure helium oxygen plasmas with humid-air impurities. *Plasma Sources Science and Technology*, 22(1):015003, 2013.

[92] J. H. Liu, X. Y. Liu, K. Hu, D. W. Liu, X. P. Lu, F. Iza, and M. G. Kong. Plasma plume propagation characteristics of pulsed radio frequency plasma jet. *Applied Physics Letters*, 98(15):151502, 2011.

[93] Xuechun Li, Huan Wang, Zhenfeng Ding, and Younian Wang. Simulation of a pulse-modulated radio-frequency atmospheric pressure glow discharge. *Thin Solid Films*, 519(20):6928 – 6930, 2011. 10th Asia-Pacific Conference on Plasma Science and Technology.

[94] Jizhong Sun, Qi Wang, Zhengfen Ding, Xuechun Li, and Dezhen Wang. Numerical investigation of pulse-modulated atmospheric radio frequency discharges in helium under different duty cycles. *Physics of Plasmas*, 18(12):123502, 2011.

[95] T. Martens. *Numerical simulations of dielectric barrier discharges*. PhD thesis, Universiteit Antwerpen, 2010.

[96] M. Iqbal. *Computational Investigations of Atmospheric Pressure Discharges*. PhD thesis, Dublin City University, 2009.

[97] W. S. Kang, H.S. Kim, and S. H. Hong. Gas temperature effect on discharge-mode characteristics of atmospheric-pressure dielectric barrier discharge in a helium-oxygen mixture. *IEEE Trans. Plasma Sci.*, 38(8), 2010.

[98] I Radu, R Bartnikas, and M R Wertheimer. Frequency and voltage dependence of glow and pseudoglow discharges in helium under atmospheric pressure. *IEEE Trans. Plasma Sci.*, 31(6), 2003.

[99] Dongsoo Lee, Jin Myung Park, Sang Hee Hong, and Yongho Kim. Numerical simulation on mode transition of atmospheric dielectric barrier discharge in helium-oxygen mixture. *Plasma Science, IEEE Transactions on*, 33(2):949–957, April 2005.

[100] J. Stevefelt, J. M. Pouvesle, and A. Bouchoule. Reaction kinetics of a high pressure helium fast discharge afterglow. *The Journal of Chemical Physics*, 76(8):4006–4015, 1982.

[101] I A Kossyi, A Yu Kostinsky, A A Matveyev, and V P Silakov. Kinetic scheme of the non-equilibrium discharge in nitrogen-oxygen mixtures. *Plasma Sources Sci. Technol.*, 1(3):207.

[102] D. Stafford and Mark J. Kushner. $O_2(a^1\Delta)$ production in He/O_2 mixtures in flowing low pressure plasmas. *Journal of Applied Physics*, 96(5):2451–2465, 2004.

[103] R P Cardoso, T Belmonte, G Henrion, and N Sadeghi. Influence of trace oxygen on He (2^3S) density in a He/O_2 microwave discharge at atmospheric pressure: behaviour of the time afterglow. *Journal of Physics D: Applied Physics*, 39(19):4178, 2006.

[104] M. Capitelli, C.M Ferreira, B. F. Gordiets, and A. I. Osipov. *Plasma Kinetics in Atmospheric gases*. Springer, Berlin, 2000.

[105] R. J. Vidmar and K. R. Stalder. Computations of the power to sustain plasma in air with relevance to aerospace technology. *AFOSR Final Performance Report*, AFRISRARRE040123, 2004.

[106] N. Sato. Discharge current induced by the motion of charged particles. *J. Phys. D: Appl. Phys.*, 13:3–6, 1980.

[107] T. Martens, A. Bogaerts, W. J. M. Brok, and J. van Dijk. The influence of impurities on the performance of the dielectric barrier discharge. *Applied Physics Letters*, 96(9), 2010.

[108] I. Rafatov, E. A. Bogdanov, and A. A. Kudryavtsev. On the accuracy and reliability of different fluid models of the direct current glow discharge. *Physics of Plasmas*, 19(3):033502, 2012.

[109] J. P. Boeuf. Numerical model of rf glow discharges. *Phys. Rev. A*, 36:6, 1987.

[110] R Peyrous, P Pignolet, and B Held. Kinetic simulation of gaseous species created by an electrical discharge in dry or humid oxygen. *Journal of Physics D: Applied Physics*, 22(11):1658, 1989.

[111] N.N. Doroshenko, V.M.and Kudryavtsev and V.V. Smetanin. Quenching mechanisms for electronically excited species in partially dissociated air. *High Energy Chem.*, 26, 1992.

[112] John T. Herron and David S. Green. Chemical kinetics database and predictive schemes for nonthermal humid air plasma chemistry. part ii. neutral species reactions. *Plasma Chemistry and Plasma Processing*, 21:459–481, 2001.

[113] R. Atkinson, D. L. Baulch, R. A. Cox, Jr. R. F. Hampson, J. A. Kerr, M. J. Rossi, and J. Troe. Evaluated kinetic and photochemical data for atmospheric chemistry: Supplement vi. iupac subcommittee on gas kinetic data evaluation for atmospheric chemistry. *Journal of Physical and Chemical Reference Data*, 26(6), 1997.

[114] Mark J. Kushner. Plasma chemistry of $He/O_2/SiH_4$ and $He/N_2O/SiH_4$ mixtures for remote plasma-activated chemical-vapor deposition of silicon dioxide. *Journal of Applied Physics*, 74(11):6538–6553, 1993.

[115] D. L. Baulch, C. J. Cobos, R. A. Cox, C. Esser, P. Frank, Th. Just, J. A. Kerr, M. J. Pilling, J. Troe, R. W. Walker, and J. Warnatz. Evaluated kinetic data for combustion modelling. *Journal of Physical and Chemical Reference Data*, 21(3):411–734, 1992.

[116] Boughton J.W., Kristyan S., and Lin M.C. Theoretical study of the reaction of hydrogen with nitric acid: ab initio mo and tst/rrkm calculations. *Chemical Physics*, 214(2):219–227, 1997.

[117] H. Matzing. *Chemical Kinetics of Flue Gas Cleaning by Irradiation with Electrons*. Wiley, 2007.

[118] R. E J Sladek, T.A. Baede, and Stoffels. Plasma-needle treatment of substrates with respect to wettability and growth of escherichia coli and streptococcus mutans. *IEEE Trans. Plasma Sci.*, 34:4, 2006.

[119] N Barekzi and M Laroussi. Dose-dependent killing of leukemia cells by low-temperature plasma. *J. Phys. D: Appl. Phys.*, 45:42, 2012.

[120] M Yusupov, E C Neyts, U Khalilov, R Snoeckx, A C T van Duin, and A Bogaerts. Atomic-scale simulations of reactive oxygen plasma species interacting with bacterial cell walls. *New Journal of Physics*, 14:9, 2012.

[121] S. G. Joshi, M. Cooper, A. Yost, M. Paff, U. K. Ercan, G. Friedman G. Fridman, A. Fridman, and A. D. Brooks. Nonthermal dielectric-barrier discharge plasma-induced inactivation involves oxidative dna damage and membrane lipid peroxidation in escherichia coli. *Antimicrobial Agents and Chemotherapy*, 55:3, 2011.

[122] Bruce E. Poling, J. M. Prausnitz, and John Paul O'Connell. *The properties of gases and liquids*. 2001.

[123] V Schulz von der Gathen, L Schaper, N Knake, S Reuter, K Niemi, T Gans, and J Winter. Spatially resolved diagnostics on a microscale atmospheric pressure plasma jet. *Journal of Physics D: Applied Physics*, 41(19):194004, 2008.

[124] K. R. Stalder, R. J. Vidmar, G. Nersisyan, and W. G. Graham. Modeling the chemical kinetics of high-pressure glow discharges in mixtures of helium with real air. *Journal of Applied Physics*, 99(9):093301, 2006.

[125] Gregory P. Smith, David M. Golden, Michael Frenklach, Nigel W. Moriarty, Boris Eiteneer, Mikhail Goldenberg, C. Thomas Bowman, Ronald K. Hanson, Soonho Song,

William C. Gardiner, Jr., Vitali V. Lissianski, and Zhiwei Qin. Gri-mech 3.0 *http://www.me.berkeley.edu/gri_mech/*. 2013.

[126] Seán Kelly and Miles M. Turner. Atomic oxygen patterning from a biomedical needle-plasma source. *Journal of Applied Physics*, 114(12), 2013.

[127] Nikolas Knake, Kari Niemi, Stephan Reuter, Volker Schulz von der Gathen, and Jorg Winter. Absolute atomic oxygen density profiles in the discharge core of a microscale atmospheric pressure plasma jet. *Applied Physics Letters*, 93(13):131503, 2008.

[128] D Schroder, H Bahre, N Knake, J Winter, T de los Arcos, and V Schulz von der Gathen. Influence of target surfaces on the atomic oxygen distribution in the effluent of a micro-scaled atmospheric pressure plasma jet. *Plasma Sources Science and Technology*, 21(2):024007, 2012.

[129] J.W. McConkey, C.P. Malone, P.V. Johnson, C. Winstead, V. McKoy, and I. Kanik. Electron impact dissociation of oxygen-containing molecules. A critical review. *Physics Reports*, 466(1-3):1–103, September 2008.

[130] E Stoffels, Y Aranda Gonzalvo, T D Whitmore, D L Seymour, and J A Rees. Mass spectrometric detection of short-living radicals produced by a plasma needle. *Plasma Sources Science and Technology*, 16(3):549, 2007.

[131] J Benedikt, A Hecimovic, D Ellerweg, and A von Keudell. Quadrupole mass spectrometry of reactive plasmas. *Journal of Physics D: Applied Physics*, 45(40):403001, 2012.

[132] Jianjun Shi, Yeqing Cai, Jie Zhang, Ke Ding, and Jing Zhang. Discharge ignition characteristics of pulsed radio-frequency glow discharges in atmospheric helium. *Physics of Plasmas*, 16(7):070702, 2009.

[133] Jianjun Shi, Yeqing Cai, Jing Zhang, and Yun Yang. Characteristics of pulse-modulated radio-frequency atmospheric pressure glow discharge. *Thin Solid Films*, 518(3):962 – 966, 2009. Proceedings of the 21st Symposium on Plasma Science for Materials.

[134] I. D. Kaganovich, B. N. Ramamurthi, and Demetre J. Economou. Spatiotemporal dynamics of charged species in the afterglow of plasmas containing negative ions. *Phys. Rev. E*, 64:036402, Aug 2001.

[135] Barry Twomey, Mahfujur Rahman, Gerry Byrne, Alan Hynes, Lesley-Ann O'Hare, Liam O'Neill, and Denis Dowling. Effect of plasma exposure on the chemistry and morphology of aerosol-assisted, plasma-deposited coatings. *Plasma Processes and Polymers*, 5(8):737–744, 2008.

[136] B. Twomey, D.P. Dowling, G. Byrne, W.G. Graham, L.F. Schaper, D. Della Croce, A. Hynes, and L. O'Neill. Comparing deposition properties in an atmospheric pressure plasma system operating in uniform and nonuniform modes. *Plasma Science, IEEE Transactions on*, 37(6):961–969, 2009.

[137] J Tynan, V J Law, B Twomey, A M Hynes, S Daniels, G Byrne, and D P Dowling. Evaluation of real-time non-invasive diagnostic tools for the monitoring of a pilot scale atmospheric pressure plasma system. *Measurement Science and Technology*, 20(11):115703, 2009.